IEEE
microwave
MAGAZINE
for the Microwave & Wireless Engineer
Volume 21 • Number 11 • November 2020

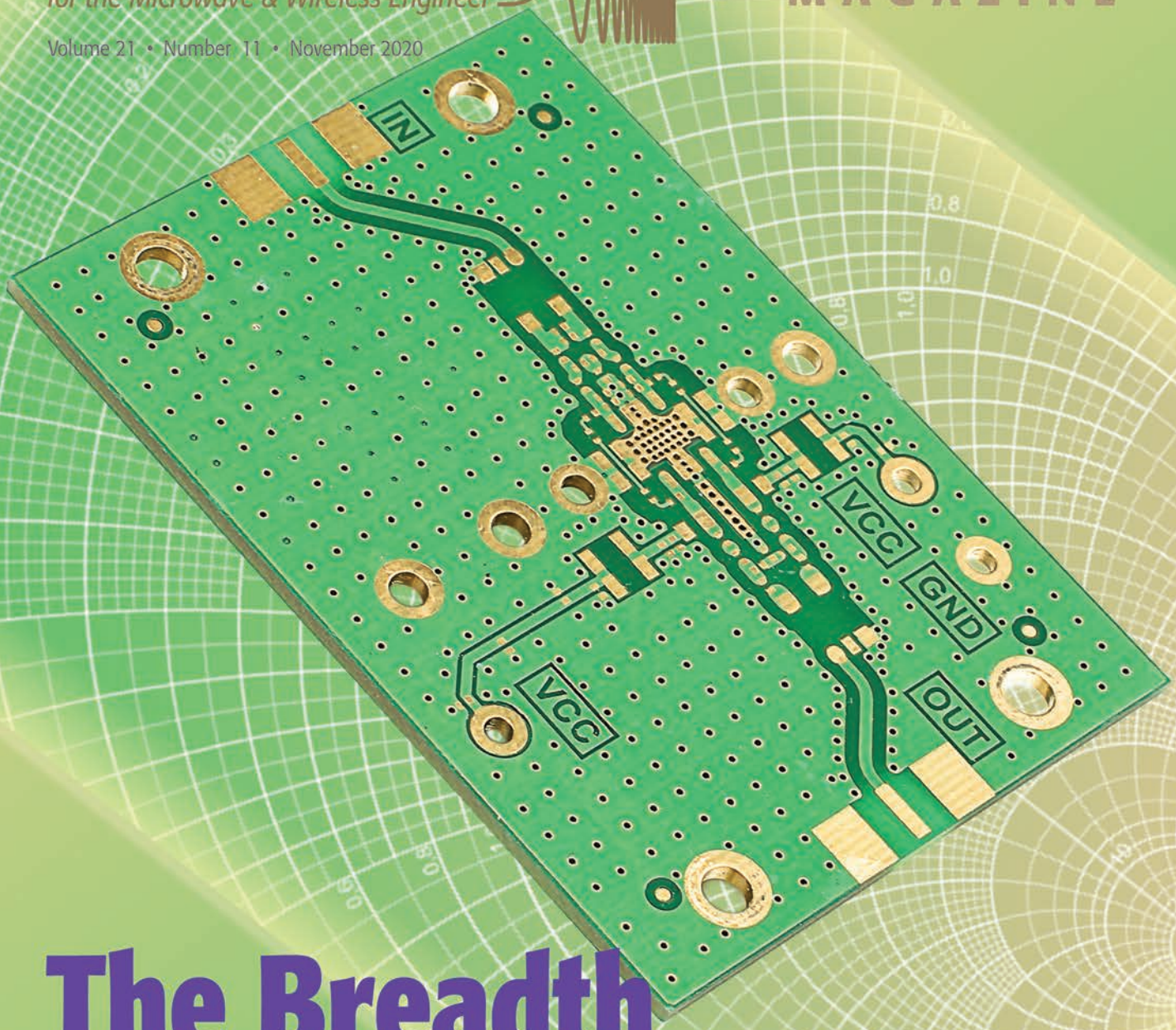

The Breadth of MTT

MTT-S
IEEE

SPECTRAN V6

BEYOND REALTIME

SETS NEW STANDARDS IN SPECTRUM ANALYSIS

USB Real-Time Spectrum Analyzer
& Vector Signal Generator

Includes PC software “RTSA-Suite PRO”

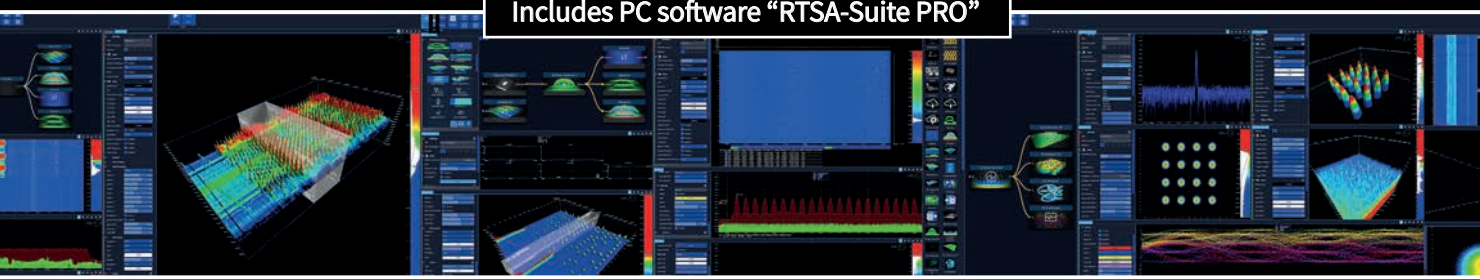

- ✔ RF Frequency range of 10 MHz to 6 GHz
- ✔ Continuous 245 MHz true I/Q streaming
- ✔ Simultaneous measurement of multiple bands
- ✔ Dual USB 3.0 streaming
- ✔ 1 THz/s sweep speed
- ✔ 120 MHz Vector Signal Generator

AARONIA AG
WWW.AARONIA.DE

www.aaronia.com/v6

MADE IN GERMANY

TINY

Wideband Transformers & Baluns!

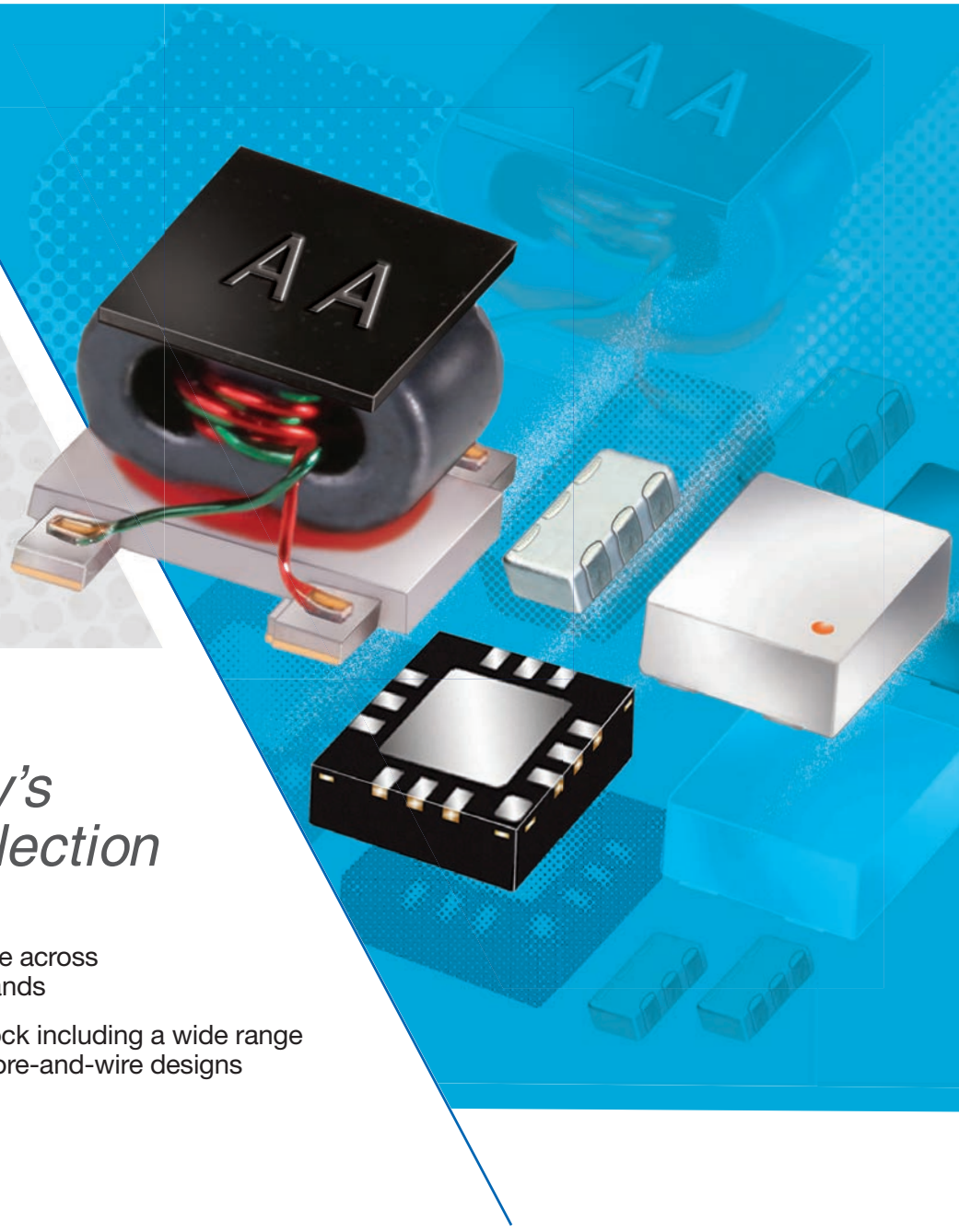

The Industry's Widest Selection

- DC to 24 GHz
- Consistent performance across very wide frequency bands
- Over 300 models in stock including a wide range of MMIC, LTCC, and core-and-wire designs

RoHS compliant.

Mini-Circuits®

(718) 934-4500 sales@minicircuits.com **www.minicircuits.com**

528_Rev F

cadence®

Design Smarter with AWR Software

See for yourself how easy and effective it is to streamline your design process, improve end-product performance, and accelerate time to market for MMICs, RFICs, RF PCBs, microwave modules, antennas, communications systems, radar systems, and more.

Get started at **cadence.com/go/awr/try**.

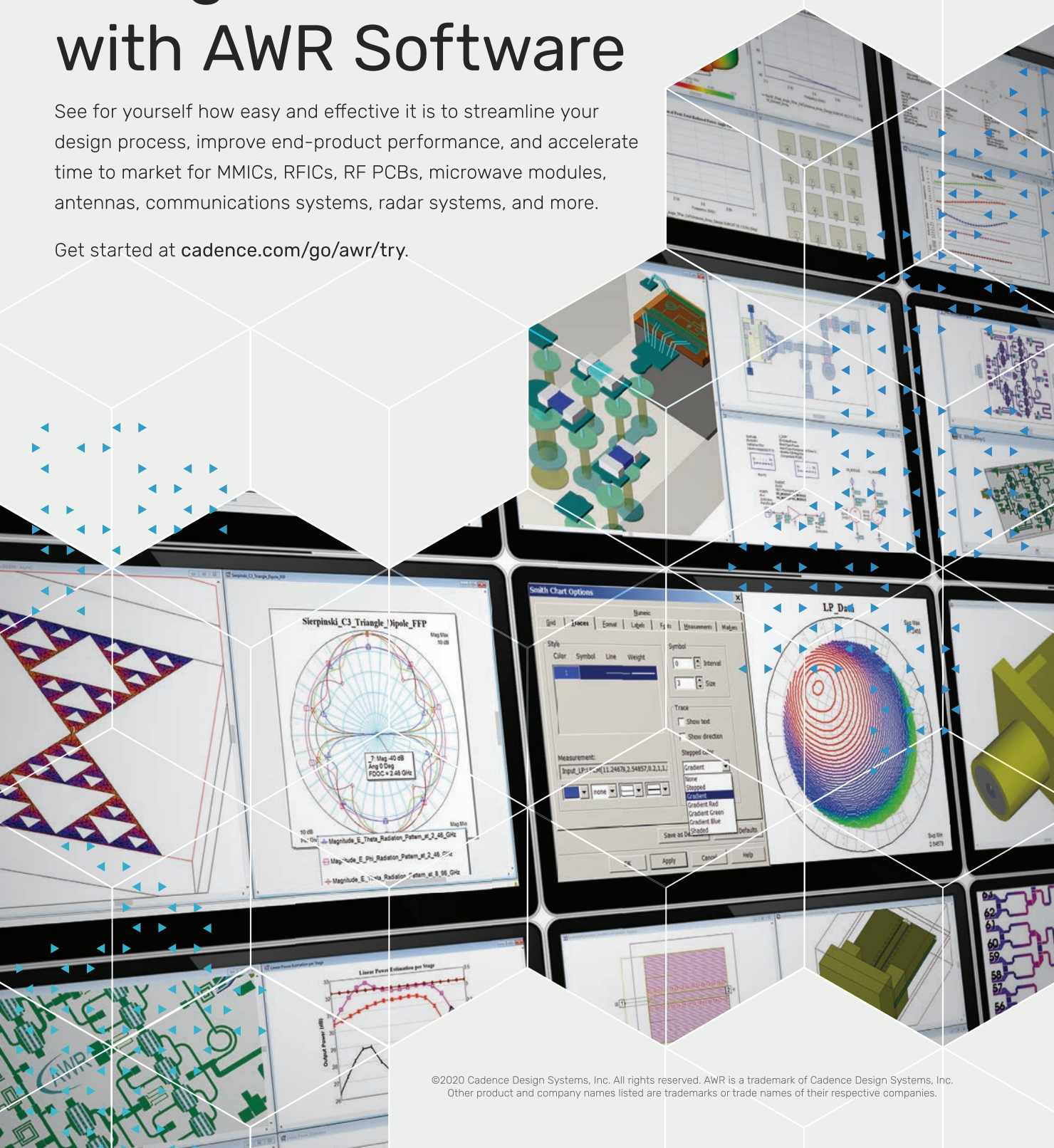

Digital Object Identifier 10.1109/MMM.2020.3015075

IEEE microwave MAGAZINE
for the Microwave & Wireless Engineer

Volume 21 • Number 11 • November 2020 • ISSN 1527-3342

features

on the cover:

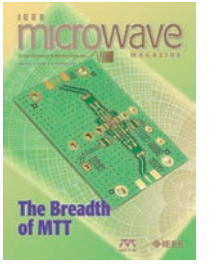

©SHUTTERSTOCK/AUDRIUS MERFELDAS

IEEE microwave MAGAZINE
for the Microwave & Wireless Engineer

IEEE Microwave Magazine (ISSN 1527-3342) (IEMMFF) is published 12 times a year by the Institute of Electrical and Electronics Engineers, Inc. Headquarters: 3 Park Avenue, 17th Floor, New York, NY 10016-5997 USA. Responsibility for the contents rests upon the authors and not upon the IEEE, the Society, or its members. IEEE Service Center (for orders, subscriptions, address changes): 445 Hoes Lane, Piscataway, NJ 08854. Telephone: +1 732 981 0060, +1 800 678 4333. Individual copies: IEEE members US$20.00 (first copy only), nonmembers US$35.00 per copy. Subscription rates: Subscriptions for Society members are included with membership dues. Nonmember subscription rates available upon request. Periodicals postage paid at New York, N.Y., and at additional mailing offices. Ride along enclosed. Postmaster: Send address changes to *IEEE Microwave Magazine*, IEEE Operations Center, 445 Hoes Lane, Piscataway, NJ 08854 USA. Canadian GST #125634188
PRINTED IN THE USA
Digital Object Identifier 10.1109/MMM.2020.3015076

columns & departments

BEREX

5G Revolution and BeRex Solution

5G
MCM, etc.

IoT
Front-end Module, Switch, etc.

Military / Satellite
Power and LNA Transistor, etc.

Wireless Infrastructure
RF Amplifier, Mixer, Divider, Switch, etc.

www.BeRex.com

USA 408) 452-5595 / 657) 235-8222 **KOR** 82-2-568-2754 **E-mail** sales@berex.com

From the Editor's Desk

Welcome to the November Issue

■ **Robert H. Caverly**

Welcome to the November issue of *IEEE Microwave Magazine*! This is one of our "The Breadth of Microwave Theory and Techniques (MTT)" issues in which we publish articles on a variety of topics. These articles are unsolicited and submitted by authors wishing to present reviews and tutorials on topics they think might be of interest to you. This is in contrast to our focus issues, which are usually organized by a guest editor and include articles invited specifically for publication in the issue. In short, anyone with a desire to write a technology review can submit a manuscript for publication in *IEEE Microwave Magazine*; you do not have to be invited to submit.

Writing for this magazine is different than writing for *IEEE Transactions on Microwave Theory and Techniques*, *IEEE Journal of Microwaves*, or *IEEE Microwave and Wireless Components Letters*. Rather than presenting your latest research findings, an *IEEE Microwave Magazine* article should be a general-interest review or tutorial that appeals to a wide audience. The material covered in the feature should also fall within the IEEE Microwave Theory and Techniques Society's (MTT-S's) field of interest (https://www.mtt.org/field-interestsstatement/). Technical features should present a balanced picture of the state of the art rather than focusing on research from a single laboratory or company. Feature articles are typically about 8–10 pages in length, which is approximately 6,000 words, including references. This translates to roughly 16–20 pages of double-spaced, single-column text. All technical features undergo a rigorous peer evaluation. If you have an idea for such a review manuscript, please consider submitting it to the magazine.

©SHUTTERSTOCK.COM/PENWIN

Our first technical feature in this "The Breadth of MTT" issue is an interesting look at a graphical design tool that all microwave and RF engineers know: the Smith chart. Although most of us are quite adept at using the chart on paper, in their article "The 3D Smith Chart: From Theory to Experimental Reality," Andrei Muller and his coauthors take us on an exploration of the 3D Smith chart. Prof. Muller et al. show us its origins and use in several familiar design examples. The second technical feature, by Oscar Quevedo-Teruel et al., "Periodic Structures With Higher Symmetries: Their Applications in Electromagnetic Devices," presents a detailed discussion on periodic structures. These are well known to microwave engineers, but this article takes the discussion a number of steps further by looking at various symmetries in the periodicity that can improve the performance of these structures. Examples of the use of higher symmetries are bandwidth improvements in electronic bandgap structures as well as reduced dispersion properties in parallel-plate waveguides. The final technical feature in this issue, "Balanced to Unbalanced: An Overview of Multifunctional Wideband Balanced-to-Unbalanced

Robert H. Caverly (rcaverly@villanova.edu) is with Villanova University, Villanova, Pennsylvania, United States.

Digital Object Identifier 10.1109/MMM.2020.3016152
Date of current version: 6 October 2020

EASY, FAST, ACCURATE

WIPL-D Pro CAD 2020

Enhanced User Experience

New: released!

- Accelerations of the CAD modeler:
  - Project tree reconstruction
  - Rendering
  - Select operations
  - Validation
- Improvements in the meshing algorithm:
  - Reduction in the number of mesh elements from 10% up to 50%
  - Improvement in pre-meshing of complex faces
  - Overall acceleration of the meshing process
- Introducing a Material library with over 80 predefined materials, and three new ways to define frequency dependent material properties:
  - Cole-Cole approximation
  - Frequency table
  - Djordjevic-Sarkar approximation
- New selection mode options:
  - Select all faces connected with the selected one
  - Select bodies by size
- Local settings:
  - Distributed loading on body level
  - Reference frequency on the level of body, face and edge of wire bodies
- Preview of the model on Open

Features:

- Solid modeling using built-in primitives (curves, surface bodies and solids)
- Import from and export to various CAD formats with efficient model repairing and defeaturing
- Easy manipulations and Boolean Operations
- Quadrilateral mesher optimized for HOBFs
- Full support for symbolic modeling, symmetry, GPU acceleration and other standard WIPL-D features

www.wipl-d.com

Four- and Five-Port Filtering Power Dividers" by Wenjie Feng et al., presents the theory of and example circuits for multiport, multifunctional signal dividers, some of which have relatively small footprints. As these are single-layer structures, they are also candidates for use with on-chip circuits and systems.

We also have a full lineup of columns and other articles in this issue. MTT-S President Alaa Abunjaileh discusses the Society's strategic plan, which has had to be revisited due to the COVID-19 pandemic and related changes in MTT-S activities. Please take a look at the "President's Column" for an overview of the MTT-S's future direction. In our "MicroBusiness" column, two different management styles (leading and misleading) are highlighted, one of which is shown to be much more effective than the other. Our "Microwave Surfing" column looks at the history of the IEEE Committee on Man and Radiation and why its work is still important nearly 50 years after its creation. In the "Society News" column, we have an interview with the chair of the MTT-S Meetings and Symposia Committee, who discusses its general operation and its incredibly busy year dealing with the many conference realignments in light of the global health crisis.

Speaking of global, this month's "Around the Globe" column includes another reprint from *James Clerk Maxwell Foundation Newsletter*, this time looking at the photographs of famous physicists on the wall of Einstein's study. It interesting to see whom Einstein chose to cover part of his study's precious wall space. Our "New Products" editor has put together a list of six recently introduced microwave-related products that might be of interest to you. And, in addition to his regular "Enigmas, etc." column, Dr. Takashi Ohira has written an article for this month's "Educator's Corner" column, where he takes an in-depth look at planar geometry and how it relates to impedance (and ties in with the Smith chart), reflection coefficients, and the Poincaré disk. This material will help you solve the next few "Engimas" puzzles (Prof. Ohira has provided a new one to think about this month as well as the solution to last month's problem). Finally, we have our usual conference calendar; what is not usual, however, is the fact that the conference landscape is continually changing. Please be sure to check the conference websites to see the latest news of any changes in dates, locations, or venues. Enjoy the issue!

President's Column

The 2020 MTT-S Strategic Plan

■ **Alaa Abunjaileh**

The IEEE Microwave Theory and Techniques Society (MTT-S) developed its first formal Strategic Plan in 2010 as part of an IEEE-wide effort. This plan has since become a vital part of the ongoing evolution within IEEE. It presents a model for how Societies perform their strategic planning and provides clear goals, which our community is pursuing, alongside initiatives that will enhance our growth in the coming years.

The MTT-S Strategic Plan has been revised this year; Past President Dylan Williams is leading this effort and chairs our 2020 Strategic Planning Committee, covering every corner of our Society. Greg Lyons, the Society's president-elect and vice-chair of the committee, will be responsible next year for implementing many of the plan's objectives with strong support from committee members.

As you would expect, the COVID-19 pandemic influenced the revision of this plan. The current update explores opportunities that have arisen this year, branching into online and hybrid events that could expand the growth of our Society and increase the footprint of our events. There is emphasis on the development and archiving of digital content that can be shared worldwide as well as on the pursuit of technology for virtual meetings and other events. The Society's Strategic Plan is complex and multifaceted; while it is still being revised as of this writing, I wanted to give you an overview of the plan and a sense of its scope.

©SHUTTERSTOCK.COM/LIGHTSPRING

Our Society's overall goal as articulated in the new draft plan is to "be the indispensable global, collaborative, multidisciplinary community for RF through terahertz technology, for the benefit of humanity." This goal is followed by a set of "vivid descriptions" of what this will look like for the Society, among which are the following:

- The MTT-S will be the first place to which RF and microwave

Alaa Abunjaileh (abunjaileh@ieee.org), 2020 MTT-S president, is with Airbus Defence and Space, Stevenage, United Kingdom.

Digital Object Identifier 10.1109/MMM.2020.3016074
Date of current version: 6 October 2020

MiCIAN

µWave Wizard

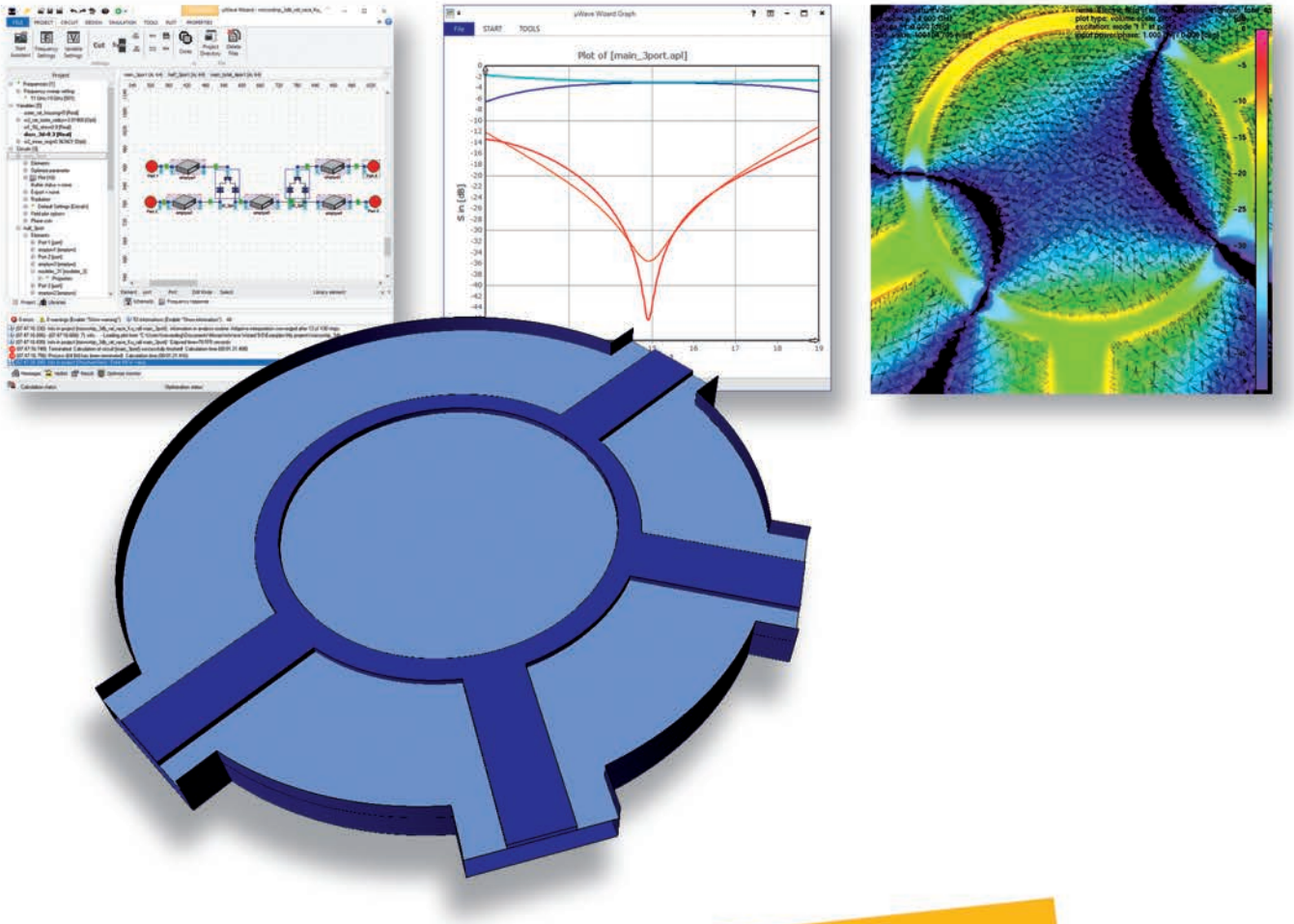

THERE'S MAGIC IN FAST AND ACCURATE RF DESIGNS

µWave Wizard EDA software for fast and accurate designs and analysis of passive components and antennas

- Hybrid solver with six different EM methods
- Rapid development with more than 400 building blocks
- User friendly modeling capabilities
- Full parameterization of structure geometries
- Various powerful synthesis tools and optimizers
- Several import and export CAD formats

MiCIAN

Mician GmbH, Schlachte 21, 28195 Bremen, Germany, Tel.: +49 42116899351, www.mician.com

engineers throughout the world turn to ensure their success.

- The MTT-S will be globally recognized by microwave practitioners and their management/institutions as 1) the authority on microwaves, 2) the unbiased nexus for open interchange of microwave information, and 3) the first choice for the dissemination and discussion of microwave science and engineering.
- MTT-S journals will be universally recognized as "the place to publish," known for the highest quality, and as the main point of communication in all regions of the world about all things RF through terahertz.
- Our professional and organizational programs and practices, such as the IEEE International Microwave Symposium and IEEE Distinguished Microwave Lecturers, will be the recognized model for other Societies and councils.

The Strategic Plan not only addresses these larger goals of our Society; it also aims to accomplish smaller objectives and specific strategies in the areas of publications, conferences, education, and professional development as well as marketing and communications. For example, the MTT-S will have a fleet of successful conferences around the world, fully accessible to local and global communities. Companies will consider our conferences the number one place to showcase their products/services. As new science and technologies emerge in our field of interest, we will hold conferences and impanel technical committees to address these new areas. Furthermore, the MTT-S will be the world's leading authority for creating, developing, and promoting microwave-related, multidisciplinary publications, activities, and events in collaboration with other IEEE Societies and Councils as well as non-IEEE entities. This will enhance the MTT-S's effort to provide opportunities for collaborative learning and facilitate megahertz through terahertz authoritative information exchange for educating and supporting students from the early stages through their higher education and throughout their professional careers.

There is emphasis on the development and archiving of digital content that can be shared worldwide as well as on the pursuit of technology for virtual meetings and other events.

Strategic planning for the MTT-S should become the methodology for our operations at all times and at all levels throughout the Society. This plan represents a compass the Society will use to guide its work over the next five years. Each year of its life, the plan will be updated based on past experiences and new circumstances or as new opportunities and challenges emerge so that the global community can continue to actively and increasingly engage with our Society.

My "electronic door" will always be open to hear any feedback, suggestions, constructive criticism, or complaints; you can reach me at abun jaileh@ieee.org. If you would like to get more involved in the MTT-S, please send me an email with a short description of your interests, and I will get back to you about possible positions within the Society.

MicroBusiness

Leading and Misleading

■ **Fred Schindler**

There is an interesting relationship between the words *leading* and *misleading* and their meanings. *Leading* is commonly used to describe the process or ability of getting people to follow. *Misleading* means conveying something that isn't correct. They aren't quite opposites, at least not in common usage. People try to mislead one another all the time. Leaders do, too. In my experience, misleading is generally not an effective way to lead. We tend to be persuaded by facts and realities. Misleading statements that are not based in reality eventually discredit the leader who makes them. Is such a leader a leader at all?

©SHUTTERSTOCK.COM/ABSCENT

Are there categories of misleading? Is being misleading sometimes a useful management tool? Consider a famous case of a leader misrepresenting reality. People who worked for Steve Jobs, the cofounder of Apple, talked about his "reality distortion field." He used it to motivate others and convince them to accomplish the seemingly impossible. It was, perhaps, self-serving, but it led to the development of many innovative products. The focus was not on him and his personal desires, though. Rather, the focus was on a common goal of fulfilling a vision. He was effectively leading a team. Ultimately, he wasn't misleading people at all. He was convincing his team that what it thought was impossible was actually possible.

There are plenty of scenarios where leaders intentionally provide misleading information. In some cases, leaders feel compelled to do so for the benefit of the organization. A good example of this is when companies need to downsize and lay off some employees. It's a difficult subject, and the process is challenging. Usually, plans are developed in secret and then quickly executed, followed by communications within the organization and sometimes a disclosure outside the company. This can all be done without being misleading. A leader wants to take the necessary action with minimal disruption, share information about what happened, and then have everyone move forward.

Fred Schindler (m.schindler@ieee.org) consults on management issues in Boston, Massachusetts, USA.

Digital Object Identifier 10.1109/MMM.2020.3014990
Date of current version: 6 October 2020

In concept, this is a good plan, but the reality is often different. More than once I was at a company where employees noticed that the HR staff had been working late into the night for several days. With a declining business environment in the background, it wasn't difficult to guess that HR was planning to reduce staff. In one case, there were denials of impending layoffs just days before job cuts were announced.

The greatest challenge is in attempting a quick execution and follow-up communications. The execution isn't always fast. Some people are out of the office or away on travel, so it isn't immediately possible to inform them that they are being laid off. Then, it becomes a choice between broadly communicating to the organization before the job cuts are complete or waiting to discuss the reductions until after they are finished. Communications can become muddled, people will be confused and preoccupied, and many employees will feel misled.

In the end, the leaders may just be misleading themselves, thinking that this can be done quickly and that the organization will get back to work. It won't. Even if a layoff is done well, its disruption will linger. If it's handled poorly, the many employees who weren't let go will consider finding work somewhere else.

Leaders can mislead in many ways. I was told by a senior leader at a former employer that my organization would not be closed down, only to have him shutter the operation several weeks later. I guess he wasn't ready to disclose the reality of the situation. But many of us suspected we were going to be shut down, and he didn't gain credibility by misleading me. Perhaps it didn't matter that it didn't matter to him. It contributed to my eventual departure.

There are also leaders who chronically mislead—seemingly pathological liars. There was, for example, the manager who talked about his "open-door policy" even though his door was often closed. Perhaps it was his wish to have an open door, even though it wasn't his practice. It was also his wish to grow the business. He wasn't able to accomplish that, either.

I worked for a leader who claimed that he had invented an innovative technology, one that the industry was broadly adopting at the time. It wasn't difficult for most of us to determine that his claim wasn't true. Patents are public information, enabling anyone with enough interest to investigate them. He hadn't invented the technology. He did have some patents in the general technical area, and perhaps one of them helped facilitate the innovative technology. He made the claim often enough that he probably came to believe it himself. Ultimately, it was self-aggrandizement, and didn't help him lead us.

We saw similar behaviors in his management practices. Like any organization, we had our share of technical and project problems. When problems occurred, he needed to assign blame. When problems were solved, he needed to assume credit. That his management of the organization may have been part of the problem was beyond his conception. He had an inability to accept blame, a need for adulation, and a suspension of reality. He misled his employees, and he misled himself.

There were some who considered him a great leader. They were mostly people who didn't work in his organization. Their assessments were primarily based on what he told them. He was keen to boast of his accomplishments, take credit for the contributions of others, and deflect blame from himself. The facts, for those who were interested in considering them, told a different story. There were others who defended him despite his faults because it served their self-interests, even though he wasn't acting in the best interests of the overall organization. But most people saw his misleading for what it was, and many excellent engineers left the company.

Every leader misleads from time to time, often because he or she perceives it as a necessity. It may even, on balance, be the right thing to occasionally mislead. But when a leader persistently, chronically misleads, consider the motive. If it's the deflection of blame, a need for praise, or the pursuit of self-aggrandizement, that person is not leading. Such people are not leaders at all and should not be in positions where they are expected to manage others.

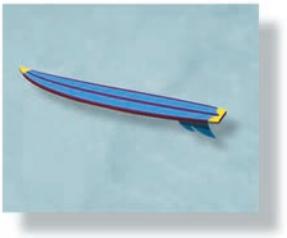

Microwave Surfing

What Is the IEEE Committee on Man and Radiation?

■ **Rajeev Bansal**

Editor's Note
An earlier version of this column originally appeared in the October 2020 issue of *IEEE Antennas and Propagation Magazine*.

"In March of 1973, Consumers Union (CU) held a press conference to announce their decision not to recommend any microwave ovens because of doubt about their radiation safety. They called for zero (later modified to minimum detectable with the appropriate instruments at the time) leakage. The next day, before Senator Tunney, Dr. Milton Zaret testified that 'there is a clear, present, and ever-increasing danger to the entire population of our country from exposure to the entire nonionizing portion of the electromagnetic spectrum'" [1].

©SHUTTERSTOCK.COM/KOLONKO

This was one of the first public challenges faced by the fledgling IEEE Committee on Man and Radiation (COMAR). The committee had been formed in 1972 "to carry out the goal of informing the public on questions related to microwave/RF radiation (excluding optical- and X-radiation) and their effects and hazards" [1]. At the behest of Dr. John Osepchuk, a founding member of COMAR, IEEE added to the charter that "whenever necessary, committee members, or the committee as a whole, should try to correct false or misleading information that is disseminated in newspapers, journals, television, radio, etc. by sending corrective information to managers of the media" [1]. COMAR encouraged a letter-writing campaign to Senator Tunney. In the spring of 1974, IEEE held a press conference with the then-chair of COMAR to announce its opposition to the CU's position.

Nearly 50 years later, when microwave ovens have become fixtures in kitchens and offices around the world, it would appear that the public's fears of nonionizing radiation would be a thing of the past. If only it were so. I first heard about COMAR when, as a graduate student during the late 1970s, I read a COMAR review of a series of alarmist articles about microwaves written by Paul Brodeur and published in *The New Yorker*. Roughly 20 years ago, I joined COMAR as a liaison member from the IEEE Antennas and Propagation Society. By that time, COMAR had become a committee under the umbrella of the IEEE Engineering in Medicine and Biology Society.

As noted on the COMAR website [2], COMAR's primary area of interest is biological effects of nonionizing electromagnetic radiation.

Rajeev Bansal (rajeev.bansal@uconn.edu) is with the University of Connecticut, Storrs, United States.

Digital Object Identifier 10.1109/MMM.2020.3014991
Date of current version: 6 October 2020

> It examines and interprets the biological effects and presents its findings in an authoritative manner, usually in Technical Information Statements (TISs) or Position Papers. These papers are subject to an extensive review process within the Committee and represent the consensus of the Committee.

It is important to note that, while COMAR does not establish safety standards, it has an interest in the standards activity within its scope.

In a TIS [3] published in 2009, COMAR concluded that

> the weight of scientific evidence in the RF bioeffects literature does not support the safety limits recommended by the BioInitiative group. For this reason, COMAR recommends that public health officials continue to base their policies on RF safety limits recommended by established and sanctioned international organizations, such as the Institute of Electrical and Electronics Engineers International Committee on Electromagnetic Safety and the International Commission on Non-Ionizing Radiation Protection, which is formally related to the World Health Organization [3].

In its most recent TIS [4], published in 2020, COMAR addressed the health and safety issues surrounding the new 5G networks. COMAR concludes that "so long as exposures remain below established guidelines, the research results to date do not support a determination that adverse health effects are associated with RF exposures, including those from 5G systems" [4]. From microwave ovens to 5G networks, it has been a long road for COMAR, but the committee is always ready to take on new challenges as they arise.

References

[1] J. Osepchuk, "COMAR after 25 years: Still a challenge," *IEEE Eng. Med. Biol. Mag.*, vol. 15, no. 3, pp. 120–125, 1996. doi: 10.1109/MEMB.1996.6994690.

[2] COMAR. Accessed: July 11, 2020. [Online]. Available: https://ewh.ieee.org/soc/embs/comar/

[3] The Committee on Man and Radiation (COMAR). "COMAR technical information statement: Expert reviews on potential health effects of radiofrequency electromagnetic fields and comments on the bioinitiative report," *Health Phys.*, vol. 97, no. 4, pp. 348–356, Oct. 2009. doi: 10.1097/HP.0b013e3181adcb94.

[4] J. T. Bushberg et al., "IEEE committee on man and radiation—COMAR technical information statement: Health and safety issues concerning exposure of the general public to electromagnetic energy from 5G wireless communications networks," *Health Phys.*, vol. 119, no. 2, pp. 236–246, Aug. 2020. doi: 10.1097/HP.0000000000001301.

Digital Object Identifier 10.1109/MMM.2020.3020484

IMS2021 ATLANTA, GA | 6-11 JUNE 2021

International Microwave Symposium

CALL FOR PAPERS

IEEE

MTT-S IEEE MICROWAVE THEORY & TECHNIQUES SOCIETY

IMS

The IEEE Microwave Theory and Techniques Society's 2021 International Microwave Symposium (IMS2021) will be held June 6–11, 2021 at the Georgia World Congress Center in Atlanta, Georgia. You are cordially invited to join us in Atlanta at the intersection of communications, aerospace, automotive, IoT and other emerging technologies to learn the latest developments in MHz-to-THz theories, techniques, devices, systems and applications. IMS2021 is the centerpiece of Microwave Week 2021 which is comprised of three conferences including the RFIC Symposium (www.rfic-ieee.org) and the ARFTG Conference (www.arftg.org)

New this year: IMS will be a hybrid conference — both face-to-face and virtual. More details will be reported soon.

Microwave Week, with more than 8000 participants and 600 industrial exhibits of state-of-the-art microwave products, is the world's largest gathering of radio-frequency (RF) and microwave professionals encompassing MHz to THz ranges and is the most important forum for the latest research advances and practices in the field. IMS2021 offers something for everyone, including the following:

- Technical Program — Oral/Poster Sessions, Workshops, Technical Lectures, and Panel/Rump Sessions
- Connected Future Summit (formerly 5G Summit) showcasing the next-generation wireless technologies for mobility, V2X and IoT
- RF Bootcamp intended for students, engineers, and managers from non-microwave engineering disciplines
- Job Fair for students offering employment opportunities within our exhibitor community
- Exhibitor workshops and application seminars featuring presentations by the preeminent technologists from our exhibitors, explaining the technology behind their products
- Special small business/entrepreneurs' area on the exhibitor floor
- Discounted pricing for students with a SUPERPASS offering access to all conference events
- Competitions for Best Industry Paper, Advanced Practices Paper, Student Paper Award, Three-Minute Thesis (3MT), Student Design Competitions and Student Demonstrations; a Student Demonstration event to showcase the prototypes developed by students and presented in the technical papers
- Project Connect for underrepresented minority engineering students, and the Ph.D. Student Initiative for new students
- Networking events for Amateur Radio (HAM) enthusiasts, Women in Engineering (WIE)/Women in Microwaves (WIM), and Young Professionals (YP)
- STEM Program featuring hands-on activities and exhibitions designed to help students in middle and high school expand their understanding of what it is to be an engineer
- Guest hospitality suite and tour programs for attendees and their guests
- New technical areas on RF to mm-wave physical layer security, quantum electronics and AI/ML for RF and microwave

Paper Submission: Authors are invited to submit technical papers describing original work on RF, millimeter-wave, and terahertz theory and techniques. The deadline for submission is 16 December 2020. A blind review process will be used to ensure anonymity for both authors and reviewers. Detailed instructions on submitting a blind-review compliant paper can be found at www.ims-ieee.org. Papers will be evaluated on the basis of originality, content, clarity, and relevance to IMS.

Digital Object Identifier 10.1109/MMM.2020.3020487

PAPER SUBMISSION INSTRUCTIONS:

1. All submissions must be in English.
2. Authors must adhere to the format provided in the template, which can be downloaded from www.ims-ieee.org.
3. For regular submissions, authors must submit their paper at www.ims-ieee.org by 11:59 PM Hawaii Standard Time on 9 December 2020. Late submissions will not be considered. The initial submission should be between three and four pages, must be in PDF format, must be double-blind compliant, and cannot exceed 2MB in size. Hardcopy and email submissions are not accepted.

Page Limit: For the initial submission deadline, the paper length should be three pages. Papers longer than three pages will not be considered. The final page length for the papers accepted for publication in the proceeding is three pages.

Paper Selection Criteria: Papers are reviewed by IMS2021 Technical Program subcommittees. The selection criteria will be:

- **Originality:** Is the contribution unique and significant? Does it advance the state of the art of the technology and/or practices? Are proper references to previous work by the authors and others provided?
- **Quantitative content:** Does the paper give a comprehensive description of the work with adequate supporting data?
- **Clarity:** Is the paper contribution and technical content presented with clarity? Are the writing and accompanying figures clear and understandable?
- **Interest to MTT-S membership:** Why should this work be reported at this conference?

Technical Areas: During the paper submission process, authors will choose a primary and two alternative technical areas (see the Technical Areas). The paper abstract should contain information that clearly reflects the choice of the area(s). Author-selected technical areas will be used to determine an appropriate committee for reviewing the paper. The technical areas are divided into five different categories that are used to organize the paper presentation schedule. It is permissible to choose primary and alternative technical areas that are in different categories.

Presentation Format: IMS offers three types of presentation formats. The authors' preference will be honored where possible, but the IMS2021 Technical Program Committee (TPC) reserves the right to place papers in the most appropriate technical area and presentation format.

1. Full-length (20-minute) papers report significant contributions, advancements, or applications in a formal presentation format with questions and answers (Q&A) at the end.
2. Short (10-minute) papers typically report specific refinements or improvements in the state of the art in a formal presentation format with Q&A at the end.
3. Interactive forum papers provide an opportunity for authors to present their theoretical and/or experimental developments and results in greater detail and in a more informal and conversational setting. Papers will be presented in a standard poster format. An IMS2021 poster template will be provided. In addition, authors have the opportunity to display hardware, perform demonstrations, and conduct discussions with interested IMS attendees.
4. Authors of accepted IMS2021 papers must submit a pre-recorded video of their paper presentation. Details of the video presentation will be communicated with the first author of the selected papers.

Notification: Authors will be notified of the decision by 10 February 2021 via the email address(es) provided with the initial paper submission. For accepted papers, an electronic version of the final manuscript (three to four pages, to be published in the Symposium proceedings) along with a copyright assignment to the IEEE must be submitted by 4 March 2021. Authors will be required to submit their presentation slides using the approved template by 20 May 2021, and these will be made available to all attendees at the conference. The submission instructions will also be provided through emails and can be accessed through the Symposium website. The Symposium proceedings will be recorded on electronic media and archived in IEEE Xplore.

Clearances: It is the authors' responsibility to obtain all required company and government clearances prior to submitting a paper. Authors are strongly urged not to wait until the last day to start the paper submission process. Those unfamiliar with the process may encounter paper formatting or clearance issues that may take time to resolve. A statement certified by the submitting author that such clearances have been obtained and a completed IEEE copyright form must accompany the manuscript of each accepted paper. Details regarding clearances will be available during the paper submission process.

Student Superpass: IMS2021 enthusiastically invites participation from students at all levels to attend IMS2021. All students will be offered the opportunity to purchase a SUPERPASS allowing access to the IMS, RFIC, and ARFTG conferences, all workshops, short courses and panel sessions, Connected Future Summit (formerly 5G Summit), and most other events over the course of the week. Student SUPERPASS prices are significantly discounted to encourage student participation.

Student Paper Competition: Eligible students are encouraged to submit papers for the Student Paper Competition. These papers will be reviewed in the same manner as all other contributed papers. First, second, and third prizes will be awarded based on content and presentation. To be considered for an award, the student must be a full-time student during the time the work was performed, be the lead author, and personally present the paper at IMS. During the submission process, the student is required to provide the email address of the faculty advisor, who will be asked upon the selection of the paper to certify that the work is primarily that of the student. Please refer to www.ims-ieee.org for full eligibility details.

Industry and Advanced Practice Paper Competitions: Eligible authors from industry are encouraged to submit papers for the Industry Paper Competition. Additionally, any author who submits a paper on advanced practices may be entered into the Advanced Practice Paper Competition. A paper on advanced practices describes an innovative RF/microwave design integration technique, process enhancement, and/or combination thereof that results in significant improvements in performance and/or in time to production for RF/microwave components, subsystems, or systems. The papers will be evaluated using the same standards as all contributed papers. Please refer to www.ims-ieee.org for details.

Workshops, Technical Lectures, Focus and Special Sessions, Panel and Rump Sessions: Topics being considered for these areas include, but are not limited to, next-generation wireless systems (5G and beyond), emerging RF/microwave applications, latest technologies for RF/microwave measurements, and advances in RFIC technology. Please consult www.ims-ieee.org for a more detailed list of desired topics and instructions on how to prepare a proposal. Proposals must be received by 23 September 2020.

MicroApps and Exhibitor Workshops: Microwave Application Seminars (MicroApps) continue as a forum on the exhibition floor for IMS exhibitors to present the technology and special capabilities behind their commercial products. In addition, the Exhibitor workshops provide IMS exhibitors a unique opportunity to provide more in-depth presentations of technical topics to the attendees. Both events are open to all conference and exhibit attendees. Exhibitor workshops require a nominal fee while MicroApps are free of charge.

Student Design Competition: All eligible students or student teams are invited to consider taking part in the Student Design Competitions (SDCs) during the IMS2021. Please refer to www.ims-ieee.org for full eligibility details, a list of IMS2021 SDCs, and the rules for each SDC.

Student Demonstrations: All students who have submitted papers for oral or interactive forum are invited to participate in the Student Demonstrations during the IMS2021. This will be a unique opportunity for students to showcase prototype hardware that was presented during technical sessions. Please refer to www.ims-ieee.org for full eligibility details.

Three-Minute Thesis (3MT®) Workshop: For eligible students and young professionals, participants with accepted papers are invited to attend a full-day workshop on Sunday on presenting technical work for broader audiences. Following the workshop, students will be invited to enter the 3MT® competition. The 3MT® contestants will make a presentation of three minutes or less, supported only by one static slide, in a language appropriate to a non-specialist audience.

IEEE T-MTT Special Issue: Authors of all papers presented at IMS2021 can submit an expanded version of their IMS papers to the Special Issue of the IEEE Transactions on Microwave Theory and Techniques (IEEE T-MTT) devoted to the IMS2021. Please refer to www.ims-ieee.org for details.

TECHNICAL AREAS:

Electromagnetic Field, Device and Circuit Techniques

1. **Field analysis and guided waves** – Novel guiding and radiating structures, new physical phenomena in transmission lines and waveguides, and new analytical methods for solving guided-wave and radiation problems.
2. **Numerical techniques & CAD algorithms** – Finite-difference, finite-element, integral equation, and hybrid methods for RF, microwave, and THz applications. Simulation, modeling, uncertainty quantification, and design optimization; circuit-, EM-, multi-physics-, and statistics-based, including surrogate modeling, space mapping, and model order reduction techniques.
3. **Instrumentation and measurement techniques** – Theoretically supported and experimentally demonstrated linear and nonlinear measurement techniques for devices and materials, error correction, de-embedding, calibration, and novel instrumentation.
4. **MHz-to-THz device modeling** – Active and passive, linear and nonlinear device and structure modeling (physical, empirical, and behavioral) including characterization, parameter extraction, and validation.
5. **Nonlinear circuit and system analysis, simulation, and design** – Distortion, stability and qualitative dynamics analysis; circuits and systems (C&S) simulation techniques and applications; behavioral modeling of nonlinear C&S (excluding PAs); and nonlinear C&S design and implementations.

Passive Components and Packaging

6. **Transmission-line structures** – Novel transmission-line structures and devices, transmission-line equivalent circuits, artificial transmission lines and metamaterial structures, transmission-line applications for devices and systems.
7. **Passive circuit elements** – Couplers, dividers/combiners, hybrids, resonators, and lumped-element approaches.
8. **Planar passive filters and multiplexers** – Planar passive filters and multiplexers including lumped elements, theoretical filter and multiplexer synthesis methods.
9. **Non-planar passive filters and multiplexers** – Resonators, filters and multiplexers based on dielectric, waveguide, coaxial, or other non-planar structures.
10. **Active, tunable, and integrated filters** – Integrated (on Si, LTCC, LCP, MCM-D, GaAs, etc.), active, and tunable filters.
11. **Microwave acoustic, ferrite, ferroelectric, phase-change, and MEMS components** – Surface and bulk acoustic wave devices including FBAR devices, bulk and thin-film ferrite components, ferroelectric-based devices, and phase-change devices and components. RF microelectromechanical and micromachined components and subsystems.
12. **Packaging, MCMs, and 3D manufacturing techniques** – Component and subsystem packaging, assembly methods, inkjet printing, multi-chip modules, wafer stacking, 3D interconnect, and integrated cooling. Novel processes related to 3D printing or additive manufacturing techniques.

Active Devices

13. **Semiconductor devices and process characterization** – RF, microwave, mm-wave, and THz devices on III-V, silicon and other emerging technologies. MMIC and Si RFIC manufacturing, reliability, failure analysis, yield, and cost.
14. **Low-noise amplifiers, variable-gain amplifiers and receivers** – LNAs, VGAs, detectors, receivers, integrated radiometers, cryogenic amplifiers and models, and characterization methods for low-noise integrated circuits and components.
15. **Signal generation, modulators, frequency conversion, and signal shaping ICs** – CW and pulsed oscillators in silicon and III-V processes including VCOs, DROs, YTOs, PLOs, and frequency synthesizers, signal modulators, and frequency conversion ICs in silicon and III-V processes, such as IQ modulators, mixers, frequency multipliers/dividers, switches, and phase shifters.
16. **Mixed-signal and wireline ICs** – High-speed mixed-signal components and subsystems for transmission; equalization and clock-data recovery techniques for electrical backplanes and electro-optical interfaces. High-speed mixed-signal components and subsystems, including ADC, DAC and DDS technologies.
17. **High-power MHz, RF and microwave amplifiers** – Advances in discrete and IC power amplifier devices and design techniques based on III-V and LD-MOS devices, demonstrating improved power, efficiency, and linearity for HF, UHF, VHF, RF and microwave bands (< 26 GHz). Power-combining techniques for SSPA and vacuum electronics.
18. **Compound semiconductor power amplifiers** – Advances in IC power amplifier devices, design techniques and power combining based on III-V and other compound semiconductor devices demonstrating improved power, efficiency, and linearity for millimeter-wave bands; vacuum electronics for millimeter-wave.
19. **Silicon power amplifiers** – Advances in RFIC and digital power amplifier design and power combining techniques based on silicon CMOS and SiGe processes, demonstrating improved power, efficiency, and linearity for RF, millimeter-wave, and sub-THz bands.
20. **Linearization and transmitter techniques for power amplifiers** – Power amplifier design, characterization, and behavioral modeling; linearization and predistortion techniques; envelope-tracking, outphasing and Doherty transmitters for III-V and silicon technologies
21. **Integrated transceivers, beamformers, imaging and phased-array chips and modules** – Design and characterization of complex III-V ICs, silicon ICs, heterogenous systems, and related packaging in the RF to mm-wave including narrowband and wideband designs. Innovative circuits and sub-systems for communications, radar, imaging, and sensing applications. Integrated on-chip antennas and on-package antennas.
22. **Millimeter-wave and terahertz integrated circuits and systems** – Design and characterization of active components including LNAs, PAs, and frequency conversion ICs in silicon and III-V processes and/or packaging in the upper mm-wave and THz regimes; innovative THz circuits systems for communications, radar, imaging, and sensing applications. Demonstrations of on-chip antennas. Novel multi-feed antennas and antenna-electronics co-designs and co-integrations.
23. **Microwave photonics and nanotechnology** – Integrated devices and 1D-2D material-based technology. Multidisciplinary field studying the interaction between microwaves, THz waves, and optical waves for the generation, processing, control, and distribution of microwave, mm-wave, and THz signals. Emerging RF applications of nanophotonics, nanoplasmonics, and nano-optomechanics; nanoscale metrology and imaging.

Systems and Applications

24. **Phased Arrays, MIMO and Beamformers** – Technology advances combining theory and hardware implementation in the areas of phased-array antennas, integrated beamformers, spatial power combining, retrodirective systems, built-in self-test techniques, broadband arrays, digital beamforming, and multi-beam systems. New beamforming, beam-tracking, and spatial notching algorithms, signal processing, and demonstrations.
25. **Radar and Imaging Systems** – RF, millimeter-wave, and sub-THz radar and imaging systems, automotive radars, sensors for intelligent vehicular highway systems, UWB and broadband radar, remote sensing, radiometers, passive and active imaging systems, radar detection techniques, and related signal processing.
26. **Wireless, 5G & Beyond, and New Satellite Communication Systems** – RF, millimeter-wave, and sub-THz communication systems with hardware implementation for terrestrial, vehicular, satellite, and indoor applications, point-to-point links, backhaul and fronthaul applications, radio-over-fiber links, cognitive and software-defined radios, MIMO and full-duplex technologies, and simultaneous transmit and receive (STAR) systems.
27. **Wireless System Characterization and Architectures** – Wireless and 5G & Beyond enabling technologies including but not limited to beamforming techniques, MIMO, massive MIMO, multiple radio access technologies, centralized radio access networks, shared and novel spectrum use, waveform design, modulation schemes, and channel modeling.
28. **Sensing and RFID Systems** – Short range wireless and RFID sensors, gas and fluidic sensors, passive and active tags from HF to millimeter-wave frequency, RFID systems including wearables and ultra-low-power.
29. **Wireless Power Transmission** – Energy harvesting systems and applications, rectifiers, circuits, self-biased systems, combined data and power transfer systems
30. **MHz-to-THz instrumentation for biological measurements and healthcare applications** – Devices, components, circuits and systems for biological measurements and characterizations; biomedical therapeutic and diagnostic applications; systems and instrumentation for biomedical applications; wireless sensors and systems, and implantable and wearable devices for health monitoring and telemedicine.
31. **MHz-To-THz interaction of materials and tissues** – Electromagnetic field interaction at molecular, cellular, and tissue levels; electromagnetic characterization of biological materials and living systems; MRI and microwave imaging. Industrial and scientific, medical applications utilizing microwave power technology; microwave-enhanced chemistry; non-destructive evaluation /testing and material property measurements at nanometer to millimeter. Multi-modal and multi-physical imaging techniques, such as microwave-induced acoustic imaging.

Emerging Technologies

32. **Innovative systems and applications** – Emerging technologies and novel system concepts for RF/microwave applications such as 6G, Internet of Things (IoT), Internet of Space (IoS), wearable computing/communication systems, machine-to-machine (M2M) communication, intelligent transportation, smart cities, smart environment, heterogeneous integration and 3D ICs, silicon photonics and plasmonics.
33. **MHz-to-THz physical layer security** – Devices, circuits, and systems for secured communication and sensing from MHz to THz, addressing general security vulnerability due to electromagnetic emissions, hardware and software co-design for physical layer security, advanced devices and materials to enhance RF, mm-Wave, and THz physical layer security, trusted design, fabrication, packaging, and validation for RF, mm-Wave, and THz electronics;
34. **AI/ML for RF and Mm-Wave** – AI/ML algorithms, implementations, and demonstrations for spectrum sensing, mobile edge networking, and MIMO and array beam operations and management; AL/ML algorithms for design and optimization of RF/mm-Wave components, circuits, and systems; AL/ML algorithms for in-situ sensing, diagnostics, control, reconfiguration, and optimization of MHz to THz communication and sensing circuits and systems.
35. **Quantum devices, systems, and applications** – Cryogenic RF devices, circuits, and systems for general quantum device interfacing and quantum computing applications.

CONNECTING FOR A SMARTER, SAFER WORLD

Atlanta 2021

Important Dates

- **16 September 2020** (Wednesday)

  PROPOSAL SUBMISSION DEADLINE
  For workshops, short courses, focus and special sessions, panel and rump sessions

- **9 December 2020** (Wednesday)

  PAPER SUBMISSION DEADLINE
  All submissions must be made electronically.

- **3 February 2021** (Wednesday)

  PAPER DISSEMINATION
  Authors will be notified by email.

- **3 March 2021** (Wednesday)

  FINAL MANUSCRIPT SUBMISSION DEADLINE
  Manuscript and copyright of accepted papers

- **5 May 2021** (Wednesday)

  WORKSHOP NOTES SUBMISSION DEADLINE
  Electronic upload of workshop notes to the Workshop Organizers.

- **5 May 2021** (Wednesday)

  VIRTUAL PRESENTATIONS SUBMISSION DEADLINE

- **19 May 2021** (Wednesday)

  FINAL PRESENTATIONS SUBMISSION DEADLINE
  Electronic upload of presentations in both PDF and PPT format

- **6–11 June 2021**

  MICROWAVE WEEK
  IMS2021, RFIC 2021, ARFTG, and Exhibition

IMS2021 Technical Program Committee

EXECUTIVE COMMITTEE
Steve Kenney, *General Co-Chair*
John Papapolymerou, *General Co-Chair*
Hua Wang, *TPC Co-Chair*
Debabani Choudhury, *TPC Co-Chair*
George Ponchak, *Finance Chair*

PLENARY SESSION
Mona Jarrahi, *Chair*
Dev Palmer, *Vice Chair*

PROFESSIONAL STAFF
Elsie Vega, *Conference Manager*
Amanda Scacchitti, *Publications Manager*
Carl Sheffres, *Exhibition Manager*
Janine Love, *Exhibition Operations*

SENIOR ADVISORS AND AUXILIARY CONFERENCE CHAIRS/LIAISONS
JK McKinney, *Senior Advisor*
Wayne Shiroma, *Senior Advisor*
Tim Lee, *IMS2020 General Chair*
Ron Ginley, *IMS2021 General Chair*
Brian Floyd, *RFIC2021 General Chair*
Jon Martens, *ARFTG2021 General Chair*
Osama Shanaa, *RFIC2021, TPC Chair*

TECHNICAL PROGRAM COMMITTEE
Hua Wang, *Co-Chair*
Debabani Choudhury, *Co-Chair*
Gabriel Rebeiz, *Senior Advisor*
Jim Buckwalter, *Senior Advisor*

ELECTRONIC PAPER MANAGEMENT
Sandy Owens, *Chair*

WORKSHOPS
Kaushik Sengupta, *Co-Chair*
Glenn Hopkins, *Co-Chair*
TBD, *Co-Chair*
Danilo Manstretta, *RFIC Liaison*
Jon Martens, *ARFTG Liaison*

CONNECTED FUTURE SUMMIT
Shahriar Shahramian, *Chair*
Clay Couey, *Vice Chair*
Aida Vera Lopez, *Vice Chair*

TECHNICAL LECTURES
Jeffrey Nanzer, *Chair*
Steven Bowers, *Vice Chair*
Mona Hella, *RFIC Liaison*

RF BOOT CAMP
Larry Dunleavy, *Chair*
JoAnn Mistler, *Vice Chair*
Tushar Sharma, *Vice Chair*

PANEL SESSIONS
Ruonan Han, *Chair*
Rui Ma, *Vice Chair*

FOCUS/SPECIAL SESSIONS
Manos Tentzeris, *Chair*
Yong-Kyu Yoon, *Vice Chair*
Ommed Momeni, *Vice Chair*

INTERACTIVE FORUM
Prem Chahal, *Chair*
Taiyun Chi, *Vice Chair*

STUDENT PAPER COMPETITION
Edward Gebara, *Chair*
Cagri Ulusoy, *Vice Chair*

STUDENT DESIGN COMPETITIONS
Guoan Wang, *Chair*
Azadeh Ansari, *Vice Chair*

STUDENT DEMONSTRATIONS
David Rickets, *Chair*

ADVANCED PRACTICE/ INDUSTRY PAPER COMPETITION
Steven Rosenau, *Chair*

THREE-MINUTE THESIS
John Bandler, *Co-Chair*
Erin Kiley, *Co-Chair*

MICROAPPS
Michael Trippe, *Chair*

INDUSTRY WORKSHOPS
Steve Nichols, *Chair*

Hackathon
Kathleen Tokuda, *Chair*

The 3D Smith Chart

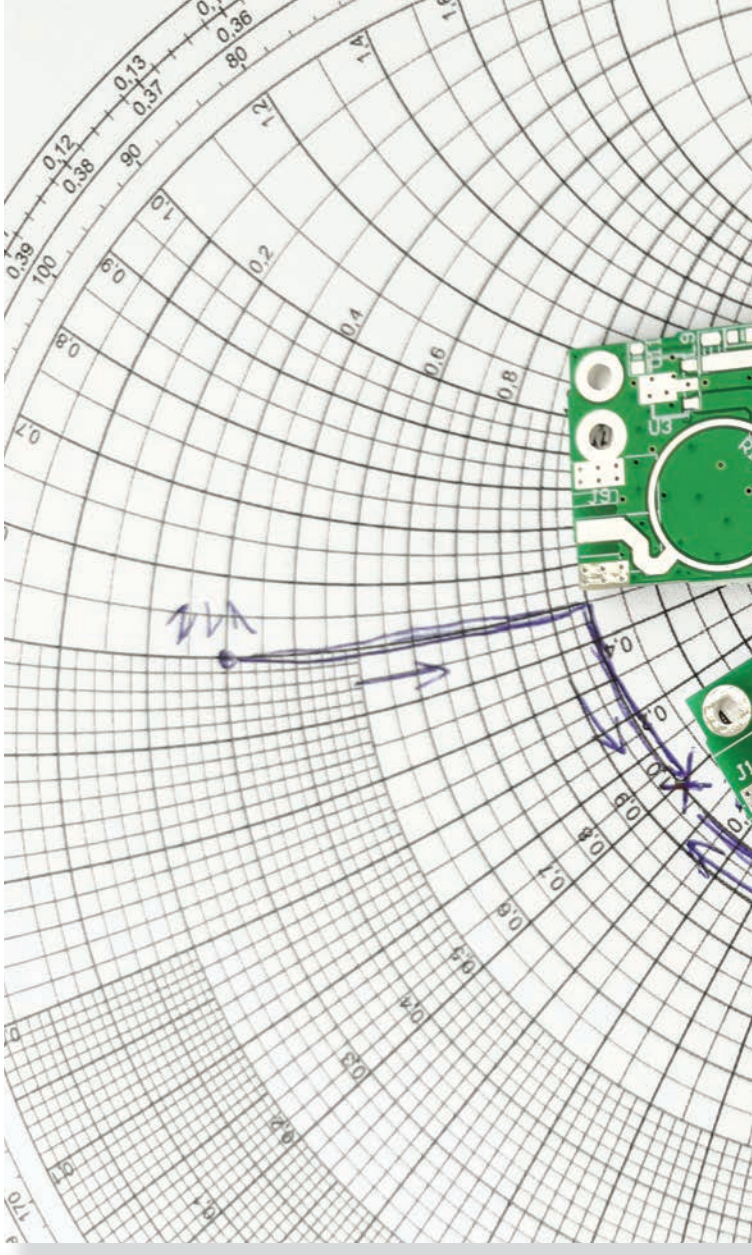

The Smith chart was primarily developed, extended, and refined by Phillip Hagar Smith [1] in a series of works published [2]–[4] between 1939 and 1969. Smith was born in Lexington, Massachusetts, in 1905. He majored in electrical communications at Tufts University and joined the Radio Research Department of Bell Telephone Laboratories (now Bell Labs) in 1928. While there, in around 1930, Smith started work on the diagram that was to become the Smith chart. He submitted the initial version to *Electronics Magazine* in 1937; the magazine finally published his diagram in 1939 [2]. The MIT Radiation Laboratory started using the chart. In 1940, and in 1944 Smith published a second article that incorporated further improvements, including the use of the chart with either impedance or admittance coordinates. In 1952, Smith was elevated to IEEE Fellow for his contributions to the development of antennas and the graphical analysis of transmission-line characteristics. The first issue of *Microwave Journal* (1958) published a biography of Smith to acknowledge the importance of his contributions. In 1969, he wrote the book *Electronic Applications of the Smith Chart in Waveguide, Circuit and Component Analysis*; he retired from Bell Labs in 1970. In 1975, he received the IEEE Microwave Theory and Techniques Society's Special Recognition in Microwave Applications award for the Smith chart, and in 1994 he was elected to the New Jersey Inventors Hall of Fame.

Andrei A. Muller (andrei.muller@epfl.ch) is with the Nanoelectronic Devices Laboratory, École Polytechnique Fédérale de Lausanne, Switzerland. Victor Asavei (victor.asavei@cs.pub.ro) and Alin Moldoveanu (alin.moldoveanu@cs.pub.ro) are with the Department of Computer Science and Engineering, Faculty of Automatic Control and Computers, University Politehnica of Bucharest, Romania. Esther Sanabria-Codesal (esanabri@mat.upv.es) is with the Departamento de Matemática Aplicada, Universitat Politècnica de València, Spain. Riyaz A. Khadar (riyaz.khadar@epfl.ch) is with Powerlab, École Polytechnique Fédérale de Lausanne, Switzerland. Cornel Popescu (cornel.popescu@cs.pub.ro) is with the Department of Computer Science and Engineering, Faculty of Automatic Control and Computers, University Politehnica of Bucharest, Romania. Dan Dascalu (dan.dascalu@imt.ro) is with the Faculty of Electronics, University Politehnica of Bucharest, Romania. Adrian M. Ionescu (adrian.ionescu@epfl.ch) is with the Nanoelectronic Devices Laboratory, École Polytechnique Fédérale de Lausanne, Switzerland.

Digital Object Identifier 10.1109/MMM.2020.3014984

Date of current version: 6 October 2020

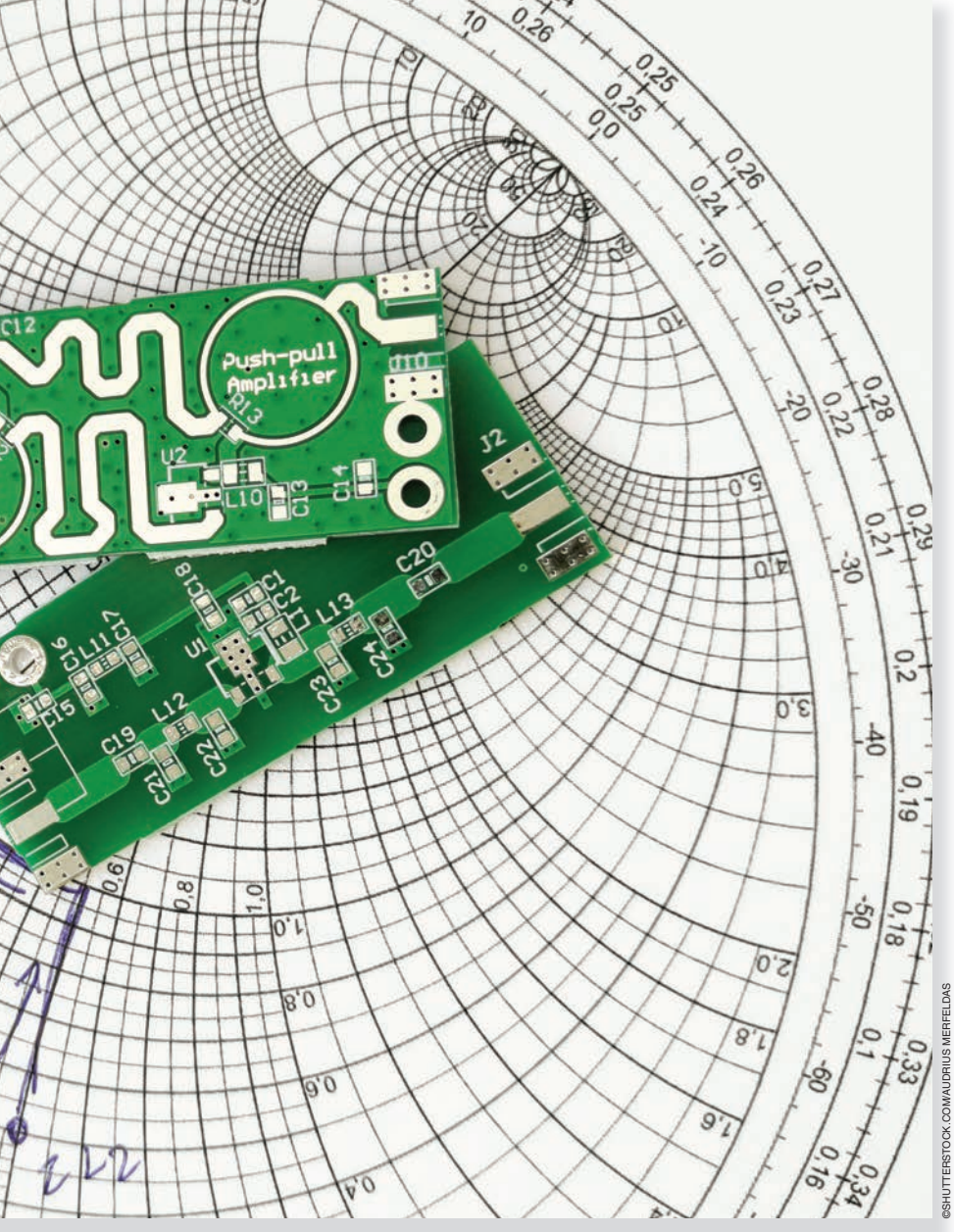

©SHUTTERSTOCK.COM/AUDRIUS MERFELDAS

In this article, we start with several drawings of spherical Smith charts, proposed with the aim of having a generalized chart that deals with both negative and positive resistance circuits within a compact surface. Then, we introduce our suggested 3D Smith chart, discussing its main equation from an inversive geometry perspective, for which Möbius transformations are a simple type of transformation, mapping circles into circles on a special sphere (called a *Riemann sphere* [5]); doing so leads to mathematical completeness and simplicity when dealing with negative resistance and infinity.

Based on this, the article takes the reader on a journey to a compact tool where all negative and positive resistances are analyzed on a preserving-circles patterned sphere. We propose to use the 3D space surrounding the sphere for multiple-complex-scalar visualization, which is useful in equivalent-circuit extractions and multiparameter optimization or simply for multiple-variable imaging and uncovering changes in frequency orientation.

Spherical Smith Chart Drawings for Negative-Resistance Circuits

The Smith chart is limited within the unit circle to passive circuits with positive resistance (r) [or conductance (g)] [1]; circuits with negative r (or g), which occurs in active circuits, are not covered by the conventional Smith chart [4], [6].

In 2006, *IEEE Microwave Magazine* presented an article [7] on drawings by the artist M.C. Escher, including a spherical self-portrait. The article pointed out the connection between the drawings of Escher and hyperbolic geometry while also emphasizing the connection between the Smith chart and Möbius transformations in geometry within the 2D complex plane.

Motivated by the desire to have a unified chart for both active and passive microwave circuits, Zelley proposed drawing an intuitive spherical Smith chart on a ping-pong ball [8]. The drawing in [8] still lacked "mathematical rigor," as the author acknowledged, and no equations were given for its construction.

Andrei A. Muller, Victor Asavei, Alin Moldoveanu, Esther Sanabria-Codesal, Riyaz A. Khadar, Cornel Popescu, Dan Dascalu, and Adrian M. Ionescu

Inspired by the beautiful drawing in [8]—obtained by means of skillful but complicated arithmetical and trigonometrical manipulations—spherical Smith chart theories were proposed in [9] and [10]. In [9], the circles appearing in 2D are mapped into different curves on the spherical chart, while, in [10], the circles on the spherical Smith chart are distorted into ellipses in 2D.

In fact, in [9], the authors parameterize the sphere using two angles as parameters so that the circles of resistance appear when we view the plane containing the equator from the point (1,0,0) and the circles of constant reactance are displayed when we turn this plane sideways. With this structure, the orthogonal projection of these circles onto the equator plane (2D Smith chart) distorts them into ellipses. In the same way, the curves on the sphere considered in [10] are projected orthogonally in 2D and do not, in general, have a circular shape.

Here we develop our main (initial) work on a single concept: inversive geometry. Inversive geometry considers the space of inversive transformations, which map all the circles into circles on a 2D sheet or on the Riemann sphere when points are thrown to infinity (∞). For this geometry, ∞ is just a point [5], [11]–[13], unlike Euclidean geometry, where ∞ = unending, or hyperbolic geometry, where ∞ = circle [7].

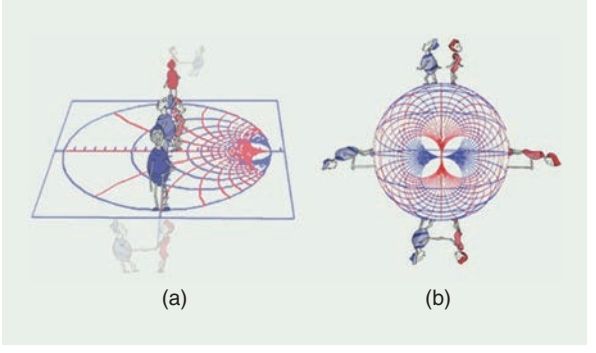

Figure 1. *A vision of infinity: (a) moving away from the origin of the Smith chart and (b) moving away from the origin of the 3D Smith chart. The males and females are in one-to-one correspondence on the Smith and 3D Smith charts.*

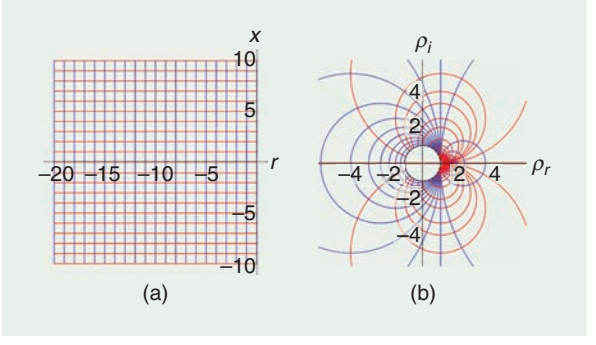

Figure 2. *The (a) impedance plane's left half-plane is (b) mapped onto the exterior of the Smith chart. The constant r circles (for negative r) are now mapped into circles outside of the Smith chart, while the constant x circles are mapped into arcs outside of the Smith chart.*

3D Smith Chart and Negative Resistance

In [12], we propose a single equation that maps the entire reflection-coefficient (ρ) (1) plane onto a unit sphere (s). The equation can be expressed in terms of ρ (its real ρ_r and imaginary ρ_r part), normalized impedance (z), resistance (r), and reactance (x) as follows:

$$\rho(z) = \frac{z-1}{z+1}, \tag{1}$$

$$\rho_{3D}(\rho = \rho_r + j\rho_i) = \left(\frac{2\rho_r}{1+|\rho|^2}, \frac{2\rho_i}{1+|\rho|^2}, \frac{1-|\rho|^2}{1+|\rho|^2}\right),$$

$$\rho_{3D}(z = r + jx) = \left(\frac{|z|^2-1}{|z|^2+1}, \frac{2x}{|z|^2+1}, \frac{2r}{|z|^2+1}\right). \tag{2}$$

This guarantees the invariance of the circles and angles; the 3D Smith chart includes both active and passive microwave circuits on a single sphere, mapping the original Smith chart onto the northern hemisphere and mapping the circles that tend to infinity on the 2D extended Smith chart into circles in the southern hemisphere. Thus, the northern hemisphere contains circuits with positive resistance, and the southern hemisphere contains circuits with negative resistance—east for inductive and west for capacitive.

In further developments of the concept [14], [15], the 3D space surrounding the sphere is then used for visualizing a variety of parameters. Figure 1 shows the conventional Smith chart and 3D Smith chart in a direct comparison. Infinity or reflection coefficients with very high magnitudes are scattered in all directions on the 2D Smith chart (reflection coefficients of loads with negative resistance). On the 3D Smith chart, surpassing the unit magnitude of the reflection coefficient means simply moving south, while infinity is a point on the sphere (the south pole, in geographical language).

Smith Chart Leading Equation and Negative Resistance

The leading equation that generates the Smith chart (1) is presented by Smith as a bilinear conformal transformation in [4]; however, nothing about the global geometrical properties of these transformations is disclosed in [2]–[4].

The equation maps the constant r and constant x grid lines of the impedance plane's right half plane ($r > 0$) into arcs and circles within the unit circle of the Smith chart, leaving the left half plane ($r < 0$) to be mapped in its exterior (as depicted in Figure 2), while throwing points to infinity in all directions. Unlike the literature describing the classical Smith chart, which considers (1)

either a bilinear transformation [4], [7], [16] or a conformal one [17], [18], here we see it as a particular case of inversive transformation, that is, the direct inverse: *D(z)* (3a) [11].

Direct inversive (also called *Möbius*) and indirect *I(z)* inversive transformations (3b) are the only transformations that map all generalized circles (simple circles or infinite extended lines) into generalized circles irrespective of their position on the complex plane. When points are thrown to infinity, one needs to compress the complex plane ($\mathbb{C} \cup \infty$} Riemann sphere) to visualize them [5].

$$D(z) = \frac{az + b}{cz + d}, \tag{3a}$$

$$I(z) = \frac{a\bar{z} + b}{c\bar{z} + d}. \tag{3b}$$

Smith Chart Circle Equation and Negative Capacitance and Inductance

To visualize the circuits exhibiting clockwise and counterclockwise frequency orientation, the dynamics of the frequency path need to be grasped. A variety of circuits exhibit reflection-coefficient movements

In 1952, Smith was elevated to IEEE Fellow for his contributions to the development of antennas and the graphical analysis of transmission-line characteristics.

on the unit circle of the complex plane; however, their intrinsic nature can be very different. Table 1 lists different frequency parameterizations of the unit circle with their angular frequency speed and specific orientation. The oriented curvature [$k(\omega)$] gives the orientation of any possible circuit. When computing the reflection coefficient for a positive inductor or negative capacitor (or vice versa), one will see the identical circle-like path in the reflection plane. However, when computing their curvature k [19], one may spot sign changes and, in this case, find their different intrinsic natures and orientations. In Table 1 it can be seen that the reflection coefficient of a single-port, normalized positive capacitance is a direct inversive transformation (3a) of $z = 1/(j\omega C)$, while the reflection coefficient

TABLE 1. Different perspectives on the unit plane circle depending on the mathematical viewpoint.

Viewpoint	Equation	Speed	Orientation, Curvature (k)	Position at $\omega = \pi/2$, (Starting Point 1, 0)
Algebraic, 2D Euclidean geometry	$r^2 + x^2 = 1$	No information	No information	No information
Differential geometry	$\mathrm{Cos}(\omega) + j\mathrm{Sin}(\omega)\,\omega = \{0, 2 * \pi\}$	1	Counterclockwise, $k = 1$	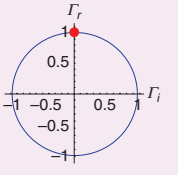
Differential geometry	$\mathrm{Cos}(-2\omega) + j\mathrm{Sin}(-2\omega)\,\omega = \{0, 2 * \pi\}$	2	Clockwise, $k = -1$	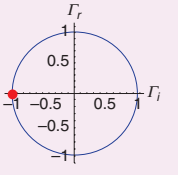
Reflection-coefficient positive capacitor	$\rho = \frac{\frac{1}{j\omega C} - 1}{\frac{1}{j\omega C} + 1}$ $\omega = \{-\infty, \infty\}$	$\frac{2C}{1 + C^2\omega^2}$	Clockwise, $k = -1$	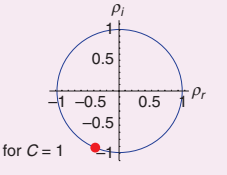
Reflection-coefficient negative capacitor	$\rho = \frac{-\frac{1}{j\omega C} - 1}{-\frac{1}{j\omega C} + 1}$ $\omega = \{-\infty, \infty\}$	$\frac{2C}{1 + C^2\omega^2}$	Counterclockwise, $k = 1$	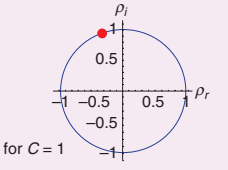

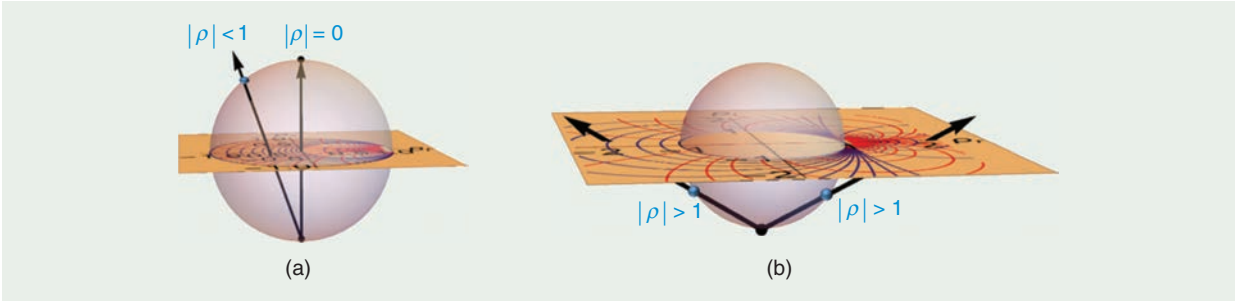

Figure 3. *The 3D Smith chart construction. (a) The 3D Smith chart image of circuits with $|\rho| < 1$ and (b) $|\rho| > 1$ in (b) the southern hemisphere.*

TABLE 2. The properties of the 2D Smith chart versus the 3D Smith chart.

Property	2D Smith Chart	3D Smith Chart Geographic Coordinate System Language (Latitudinal and Longitudinal)
Positive resistance	Interior of unit circle	Northern hemisphere
Negative resistance	Exterior	Southern hemisphere
Perfect matching	Origin	North pole
|Reflection coefficient|==infinity	Infinity, far out	South pole
Inductive	Above the Γ_r axes	East
Capacitive	Below the Γ_r axes	West
r, x, g, and b constants	Circles	Circles
Purely resistive	Γ_r axes	Great circle formed by the prime meridian and antemeridian, dividing the world into east and west hemispheres
$\|\Gamma\|$ = constant	Circle centered in the origin	Latitude circle
Constant phase of the reflection coefficient	Lines through the origin	Great circle of longitude made by the prime meridian and antemeridian
$\|\Gamma\| = 1$	Unit circle	Equator
Open circuit	(1,0)	Null island (prime meridian/equator intersection) (0,0)
Short circuit	(−1,0)	Antipodal point to null island (antemeridian/equator intersection) (0, −180 E)
Unit-inductive load	(0,j)	(0, 90 E)
Unit-capacitive load	(0,−j)	(0, 90 W)

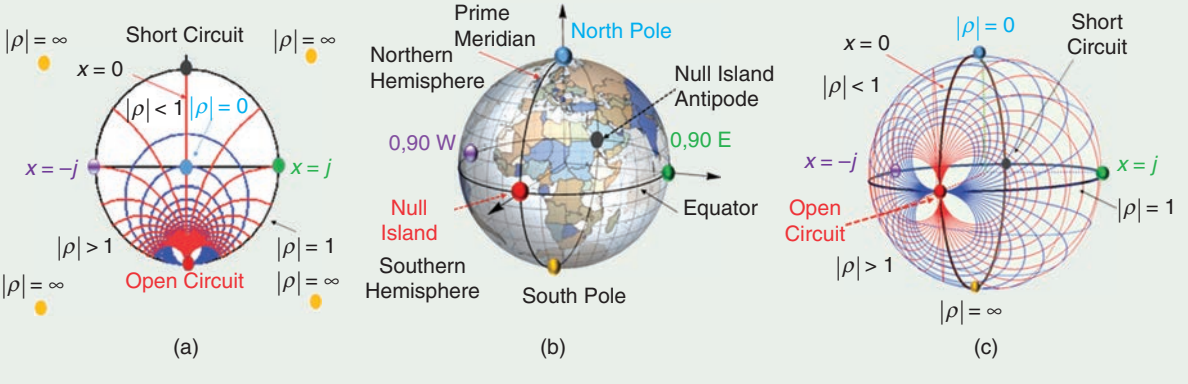

Figure 4. *(a) A 2D Smith chart, (b) Earth, and (c) a 3D Smith chart rendered with r (blue) and x (red) circle points and zones correspondence.*

TABLE 3. The uses, advantages, and disadvantages of the 3D Smith chart.

Use	Circuit Examples	Location	Advantages/Disadvantages
Negative resistances in [12] and [13] and in this article	In amplifier stability, diodes, oscillators, and so on	Southern hemisphere (surface)	Compact space for all possible loads on a sphere (thus a surface); a CAD or 3D printed chart is needed
Gain representations/group delay in [14] and [15] and in this article	Amplifiers	3D space (exterior when positive, interior when negative)	Scalar levels can be seen simultaneously with *S*-parameters; a CAD chart is needed
Frequency dynamics [19] and in this article	All the circuits, negative capacitances, negative inductances, and metamaterials	3D space	*S*-parameters' clockwise and counterclockwise changes can be spotted, and intrinsic physical connections can be made; a CAD chart is needed
Multiparameter in optimizations/equivalent-circuit extractions in [19] and in this article	In the design/modeling of all circuits	Surface and 3D space	Simultaneously fit *S*-parameters and orientation inductances, Qs, and fulfill multiple requirements/the correct extraction of equivalent circuits; a CAD chart is needed

of the negative capacitance is an indirect inversive transformation (3b) of $z = 1/(j\omega C)$; both have the same circle path but opposed orientations. Later in this article, we show how the 3D Smith chart can spot orientation changes.

3D Smith Chart Construction

Figure 3 displays the construction of the 3D Smith chart using a stereographic projection from the south pole with its guiding (2) ($\mathbb{C} \cup \{\infty\}$). The construction is based on the circles' visualization theory of direct and indirect inversive transformation, (3a) and (3b), respectively, first proposed in 1914 by Maxime Bôcher, former president of the American Mathematical Society [5].

The classical Smith chart is mapped in the northern hemisphere [Figure 3(a)]; the circuits with negative resistance, exhibiting $|\rho| > 1$, are mapped in the southern hemisphere in Figure 3(b). The 3D chart's properties are listed in Table 2. Figure 4 presents the 3D Smith chart, showing its key points in a one-to-one comparison with the Smith chart and Earth. Table 2 lists its properties and Table 3 its possible advantages and drawbacks.

Figure 5 represents the 3D Smith chart and the Smith chart rendered with constant *r*, *x*, *g*, and *b* (susceptance circles). The CAD tool in which it is (or may be) implemented allows the viewer to rotate it in any convenient way for the desired application.

Table 3 lists the various properties of the Smith chart and 3D Smith chart. Figure 5 shows the 3D Smith chart rendered with the constant normalized resistance, reactance (x), conductance (g), and susceptance circles (b) in comparison with the Smith chart. The $r, g \in (0, \infty)$ for the Smith chart while $r, g \in (-\infty, \infty)$ for the 3D Smith chart.

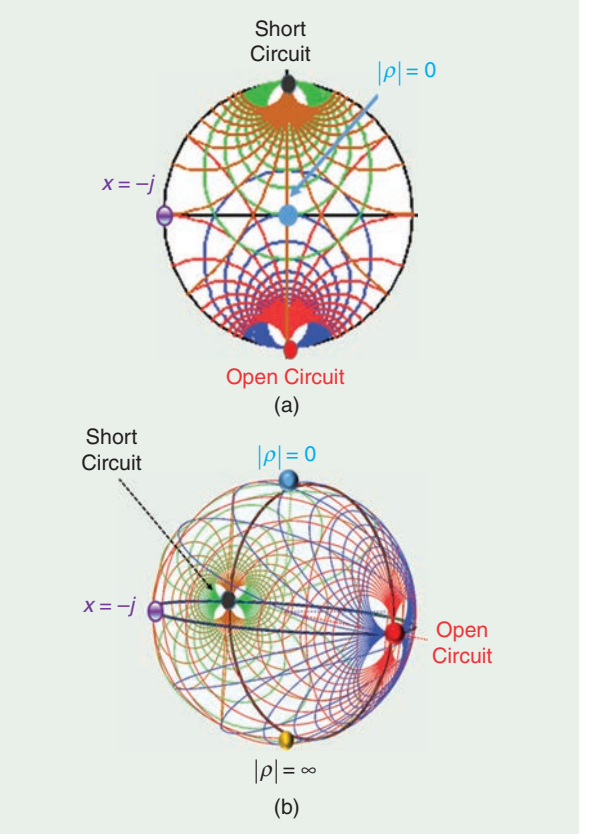

Figure 5. *(a) A Smith chart and (b) a 3D Smith chart rendered with r, x, g, and b circles.*

Matching a Network on the Chart Surface

To match the desired network, one must intersect the $r = 1$ or $g = 1$ circles, which pass through the origin of the Smith chart in Figure 6(a) or through the north pole of the 3D Smith chart [Figure 6(b)]. When the north pole

On the 3D Smith chart, the orientation is best visualized as if the viewer were a person walking on the surface with his or her feet on the circles.

is reached, matching is achieved. The matching procedure is identical to that used in 2D; the designer simply has to move on the constant r and constant g circles or on the constant reflection-coefficient circles (latitude) to intersect the $r = 1$ and $g = 1$ circles in the fashion desired. Figure 6(c) presents a variety of matching strategies and their circuital meaning while moving on the constant r, g circles in opposed directions. On the 3D Smith chart, the orientation is best visualized as if the viewer were a person walking on the surface with his or her feet on the circles.

Example 1: Matching a Given Passive Network

To match a load of $10 + j10$ to a 50-Ω line with L, C networks, we normalize to 50 Ω and get $z = 0.2 + j0.2$. Figure 7 presents schematically the matching of a $z = 0.2 + 0.2j$ network with various circuits. The values of these elements can be easily computed as on the 2D Smith chart, keeping in mind the coordinates of the points and (2).

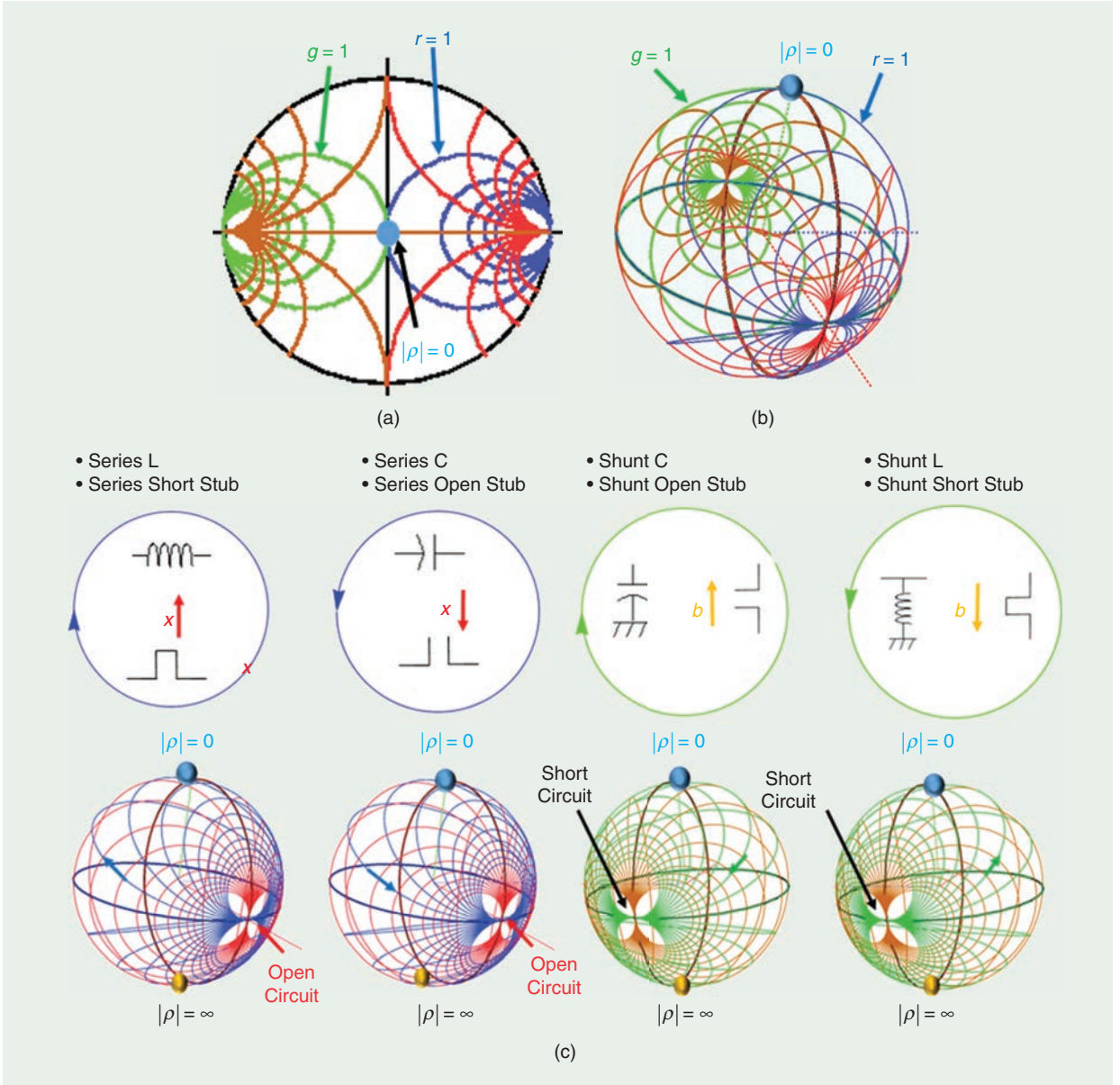

Figure 6. *Matching a network. (a) A Smith chart's g=1 and r = 1 circles, (b) a 3D Smith chart's g = 1 and r = 1 circles, and (c) moving along g and r constant circles on the 3D Smith chart in a clockwise- and counterclockwise-circuital correspondence.*

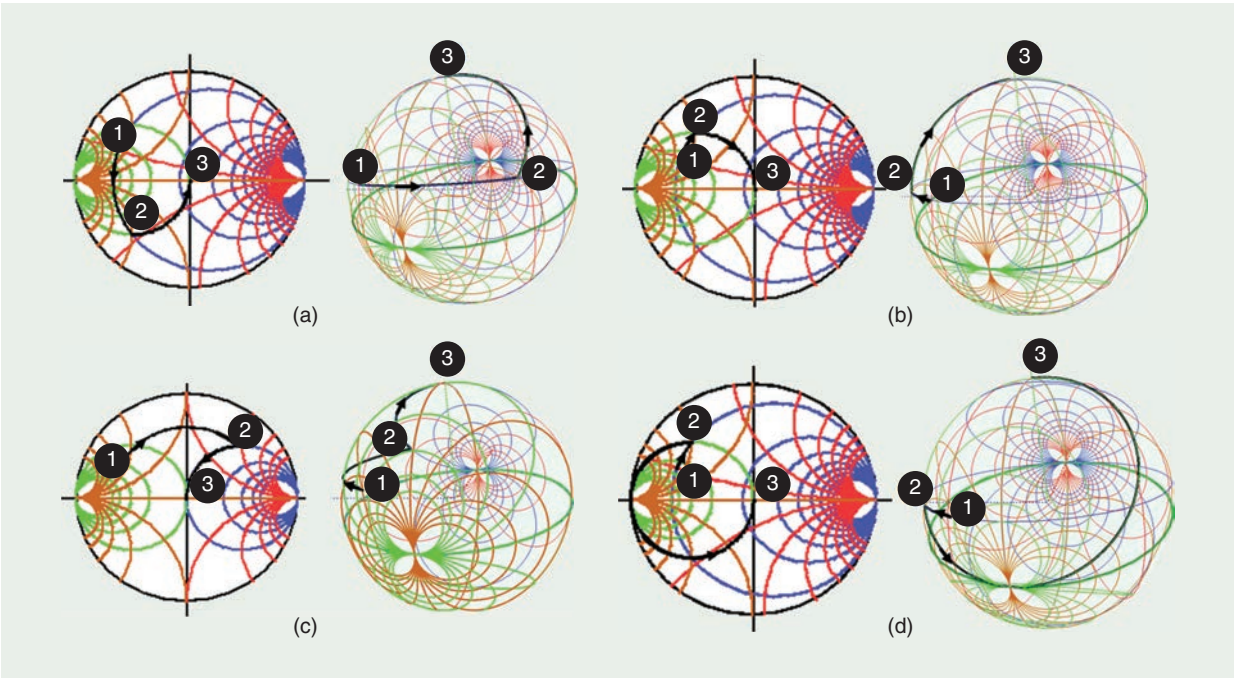

Figure 7. *The step-by-step matching of a 0.2 + 0.2j load using four different paths, that is, (a), (b), (c), and (d), on the Smith and 3D Smith charts, respectively.*

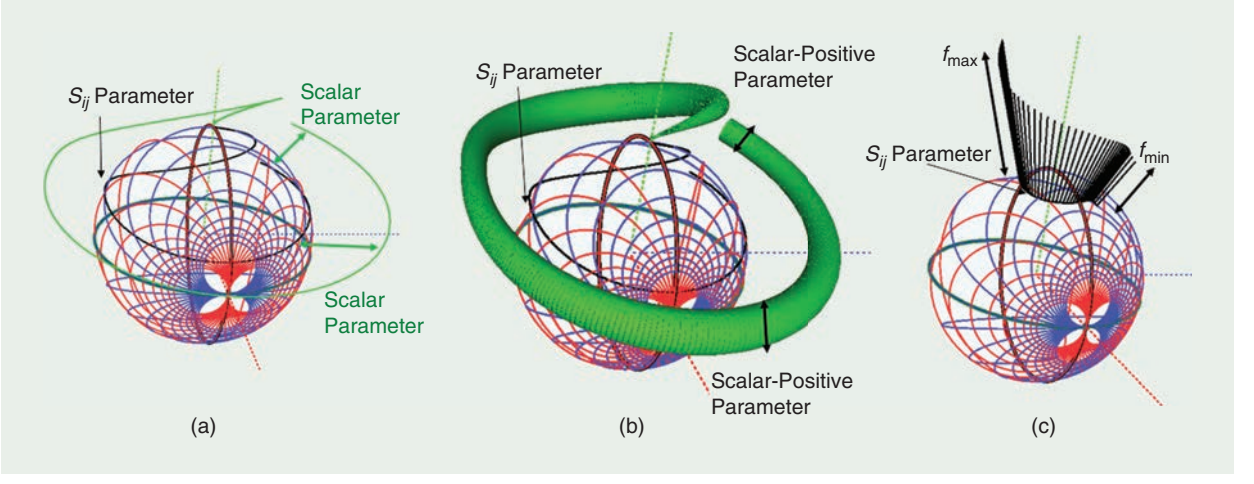

Figure 8. *3D space representations of scalar values. (a) A parameter with possible positive (the exterior of the 3D chart) and negative values (the interior of the 3D chart) (group delay). (b) Only the positive values are shown as a generalized cylinder with variable radii. (c) A frequency display graphing the dynamics of the S-parameters.*

Figure 7(a)–(d) shows the following: a series capacitance and shunt inductance, series L and shunt C, a lossless transmission line (moving on a latitude circle) and shunt short stub, and a lossless transmission line and shunt short stub.

3D Space Rendering Above the 3D Smith Chart Used for Both Passive and Active Circuits

Figure 8 synthesizes the main rendering schemes proposed for displaying a variety of frequency-dependent parameters simultaneously with *S*-parameters, which are always displayed on the surface. Figure 8(a) shows the rendering that applies for the display of group delay and series- and shunt-inductance models. Mapping from the center of the sphere using variable homothety [15], [19] maps these values closer or further away from its surface (for each frequency point), corresponding to the normalized values displayed. If the values become negative, the values are mapped in the interior of the chart. Another positive scalar value that is dependent on

The topology of the 3D Smith chart allows for multiple parameter visualizations that can potentially speed up the design/characterization of passive circuits, while giving new insights.

the previous value is displayed as the variable radius of a generalized cylinder along the previously presented variable [Figure 8(b)]. Figure 8(c) depicts the proposed frequency display as the distance from the corresponding S_{ij} parameter (with a reference system in the center of the sphere).

Inductors: Characterization of Multiple Simultaneous Parameters

The topology of the 3D Smith chart allows for multiple parameter visualizations that can potentially speed up the design/characterization of passive circuits, while giving new insights. The authors of [19] report reconfigurable inductors with the phase-change material vanadium dioxide (VO_2) as the switching material between insulating and conductive states with temperature control. Such programmable inductors outperform the inductors reported in [20] and [21], which use the same material, in terms of quality (Q) in the conductive state of VO_2. The VO_2 switch length of fewer than 635 nm minimizes its limited conductivity effects in [20], and (Q) factors of roughly seven were achieved (unlike three in [20] or below unity in [21]) while using VO_2.

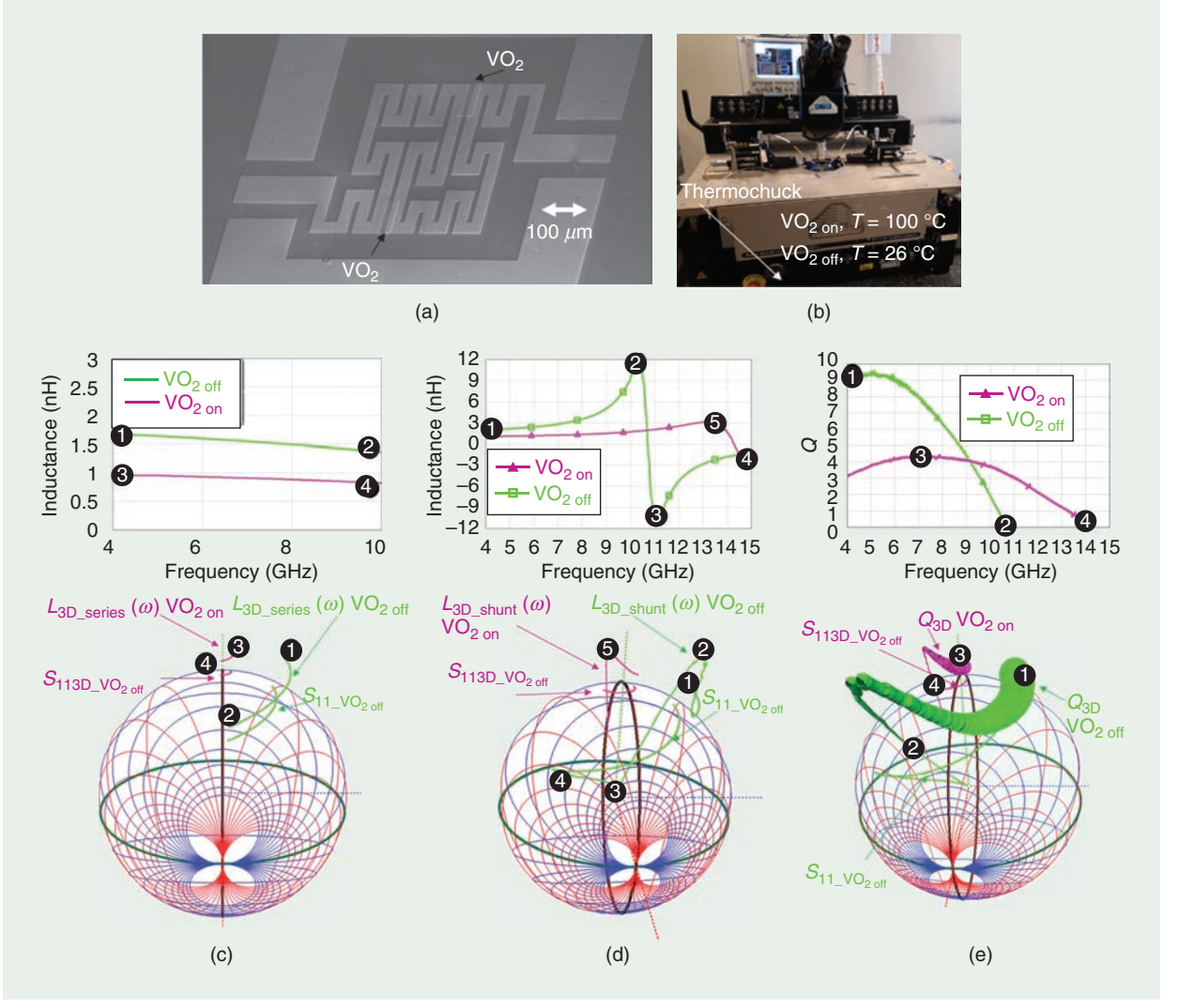

Figure 9. *(a) An inductor with VO_2 switches in a fabricated photo. (b) An S-parameter measuring setup with a heater for VO_2 on/off activation using the in-house Anritsu VectorStar VNA. (c) A series-inductance display over the S-parameters, (d) a shunt-inductance display over the S-parameters, and (e) a Q-factor display over the shunt-inductance curve. Q: quality.*

Here we present other inductors with a 1.6-µm switch length and their corresponding performances in on/off states measured with the Anritsu Vector Star vector network analyzer and extracted using its incorporated software (Microwave Office) and our GUI. The results reported in Figure 9 improve upon the results reported in [19] in terms of insulating-state (off-state) performance while performing less well in the on state (because the 1.6-um length of the VO_2 switch accentuates the on-state losses). Figure 9(a) shows the layout of the inductor, which is the same as in [19] (but with a larger switch); Figure 9(b) depicts the measurement setup, including a heater to activate the VO_2. The extracted series inductance (based on the Y_{21} admittance parameter) [20], [21] is shown in Figure 9(c); the extracted shunt inductance is shown in Figure 9(d) [22] (based on the Y_{11} parameters), while Q is displayed in Figure 9(e). All of these are displayed on both a 2D plot and a 3D Smith chart together with the corresponding $S_{113D}(j\omega) = \rho_{3D}(j\omega)$ parameters.

The 3D representations are based on the models presented in Figure 8(a) and (b). For the 3D representation of the series and shunt inductance, the normalized (L_N) values are first computed on the given frequency range of the display. The ρ_{3D} (2) is used and, at each frequency point, the 3D inductance curve is computed using the following formula:

$$L_{3d}(\omega) = (L_N(\omega) + 1)^* \, \rho_{3D}(j\omega). \tag{4}$$

In Figure 9(c)–(e), multiple Touchstone files are represented (series and shunt), then the maximum of the series and shunt inductance is used in the normalization step to obtain the normalized values across the different states displayed. The Q factor Q_{3D} is displayed as a generalized cylinder along the $L_{3d}(\omega)$ curve, with the variable radius corresponding to its value at the given frequency point normalized through its maximum over the display range [19]. When this becomes negative, the cylinder radius becomes 0.

Stability Circles—Inversive Transformations

The stability of an amplifier, or its resistance to oscillation, is a very important consideration in its design and can be determined from the *S*-parameters, matching networks, and terminations.

Some passive loads and source terminations can produce input and output impedances that have negative real parts; oscillations are possible under these circumstances. A designer would aim for unconditional stability: that is, for possible loads and source terminations, the amplifier should not produce negative real parts of its input and output impedance.

A graphical way to check this, and thus to ensure unconditional stability, is to make certain that the load

Some passive loads and source terminations can produce input and output impedances that have negative real parts; oscillations are possible under these circumstances.

(input) stability and source (output) stability circles are mapped in the exterior of the Smith chart (both their centers and all their points) [16], [23]. The positions of these circles are given by (5a), (5b), and (6), where z denotes the unit circle and Δ the determinant of the two-port *S*-parameters [23] (7).

Writing (5) as (6), we can see that we have an inversive transformation of z, where z is the unit circle. Geometrically, for (5b), we have step (a) translation of the unit circle with Δ/S_{22}, step (b) inversion in the unit circle, step (c) dilatation with abs $(S_{12}S_{21}/S_{22}^2)$, and step (d) rotation with arg $(S_{12}S_{21}/S_{22}^2)$:

$$t(z) = \frac{z - S_{11}}{S_{22}z - \Delta}, \tag{5a}$$

$$p(z) = \frac{S_{22} - z}{\Delta - S_{11}z}. \tag{5b}$$

$$t(z) = \frac{1}{S_{22}} - \frac{\frac{S_{12}S_{21}}{S_{22}^2}}{z - \frac{\Delta}{S_{22}}}, \tag{6a}$$

$$p(z) = \frac{1}{S_{11}} + \frac{\frac{S_{21}S_{12}}{S_{22}^2}}{z - \frac{\Delta}{S_{11}}}. \tag{6b}$$

$$\Delta = S_{11} * S_{22} - S_{21} * S_{12}. \tag{7}$$

In the rather unusual but possible situation that $|\Delta/S_{22}| = 1$, step (a) will translate the unit circle in (5b) into a circle passing through the origin in a point. Step (b) will then map this circle into an extended line passing through infinity (as inversions in circles passing through the origin result in infinite lines), and steps (c) and (d) will not change this any further, resulting in an extended line. The same things occur with (6b) for $|\Delta/S_{11}| = 1$; thus, theoretically, one can deal with circles or extended lines within the 2D complex reflection coefficients plane for (5) and (6).

On the 3D Smith chart there are no exceptions: (5) and (6) are inversive transformations of the unit circle; if $|\Delta/S_{22}| = 1$ or $|\Delta/S_{11}| = 1$, both (5) and (6) will generate circles passing through the south pole.

To ease the use of stability circles once their centers are mapped toward infinity (and thus become impossible to visualize on a 2D Smith chart), we propose the use of the 3D Smith chart for checking the stability in a compact and general way.

Example 2: Stabilize a Transistor With a Shunt Resistor

The following example shows how a resistive loading can stabilize a potentially unstable transistor using the graphical methodology presented in the previous section. To test it, we also compute the values of classical stability coefficients in both situations.

Determine the resistive load that can stabilize the transistor with the following *S*-parameters presented in Table 4 at 800 MHz [16, pp. 227], and plot the stability circles in both situations. The stability circles can be seen in Figure 10(a) and (b) on the 3D Smith chart. To see the values needed for r and g to stabilize the input stability circle (black), we change the rendering for r, x and g, b and detect the values needed.

Stability tests for the transistor presented in Table 5 based on the Rollet (8) equation [16], [24], [25] show $k = 0.54$ with $|\Delta| = 0.50$, or the more compact versions [26] given in (9) result in $\mu_1 = 0.85$, thus providing a violation of the conditions:

$$k = \frac{1 + |\Delta|^2 - |S_{11}|^2 - |S_{22}|^2}{2|S_{12} * S_{21}|} > 1 \text{ and } |\Delta| =< 1, \quad (8)$$

$$\mu_1 = \frac{1 - |S_{11}|^2}{|S_{22} - S_{11}^* \Delta| + |S_{12} * S_{21}|} > 1. \quad (9)$$

Moreover, as k is smaller than unity, the stability circles cross the boundary of the Smith chart [25] or the equator of the 3D Smith chart; our aim is to shift their centers and all of their points outside of the northern hemisphere. Figure 11(a) and (b) shows the stability circles' positions once the transistor is stabilized, which correspond to the *S*-parameters in Table 4. Adding a shunt resistor of 500 Ω, the new *S*-parameters can stabilize the transistor (schematic view in Figure 11) exhibiting the *S*-parameters in Table 4, providing $k = 1.04$ with $|\Delta| = 0.40$ and $\mu_1 = 1.02$, which is thus unconditionally stable, according to (9).

Power Gain Circles—Pure Euclidean Geometry in 3D

Unilateral transducer constant power gain circles play an essential role in the design of RF amplifiers and active modulators because they help to determine optimal impedance-matching conditions to meet gain and stability specifications. Unilateral transducer constant power gain circles (for the source input in our example) are a subfamily of Apollonius circles with respect to $S_{11}*$ and $1/S_{11}$. Plotting these gain circles on the 3D Smith chart overcomes traditional limits associated with contour plots on the traditional 2D Smith chart [14].

TABLE 4. S-parameters of the given transistor with a shunt resistor connected.

$\|S_{11}\|$	Phase (°)	$\|S_{12}\|$	Phase (°)	$\|S_{21}\|$	Phase (°)	$\|S_{22}\|$	Phase (°)
0.65	–94	0.032	41.2	4.62	116.2	0.66	–36

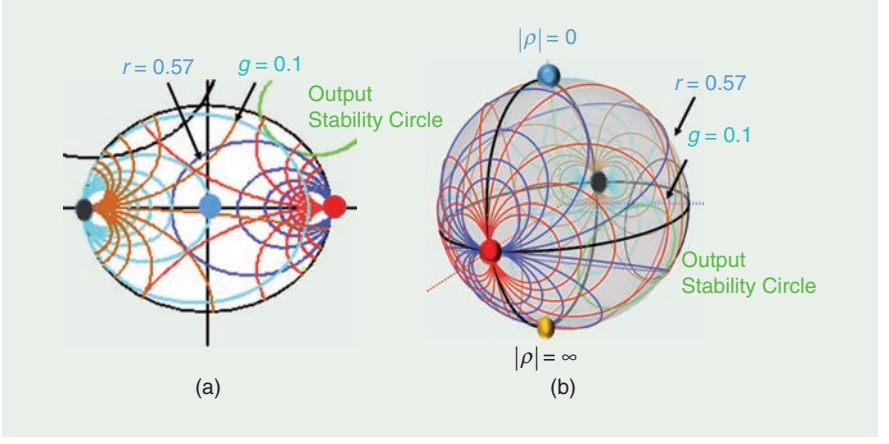

Figure 10. *Stability circles for the transistor described in Table 4 at 800 MHz (black input and green output). (a) The Smith chart and (b) the 3D Smith chart.*

TABLE 5. S-parameters of the given transistor.

$\|S_{11}\|$	Phase (°)	$\|S_{12}\|$	Phase (°)	$\|S_{21}\|$	Phase (°)	$\|S_{22}\|$	Phase (°)
0.65	–95	0.035	40	5	115	0.8	–35

Example 3

Consider the following bipolar junction transistor (BJT) *S*-parameters measured at 1 GHz [16] given in Table 6. The maximum achievable gain is $10(1/\text{Lg}\, 10\,(1/\text{Lg}|1 - S_{11}|^2) = 3.31$ dB. Plot the 3.31-dB constant power gain circles and the –2.27 power gain circles.

In Figure 12, we plot two gain circles corresponding to the values in Table 7 computed for the BJT transistor given in Table 6. The power level in 3D is normalized with respect to the square root of the maximum gain (for display reasons).

Example 4: Negative Capacitance

Negative capacitance [26]–[30] is of interest in many RF applications; however, the negative-capacitance and positive-inductance S_{11} parameters of one- and two-port lossless

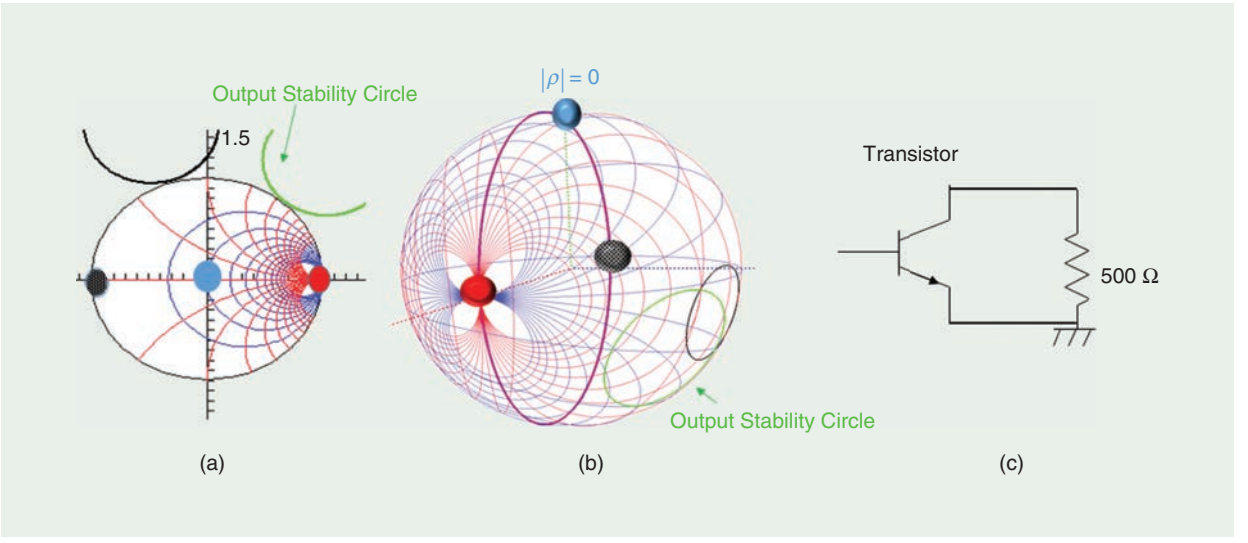

Figure 11. *A stabilized transistor with a 500-Ω resistor. (a) Stability circles on the Smith chart, (b) the 3D Smith chart, and (c) the stabilization scheme.*

TABLE 6. The BJT S-parameters at 1 GHz.

$\|S_{11}\|$	Phase (°)	$\|S_{12}\|$	Phase (°)	$\|S_{21}\|$	Phase (°)	$\|S_{22}\|$	Phase (°)
0.73	175	0	0	4.45	65	0.21	−80

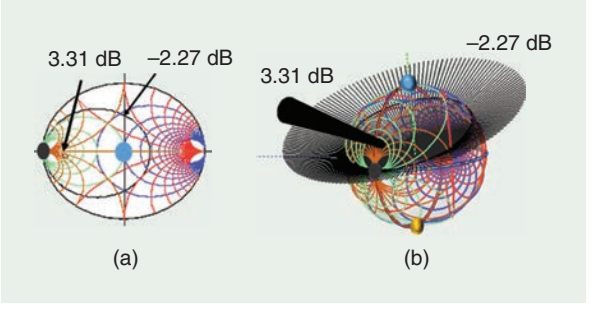

Figure 12. *The power gain circles for two different power levels on (a) a 2D Smith chart and (b) a 3D Smith chart.*

TABLE 7. BJT S-parameters at 1 GHz.

Gain (dB)	Gain (dB)	Gain ^.5
3.31	2.15	1.46
1.78	1.51	1.23
0	1	1
−2.27	0.6	0.77

networks share the same paths on the Smith chart. By means of differential geometry, however, we can see that their orientation (oriented curvature [20] of their frequency S_{11}) in either one- or two-port configurations is opposed. Their Foster/non-Foster character [27]–[30] changes the orientation of their S_{11} motions as frequency increases on the Smith chart.

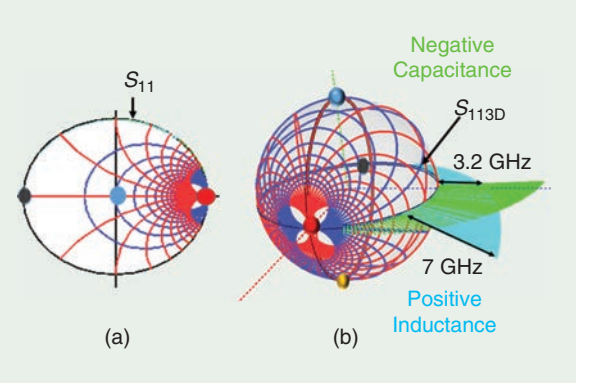

Figure 13. *Negative-capacitance and positive-inductance reflection coefficients on (a) a 2D Smith chart and (b) a frequency-dependent 3D Smith chart.*

Figure 13(a) represents the S_{11} of a negative capacitor and positive inductor in a one-port configuration with a 50-Ω load at both ports analyzed from 1 to 7 GHz. The implementation in [19] distinguishes the different intrinsic natures (the opposed sign of oriented curvatures) of both by representing the sweeping frequency dependency in 3D, as displayed in Figure 13(b). In this representation, we can detect not only the path but also the dynamics of the motion. The frequency representation in [19] allows the quantitative display of the frequency in 3D as the distance from the 3D Smith chart for each S_{11} point. The counterclockwise-frequency

Unilateral transducer constant power gain circles (for the source input in our example) are a subfamily of Apollonius circles with respect to S_{11}^* and $1/S_{11}$.

increase motion is clearly detected in Figure 13(b) for the negative capacitance, thus proving its different nature with respect to a conventional positive inductor. Even though its S_{11} parameters coincide on the Smith chart on a large frequency range with the S_{11} parameters of a conventional positive inductor, Figure 13(b) detects the different intrinsic nature of the negative capacitance.

Example 5: Negative-Resistance Circuits

Let us consider a negative-resistance phenomenon [31], such as the one observed in tunnel diodes [32] (Esaki diodes), which have been employed in active circuit design since 1957. Figure 14(a) depicts a small signal-equivalent circuit [4] consisting of negative resistance R, unavoidable shunt capacitance C, series inductance L, and series resistance R_s. With the additional presence of a very lossy package, including the presence of additional parasitic [33] R_p, L_p, and C_p and taking into account the values depicted in Figure 14, compute the input impedance (Z_{in}) at 2 GHz.

Figure 14(b) depicts the computation procedure using the 3D Smith chart by means of normalized values to 50 Ω (0.02 S). The input-normalized impedance detected with the 3D Smith chart is $z_{in} = 1/(g + jb) \simeq 0.037 - 0.147j$; thus, $Z_{in} \simeq -1.85 - j7.35$.

Conclusions

This article reported on the historical evolution of the Smith chart and its current extension and analytical generalization as a 3D tool. We illustrated the

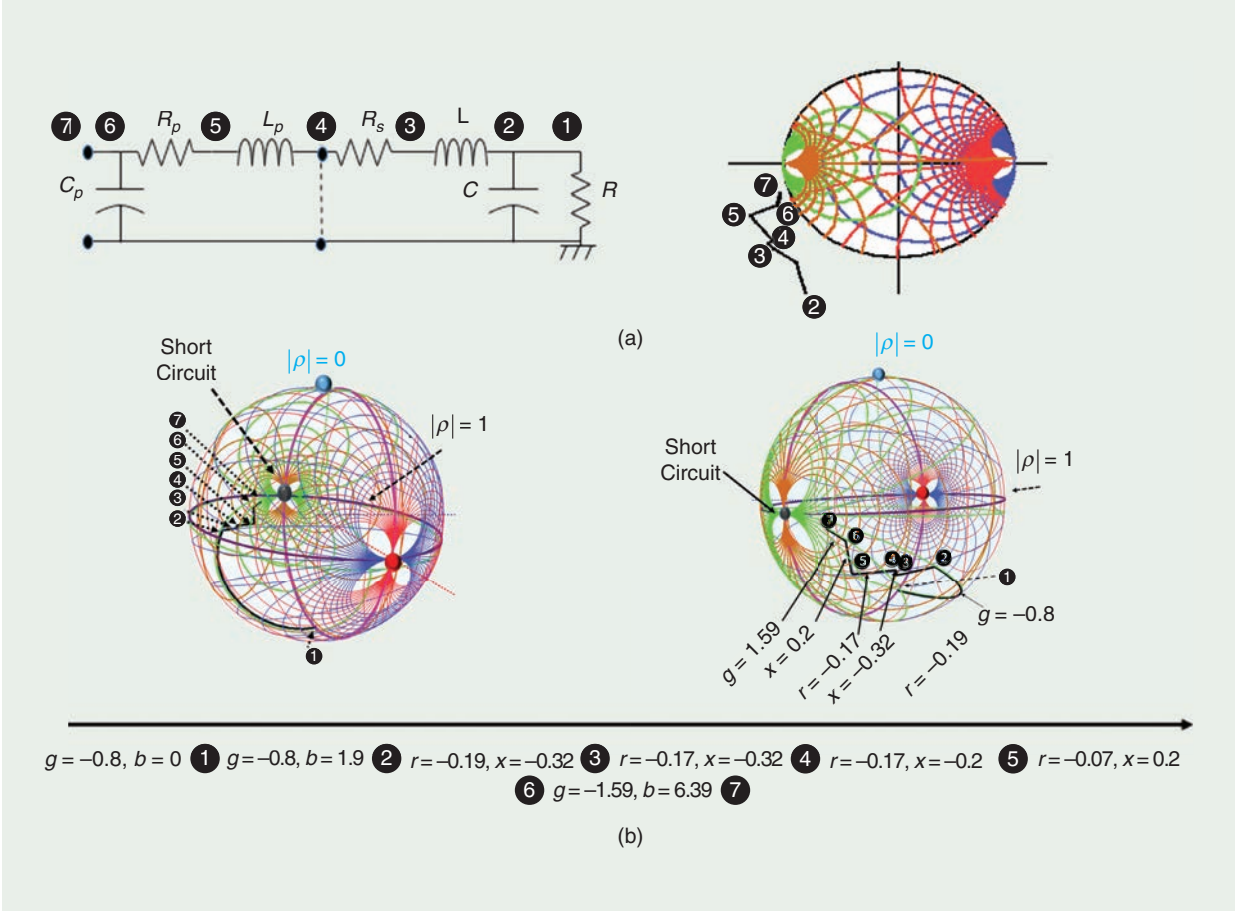

Figure 14. *(a) A tunnel diode-equivalent circuit, including the packaging at 2 GHz with $R = -62.5\ \Omega$ ($g = -0.8$), $C = 3$ pF ($b = 1.9$), $L = 0.5$ nH ($x = 0.126$), $R_S = 1\ \Omega$ ($r = 0.02$), $L_p = 0.5$ nH ($x = 0.126$), $R_p = 5\ \Omega$ ($x = 0.1$), and $C_p = 3$ pF ($b = 1.9$), along with its Smith-chart impedance in different points. (b) A 3D Smith chart impedance computation seen from two perspectives.*

theoretical development, refinement, and capabilities of the 3D Smith chart using a series of examples from passive to active components, including concepts such as negative-resistance and negative-capacitance circuits. For all of the selected examples, we used the same basic mathematical formulations, and we have reported how inversive-differential geometry theory can be used to develop an engineering tool that enhances the visualization capability of traditional Smith charts and offers new insights into the design of RF devices and circuits.

Acknowledgments

Portions of this article were supported by the HORIZON2020 FETOPEN PHASE-CHANGE SWITCH project under grant 737109 and the PGC2018-094889-B-100 grant. We especially thank Prof. Robert Caverly, Assistant Editor Sharri Shaw, the Editorial Board, and reviewers for their very helpful suggestions, constructive critiques, and corrections throughout the entire review process. Finally, we would like to thank Prof. Ke Wu for encouraging us to write an article on this topic as well as Dolores Gonzalez Demenchenko for her help with Figure 1.

References

[1] R. W. Rhea, *Preface of Electronic Applications of the Smith Chart*, 2nd ed. New York: Noble, 2000.

[2] P. H. Smith, "Transmission-line calculator," *Electronics*, vol. 12, no. 1, pp. 29–31, Jan. 1939.

[3] P. H. Smith, "An improved transmission line calculator," *Electronics*, Jan. 1944.

[4] P. H. Smith, *Electronic Applications of the Smith Chart*. New York: McGraw Hill, 1969.

[5] M. Bocher, "Infinite regions of various geometries," *Bull. Amer. Math. Soc.*, vol. 20, no. 4, pp. 185–200, 1914. doi: 10.1090/S0002-9904-1914-02463-2.

[6] R. L. Kyhl, "Plotting impedances with negative resistive components," *IEEE Trans. Microw. Theory Techn.*, vol. MTT-8, no. 3, p. 377, May 1960. doi: 10.1109/TMTT.1960.1125249.

[7] S. Gupta, "Escher's art, Smith chart, and hyperbolic geometry," *IEEE Microw. Mag.*, vol. 7, no. 5, pp. 67–76, Oct. 2006. doi: 10.1109/MW-M.2006.247916.

[8] C. Zelley, "A spherical representation of the Smith chart," *IEEE Microw. Mag.*, vol. 8, no. 3, pp. 60–66, June 2007. doi: 10.1109/MMW.2007.365060.

[9] Y. Wu, H. Huang, Y. Liu, and Z. Gao, "Spherical representation of omnipotent Smith chart," *Microw. Opt. Technol. Lett.*, vol. 50, no. 9, pp. 2452–2455, Sept. 2008. doi: 10.1002/mop.23689.

[10] Y. Wu, Y. Zhang, Y. Liu, and H. Huang, "Theory of the spherical generalized Smith chart," *Microw. Opt. Technol. Lett.*, vol. 51, no. 1, pp. 95–97, Jan. 2009. doi: 10.1002/mop.23999.

[11] D. A. Brannan, M. F. Esplen, and J. J. Gray, *Geometry*. New York: Cambridge Univ. Press, 2007.

[12] A. A. Muller, P. Soto, D. Dascalu, D. Neculoiu, and V. E. Boria, "A 3D Smith chart based on the Riemann sphere for active and passive microwave circuits," *IEEE Microw. Wireless Compon. Lett.*, vol. 21, no. 6, pp. 286–288, June 2011. doi: 10.1109/LMWC.2011.2132697.

[13] A. A. Muller, P. Soto, D. Dascalu, and V. E. Boria, "The 3D Smith chart and its practical applications," *Microw. J.*, vol. 55, no. 7, pp. 64–72, July 2012.

[14] A. A. Muller et al., "Apollonius unilateral transducer constant power gain circles on the 3D Smith chart," *IET Electron. Lett.*, vol. 50, no. 21, pp. 1531–1533, Oct. 2014. doi: 10.1049/el.2014.2695.

[15] A. A. Muller, E. Sanabria-Codesal, A. Moldoveanu, V. Asavei, and S. Lucyszyn, "Extended capabilities of the 3-D Smith chart with group delay and resonator quality factor," *IEEE Trans. Microw. Theory Techn.*, vol. 65, no. 1, pp. 10–19, Jan. 2017. doi: 10.1109/TMTT.2016.2614931.

[16] G. Gonzalez, *Microwave Transistor Amplifiers Analysis and Design*, 2nd ed. Englewood Cliffs, NJ: Prentice Hall, 1996.

[17] B. C. Wadell, "Smith charts are easy-Part 1," *IEEE Instrum. Meas. Mag.*, vol. 2, no. 1, pp. 37–40, 1999. doi: 10.1109/5289.754758.

[18] B. C. Wadell, "Smith charts are easy-Part 2," *IEEE Instrum. Meas. Mag.*, vol. 2, no. 2, pp. 45–47, 1999. doi: 10.1109/5289.765969.

[19] A. A. Muller et al., "3D Smith charts scattering parameters frequency-dependent orientation analysis and complex-scalar multiparameter characterization applied to Peano reconfigurable vanadium dioxide inductors," *Sci. Rep.*, vol. 9, no. 1, pp. 1–15, Dec. 2019. doi: 10.1038/s41598-019-54600-5.

[20] E. A. Casu, A. A. Muller, M. Cavalieri, A. Fumarola, A. M. Ionescu, and M. Fernandez-Bolaños, "A reconfigurable inductor based on Vanadium Dioxide insulator to metal transition," *IEEE Microw. Wireless Compon. Lett.*, vol. 28, no. 9, pp. 795–797, 2018. doi: 10.1109/LMWC.2018.2854961.

[21] S. Wang, W. Wang, E. Shin, T. Quach, and G. Subramanyam, "Tunable inductors using vanadium dioxide as the control material," *Microw. Opt. Techn. Lett.*, vol. 59, no. 5, pp. 1057–1061, 2017. doi: 10.1002/mop.30459.

[22] J. Kang et al., "On-chip intercalated-graphene inductors for next-generation radio frequency electronics," *Nature Electron.*, vol. 1, no. 1, pp. 46–51, 2018. doi: 10.1038/s41928-017-0010-z.

[23] J. F. White, *High Frequency Techniques: An Introduction to RF and Microwave Engineering*. Hoboken, NJ: Wiley, 2004

[24] M. J. Rollet, "Stability and power-gain invariants of linear two-ports," *IRE Trans. Circuit Theory*, vol. 9, no. 1, pp. 29–32, Mar. 1962. doi: 10.1109/TCT.1962.1086854.

[25] M. L. Edwards and J. H. Sinsky, "A new criterion for linear 2-port stability using a single geometrically derived parameter," *IEEE Trans. Microw. Theory Techn.*, vol. 40, no. 12, pp. 2303–2310, Dec 1992. doi: 10.1109/22.179894.

[26] A. M. Ionescu, "Negative capacitance gives a positive boost," *Nature Nanotechnol.*, vol. 13, no. 1, pp. 7–8, 2018. doi: 10.1038/s41565-017-0046-2.

[27] H. Mirzaei and G. V. Eleftheriades, "Realizing non-Foster reactive elements using negative-group-delay networks," *IEEE Trans. Microw. Theory Techn.*, vol. 61, no. 12, pp. 4322–4332, Dec. 2013. doi: 10.1109/TMTT.2013.2281967.

[28] A. A. Muller and S. Lucyszyn, "Properties of purely reactive Foster and Non-Foster passive networks," *IET Electron. Lett.*, vol. 51, no. 23, pp. 1882–1884, Nov. 2015. doi: 10.1049/el.2015.1429.

[29] A. M. Kemp, et al. "A high Q piezoelectric resonator as a portable VLF transmitter," *Nat. Commun.*, vol. 10, no. 1, p. 1715, 2019. doi: 10.1038/s41467-019-09680-2.

[30] M. M. Jacob, "Non-Foster circuits for high performance antennas: Advantages and practical limitations," Ph.D. thesis, UCSD, San Diego, CA, 2016. [Online]. Available: https://escholarship.org/uc/item/2pq549c3

[31] D. Dascalu, *Transit-Time Effects in Unipolar Solid-State Devices*. Tunbridge Wells, U.K.: Abacus Press, 1972.

[32] A. M. Ionescu and H. Riel, "Tunnel field-effect transistors as energy-efficient electronic switches," *Nature*, vol. 479, no. 7373, pp. 329–337, 2011. doi: 10.1038/nature10679.

[33] K. Ishii, *Practical Microwave Electron Devices*. San Diego, CA: Academic, 1990.

Periodic Structures With Higher Symmetries

Oscar Quevedo-Teruel, Guido Valerio, Zvonimir Sipus, and Eva Rajo-Iglesias

Higher symmetries frequently amaze human beings because of the illusions and incredible landscapes such symmetries can produce. For example, imagine the unearthly pictures of the Dutch graphic artist M.C. Escher. He made use of glide symmetry and reflection to produce unbelievable transitions and transformations of objects and beings, as illustrated in Figure 1(a). However, the history of higher symmetries started much earlier. Escher was partially inspired by the Moorish tessellations in the Alhambra in Granada, Spain, such as the ones pictured in Figure 1(b).

Oscar Quevedo-Teruel (oscarqt@kth.se) is with the Division of Electromagnetic Engineering, KTH Royal Institute of Technology, Stockholm, Sweden. Guido Valerio (guido.valerio@sorbonne-universite.fr) is with Sorbonne Université, CNRS, Laboratoire de Génie Electrique et Electronique de Paris, France, and the Université Paris-Saclay, CentraleSupélec, CNRS, Laboratoire de Génie Electrique et Electronique de Paris, Gif-sur-Yvette, France. Zvonimir Sipus (zvonimir.sipus@fer.hr) is with the Faculty of Electrical Engineering and Computing, University of Zagreb, Croatia. Eva Rajo-Iglesias (eva@tsc.u3m.es) is with the Department of Signal Theory and Communications, Carlos III University of Madrid, Spain.

Digital Object Identifier 10.1109/MMM.2020.3014987

Date of current version: 6 October 2020

 1527-3342/20©2020IEEE

Higher symmetries can be employed not only to create artistic creations but also as tools for a better description of space (e.g., in connection with numerical problems in space tessellation and meshing [1] and for enhancing the performance of electromagnetic devices). Here, we explain the importance of the recently discovered electromagnetic properties of higher symmetries as well as their implications and opportunities for microwave and antenna engineers.

Higher Symmetries in Electromagnetic History: Back to the 1960s

Narrowing our scope to physics, higher symmetries were very popular during the 1960s. For example, George L. Trigg wrote in 1965 that "in the last few months, scarcely an issue of *Physical Review Lett*. has failed to contain at least one paper on the topic" [2], demonstrating the volume of studies at the time. If we are even more specific and focus our attention on electromagnetic engineering, the first studies of higher symmetries, mostly on periodically loaded waveguide structures, arrived during the middle of the 1960s [3], [4], and they were popular for one decade, until the mid-1970s [5], [6]. However, during the 1970s, the electromagnetic engineering community was not ready to further develop scientific studies of higher symmetries and understand the symmetries' full potential. First, computers were very basic, and there was no commercial software that could be used to simulate these complex structures. Second, our understanding of periodic structures achieved maturity during the 2000s, with the arrival of concepts such as metamaterials [7], [8] and metasurfaces [9], [10]. Finally, at the end of the 1970s and the beginning of the 1980s, electromagnetic engineers focused their attention on making wireless systems affordable for everybody, so printed and planar technologies were the selected solutions for low-cost communications at low frequencies [11].

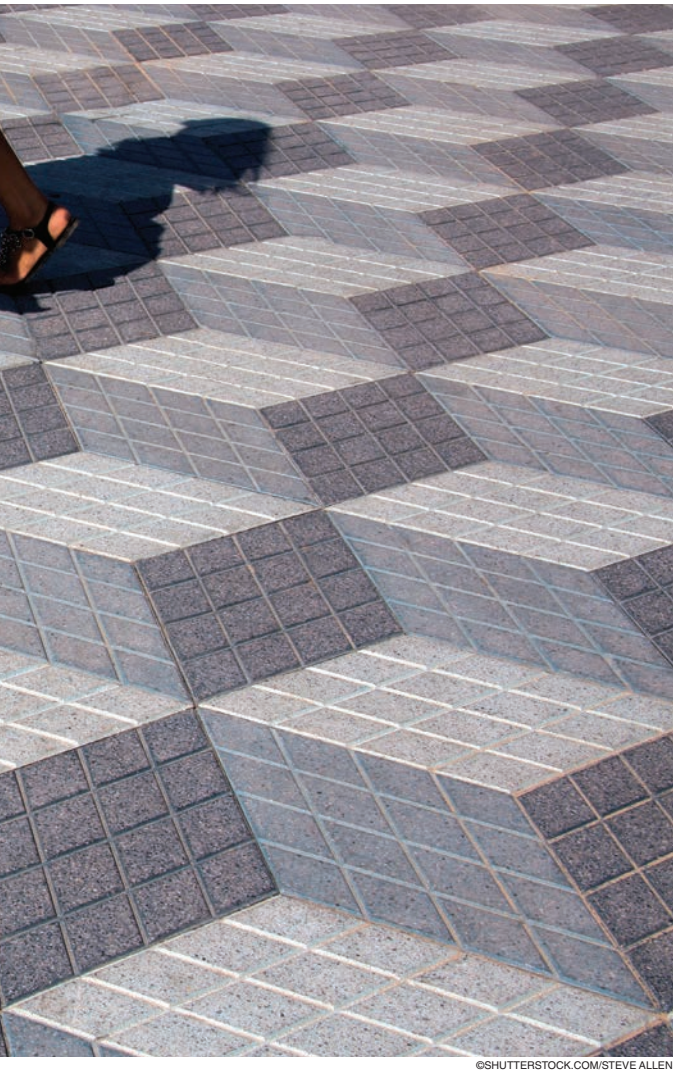

©SHUTTERSTOCK.COM/STEVE ALLEN

We are now entering the third decade of the 21st century, and powerful computers are easily accessible, commercial software for simulation is commonly available, and periodic structures are broadly understood thanks to studies on metamaterials and metasurfaces: the opportunity for higher symmetries has arrived. This opportunity is evolving as the industry demands electromagnetic systems operating at higher frequencies [12]. At these frequency ranges, there is a need for low-loss structures, which can be achieved only with fully metallic devices and integrated antennas and circuits [13].

In this situation, antennas based on leaky waves and lenses are gaining converts for communication designs in the new bands of 5G and satellite communications [14]. Although the design of these antennas is more complicated than the architecture of arrays, the antennas present a simpler feeding network. On the other hand, filters were traditionally designed as an independent unit connected to the rest of the system. Due to insertion loss and the losses in the interconnections [15], for high-frequency designs filters must be integrated with other components. Finally, because of these large losses, future components, such as filters, must be reduced in length. Therefore, design techniques that are not based on isolated elements but on coupled elements are required to reduce overall losses.

Definition of Periodic Structures With Higher Symmetries

A periodic unit cell possesses higher symmetries when it is invariant under a geometrical transformation that, iterated several times, gives the unit-cell translation. For example, a glide-symmetric unit cell is invariant after a translation and a mirroring [16]. A twist-symmetric unit cell is invariant after a translation and a rotation (or angular movement) [17].

Glide Symmetries

In Figure 1(c), we present the creation of a periodic structure through glide reflection. A unit cell, represented in blue, is filled with a triangle and a rectangle. One could repeat this unit cell with a simple translation, and one could also create a reflected unit cell that is alternated together with the translation. Glide symmetries can be 1D or 2D. In Figure 2(a) and (b), we represent two examples of 1D glide-symmetric structures: corrugations [18]–[20] and transversal slots [21], [22]. These two structures have glide symmetry with respect to the x direction; however, their mirroring planes are different. In the corrugations, this plane is horizontal, but, in the slots, it is vertical. In these cases, the glide operation is $x \rightarrow x + p/2$ and either $z \rightarrow -z$ in the corrugations or $y \rightarrow -y$ in the slot, with p as the periodicity in both cases.

A specific new case of glide symmetry was recently reported as *polar glide symmetry* [17], [23]. It refers to the case in which the mirroring surface is not defined with Cartesian coordinates but with polar ones. Therefore, the mirroring surface is orthogonal to a vector in the ρ direction [23], [24]. 2D glide-symmetric structures were first studied in [25], and they require translation in two orthogonal directions that are opposite the vector of the

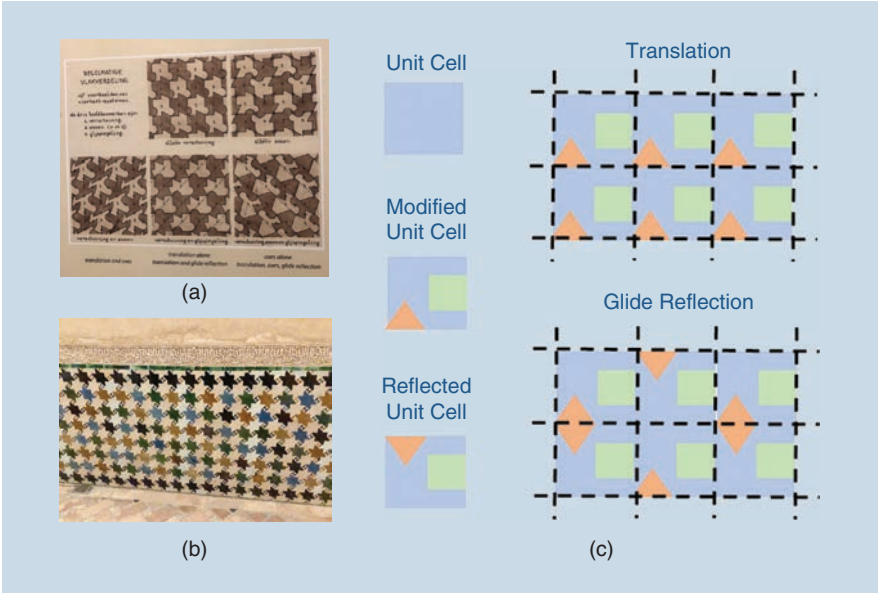

Figure 1. *Glide symmetries in art. (a) An explanation of glide reflection at the museum of M.C. Escher in The Hague, The Netherlands. (b) Moorish tessellations in the Alhambra, Granada, Spain. (c) Compositions made of translations and glide reflection.*

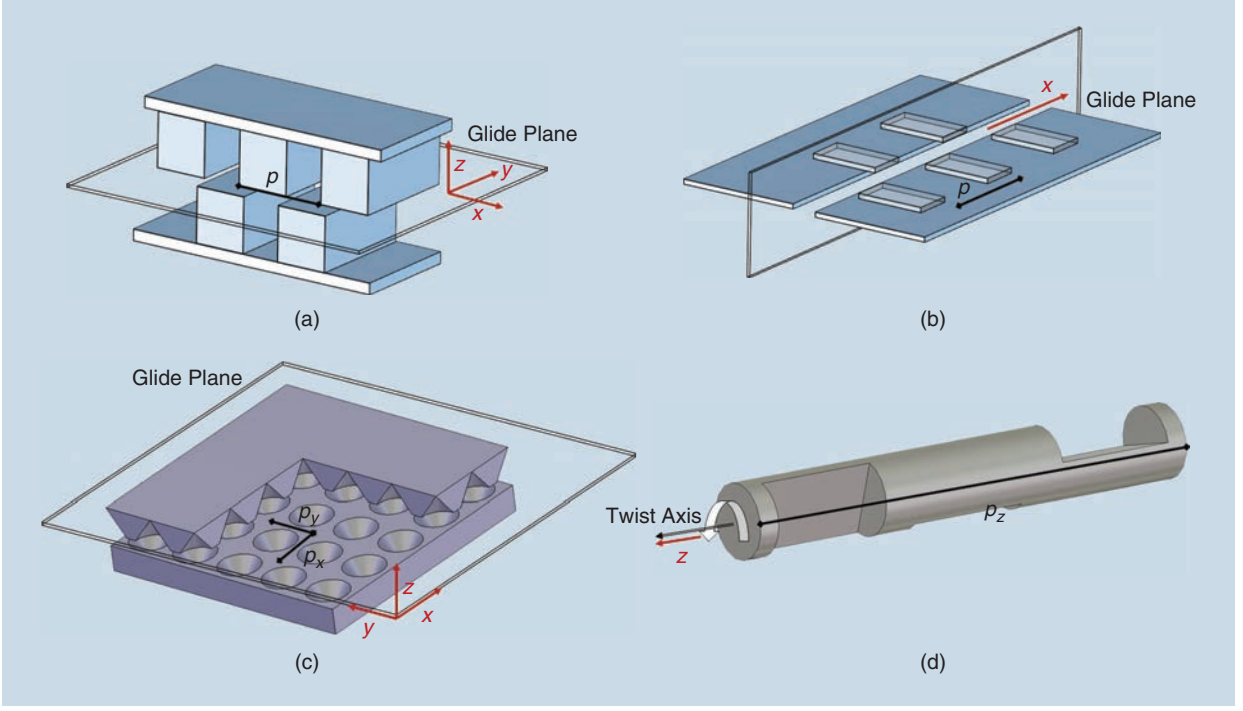

Figure 2. *Electromagnetic configurations of higher symmetries. (a) Glide-symmetric corrugations. (b) A slot with glide-symmetric transversal loads. (c) A 2D glide-symmetric holey structure. (d) A twist-symmetric holey configuration.*

mirroring plane. For example, a common glide operation can be $(x, y) \rightarrow (x + p_x/2, y + p_y/2)$ and $z \rightarrow -z$ [26], [27], with p_x and p_y as the periods in x and y, respectively. One example of 2D glide symmetry is illustrated in Figure 2(c) for conical holes inserted in two parallel plates.

Twist Symmetries

Twist-symmetric structures are those that are invariant under a translation in one direction. For example, Figure 2(d) illustrates a holey metallic wire oriented in the z direction, i.e., the propagation direction. The wire has holes that rotate through the z direction. A periodic structure possesses m-fold twist symmetry, with m being an integer, if it is invariant under a p/m translation and a $2\pi/m$ rotation around the twist direction, where p is the periodicity of the structure [23]. The particular case in Figure 2(d) is threefold. We must note that helices are a particular case of twist symmetry with $m = \infty$. Helices were studied in terms of dispersion properties during the 1950s [28]. For this reason, twist symmetry is also known as *helical symmetry* and *screw symmetry* [6].

Subperiodicities in Higher Symmetries

Introducing higher symmetries in periodic structures may drastically change the dispersion properties of those structures (i.e., how passbands and stopbands are distributed in the frequency domain). The basic property of higher-symmetric periodic structures concerns the possibility of closing selected bandgaps. This was previously discussed by Hessel et al. [6] during the early 1970s, with reference to 1D structures. Specifically, the presence of a glide symmetry with period p closes the first stopband at the edge of a Brillouin zone $\beta = \pi/p$, where β is the phase constant of a Bloch mode; an m-fold twist symmetry closes the first $m - 1$ stopbands, alternatively at $\beta = \pi/p$ and $\beta = 0$. More recently, the same spectral properties have been observed in 2D structures [26], [27].

For example, in a glide-symmetric structure, the absence of a stopband at $\beta = \pi/p$ can be easily explained if the effect of the periodic scatterers on the two sides of the glide plane is the same. This means that these scatterers can be moved on the same side of the plane, thus transforming the glide structure into an equivalent, purely periodic structure with a halved spatial period $p/2$. An example of such a 1D glide structure and its associated nonglide structure are depicted in Figure 3(a) and (b). The Brillouin diagram of this new nonglide periodic structure presents a first stopband edge at $\beta = \pi/(p/2) = 2\pi/p$, which is equivalent to the $\beta = 0$ point in the diagram of the glide structure. In other words, the glide structure is equivalent to a structure with a shorter period so that its first stopband is found at higher frequencies.

Higher symmetries can be employed not only to create artistic creations but also as tools for a better description of space (e.g., in connection with numerical problems in space tessellation and meshing and for enhancing the performance of electromagnetic devices).

However, the equivalence between scatterers on the two sides of the glide plane is not necessarily verified in all glide structures. To explain this phenomenon, let us decompose the Bloch mode supported by the glide structure into the modes of the uniform background structure. These modes are coupled together by periodic scatterers. In the glide structure of Figure 3(a), these scatterers are placed alternately on the two sides of the glide plane; in the periodic structure of Figure 3(b), they are all on the same side. On the one hand, if in both structures the scatterers are weakly interacting among one another, only one dominant mode is relevant in the coupling between adjacent scatterers. This happens if each scatterer mainly excites only one dominant background mode or if all the higher-order background modes excited by one scatterer are strongly attenuated when they reach the adjacent ones. In this case, the mutual position of two adjacent scatterers does not impact the coupling, which is the same whether both scatterers lie on the same side or on opposite sides of the glide plane. The glide structure is then reducible to the nonglide periodic structure with a halved spatial period [29].

An example of a reducible glide structure can be seen in Figure 3(c), where the glide and nonglide lines have the same dispersion diagram if their phase constants are normalized with respect to the same distance p (the period of the glide line). On the other hand, if in at least one of the two structures in Figures 3(a) and (b) the scatterers are strongly interacting, several background modes will be relevant for their coupling [30]. These modes will have, in general, different parity with respect to the glide plane; the odd and even modes will experience a different scattering according to the position of the scatterer with respect to the glide plane. This richer modal coupling in strongly coupled structures makes the glide-symmetric structure irreducible to the nonglide periodic one with a reduced spatial period [29]. An example of an irreducible glide structure appears in Figure 3(d), where the glide and nonglide periodic structures have different dispersion diagrams. The

same phenomena can be found in twisted structures, where the scatterers lie along a spiral, rather than on different sides of a plane [31].

Circuit Models to Analyze Glide-Symmetric Structures

Despite the recent interest in higher-symmetric structures, simplified models for the efficient design of these structures are not yet available. Specific models of higher-symmetric structures are needed because the application of full-wave numerical methods to this class of structures is difficult. Interesting dispersive behaviors, such as wideband response and strong bandgap rejection, require extreme values of geometrical parameters (e.g., very close glide surfaces to enhance their mutual interaction). In these cases, numerical methods encounter difficulties. For example, thin gaps between surfaces require a very dense localized meshing in finite-element and finite-difference methods, and they cause slow convergence in Green's functions in the method of moments. Furthermore, the study of finite structures made by a nonuniform array of thousands of subwavelength cells is a multiscale problem that requires ad hoc computation techniques.

Circuit Models

The availability of equivalent circuits for the unit cells of higher-symmetric structures would considerably simplify the structures' preliminary design. Based on the previous analysis, if a higher-symmetric structure is reducible to a non-higher-symmetric periodic structure, a monomodal equivalent circuit is sufficiently accurate to calculate its dispersion behavior. Furthermore, the model can be performed on only one subunit cell, and its non-higher-symmetric structure can be analyzed instead of the higher-symmetric structure. This was done in [19], where a 1D glide-symmetric corrugated structure [as illustrated in Figure 2(a)] was analyzed by means of an equivalent circuit derived from the T junction discontinuity [32]. In fact, the central horizontal waveguide region can be regarded as a parallel-plate waveguide (PPW) connected with a series of vertical corrugations, with each one equivalent to a PPW along the vertical direction. A unit cell can then

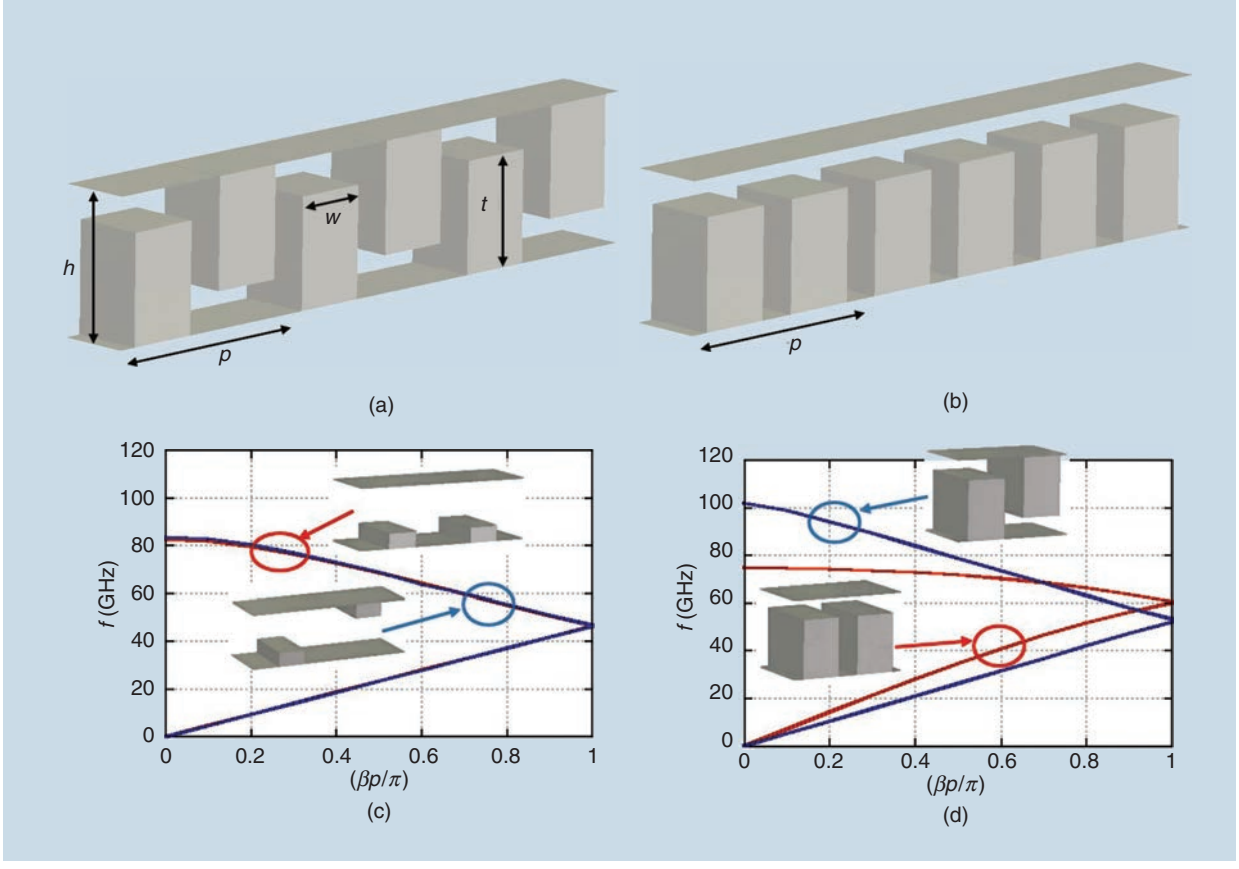

Figure 3. *(a) A structure with glide-symmetric corrugations along one direction. (b) An associated nonglide-symmetric structure with corrugations along one direction. (c) A Brillouin diagram of glide and nonglide structures with h = 1 mm, w = 0.5 mm, p = 3 mm, and t = 0.25 mm. (d) A Brillouin diagram of glide and nonglide structures with h = 1 mm, w = 0.5 mm, p = 1.5 mm, and t = 0.75 mm.*

be described as a composition of T junctions between parallel plates.

This kind of discontinuity has been widely studied and can be characterized with the closed-form scattering parameters found in [32]. The results of this equivalent circuit are extremely accurate for the full range of parameters used in current applications, as long as the unit cell keeps a T junction topology. This is no more valid in the glide-corrugated structure in Figure 3(a). More recently, a circuit model analysis was proposed to model glide-symmetric loaded microstrip lines [33]. This model accurately explains the coupling effects between unit cells and the different interactions among conventional and glide-symmetric unit cells.

Multimode Analysis

When irreducible structures are of interest, a multimodal equivalent circuit can always be used to correctly model the interactions among the different scatterers [29], [31]. In a 1D higher-symmetric line, the unit cell can then be modeled as a 2-N-port network, where N is the number of background modes retained on each Floquet boundary of the cell to accurately compute the interactions among scatterers. This network can be characterized by means of its transmission matrix $\boldsymbol{T}$, whose eigenvalues are related to the wavenumbers of the Bloch modes supported by the structure. If only two modes are relevant, we get

$$\boldsymbol{T}\cdot\begin{bmatrix} V^{(1)} \\ V^{(2)} \\ I^{(1)} \\ I^{(2)} \end{bmatrix} = e^{-jk_x p}\begin{bmatrix} V^{(1)} \\ V^{(2)} \\ I^{(1)} \\ I^{(2)} \end{bmatrix}, \tag{1}$$

where $V^{(1)}$ and $I^{(1)}$ are the voltage and currents associated with the first mode on one Floquet boundary of the cell, $V^{(2)}$ and $I^{(2)}$ are the voltage and currents associated with the second mode on the same Floquet boundary, and k_x is the (possibly complex) unknown Bloch wavenumber.

In terms of the transmission matrix, this description can also lead to an alternative approach for performing a dispersion equation by means of a subcell's multimodal transmission matrix. In this case, we need to take into account that, after translating one subcell, each background mode composing the Bloch mode is not equivalent to a phase shift (as a translation of one cell is). To get a phase shift, we also need to perform a reflection [29] or a rotation [31] according to the glide or twisted nature of the structure. We can compensate for each background mode in this geometrical operation by multiplying each mode by a factor depending on the mode parity. In the case of a glide line, if the first mode in (1) is even with respect to the glide plane and the second mode is odd, we get

$$\boldsymbol{T}_{1/2}\cdot\begin{bmatrix} V^{(1)} \\ V^{(2)} \\ I^{(1)} \\ I^{(2)} \end{bmatrix} = e^{-jk_x p/2}\begin{bmatrix} V^{(1)} \\ -V^{(2)} \\ I^{(1)} \\ -I^{(2)} \end{bmatrix}, \tag{2}$$

where the transmission matrix $\boldsymbol{T}_{1/2}$ refers to only one-half of the unit cell (thus enabling a faster computation). Equation (2) also confirms that the presence of only one mode (or the presence of modes with the same parity) in both (1) and (2) makes the structure equivalent to a nonglide periodic line, having as a unit cell the subcell of the glide line. All these results can be easily generalized to 2D glide structures [29], where background modes can be defined on each of the four Floquet boundaries of the unit cell.

A periodic unit cell possesses higher symmetries when it is invariant under a geometrical transformation that, iterated several times, gives the unit-cell translation.

Mode Matching to Analyze Glide-Symmetric Structures

An appropriate way of analyzing electromagnetic structures that have higher symmetries is to apply the mode-matching analysis approach. Mode matching is based on representing the electric and magnetic fields in each section of the structure as a sum of suitable modes with unknown complex amplitudes. In other words, it uses preknowledge about the electromagnetic field configuration and symmetry properties to reduce the number of unknowns. With this technique, it is possible to precisely describe the electromagnetic fields in the structure and gain physical insight into the properties of higher symmetries.

As an example, let us consider a PPW with glide-symmetric holey walls [Figure 2(a) and (c)]. The electromagnetic fields in the PPW region (parallel to the walls) can be expressed as a series of Floquet harmonics by virtue of periodicity,

$$\begin{aligned} \mathbf{E}_t^{\text{Gap}} &= \frac{1}{p^2}\sum_{s,q} e^{-j(k_{x,s}x + k_{y,q}y)}\tilde{\mathbf{e}}_{t,sq}^{\text{Gap}}(z), \\ \mathbf{H}_t^{\text{Gap}} &= \frac{1}{p^2}\sum_{s,q} e^{-j(k_{x,s}x + k_{y,q}y)}\tilde{\mathbf{h}}_{t,sq}^{\text{Gap}}(z), \end{aligned} \tag{3}$$

with $k_{x,s} = k_{x,0} + 2\pi s/p$ and $k_{y,q} = k_{y,0} + 2\pi q/p$, and by assuming a rectangular lattice with period p in both the x and y directions. The amplitude of each Floquet harmonic of the transverse electric field can be written as

$$\tilde{\mathbf{e}}_{t,sq}^{\text{Gap}}(z) = \begin{pmatrix} A_{sq}^{x} \\ A_{sq}^{y} \end{pmatrix} \sin(k_{z,sq} z) + \begin{pmatrix} B_{sq}^{x} \\ B_{sq}^{y} \end{pmatrix} \cos(k_{z,sq} z),$$
$$\tilde{\mathbf{h}}_{t,sq}^{\text{Gap}}(z) = \begin{pmatrix} D_{sq}^{x} \\ D_{sq}^{y} \end{pmatrix} \sin(k_{z,sq} z) + \begin{pmatrix} F_{sq}^{x} \\ F_{sq}^{y} \end{pmatrix} \cos(k_{z,sq} z), \tag{4}$$

where $k_{z,sq} = (k_0^2 - k_{x,s}^2 - k_{y,q}^2)^{1/2}$ is the vertical wavenumber of the $(s,q)^{th}$ harmonic. This electromagnetic distribution is matched to the zero tangential electric field on the metallic parts of the PPW walls and to the tangential electromagnetic field distribution in the lateral waveguides

$$\mathbf{E}_t^{WG}\left(z = \frac{g}{2}\right) = \sum_m r_m^- C_m \boldsymbol{\Phi}_m(x, y),$$
$$\mathbf{H}_t^{WG}\left(z = \frac{g}{2}\right) = \sum_m r_m^+ Y_m C_m [\hat{z} \times \boldsymbol{\Phi}_m(x, y)], \tag{5}$$

where C_m is the unknown coefficient of the mth mode and $\boldsymbol{\Phi}_m$ and Y_m are the corresponding cross-section modal function and the wave admittance. In the formulation, both the E- and H-field components should be matched at the lateral waveguide openings, by which it is possible to determine the unknown coefficients. One should note that the selected waveguide modes are orthogonal in PPWs and in the lateral waveguide sections, but they are not mutually orthogonal. Therefore, the bi-Galerkin method is applied (i.e., waveguide modes of the PPW and the lateral waveguides are used to test the E- and H-field equations), and the mode-matching matrix is densely filled.

The generalized Bloch theorem [6], [26], [27] states that the field repeats itself (apart from an exponential factor) after a translation of half a period and a mirroring operation:

$$\mathbf{E}(x, y, -z) = \pm e^{-j\left(k_{x,0}\frac{p}{2} + k_{y,0}\frac{p}{2}\right)} \mathbf{E}\left(x - \frac{p}{2}, y - \frac{p}{2}, z\right). \tag{6}$$

If we assume that the field distribution in the lateral waveguides is described with only one waveguide mode, the linear system (whose determinant represents the characteristic equation of the mode traveling along the glide-symmetric periodic structure) is reduced to a single equation:

$$\sum_{\substack{s+q \\ \text{even}}} \tilde{\boldsymbol{\Phi}}(k_{x,s}, k_{y,q}) \tilde{\boldsymbol{\Phi}}(-k_{x,s}, -k_{y,q}) \frac{k_0^2 - k_{y,q}^2}{k_{z,sq}} \cot\left(\frac{k_{z,sq} g}{2}\right)$$
$$- \sum_{\substack{s+q \\ \text{odd}}} \tilde{\boldsymbol{\Phi}}(k_{x,s}, k_{y,q}) \tilde{\boldsymbol{\Phi}}(-k_{x,s}, -k_{y,q}) \frac{k_0^2 - k_{y,q}^2}{k_{z,sq}} \tan\left(\frac{k_{z,sq} g}{2}\right)$$
$$+ jp^2 \frac{r^+}{r^-} k_{z,01}^{WG} = 0. \tag{7}$$

The presence of glide symmetry means that, for even Floquet mode indices (i.e., for an $s+q$ even number), the electric field in the parallel-plate region is described with $\cos(k_{z,sq} z)$ terms (i.e., with terms that have an even symmetry across the $z = 0$ plane), while, for odd Floquet mode indices, the electric field is described with $\sin(k_{z,sq} z)$ terms [i.e., with terms that have an odd symmetry; see (4)]. It is interesting to compare this characteristic equation with the one given for an open holey surface. In the case of an open surface, there is no mixing of odd and even modes since there is no second holey surface forming the PPW (i.e., only the outgoing waves are present), so it is usually enough to consider only one waveguide mode. The situation is different when a top ground plane approaches the structure [34], [35] and when the structure possesses glide symmetry [26], [27].

Dielectric Glide-Symmetric Structures

Until recently, most of the realized prototypes possessing higher symmetry were made from metal. However, in many applications and especially when going higher in frequency toward optics, dielectrics are the preferred building material. Although, at first glance, there are a lot of similarities between the analysis of metallic and dielectric glide-symmetric structures, the main difference comes from the fact that in the dielectric case part of the propagating wave (and thus part of the electromagnetic power) travels outside the dielectric waveguide. The wave propagating in the corrugated region can be modeled as a wave propagating along a periodic array of dielectric slabs, and it has to be matched at both interfaces with the modes present in the PPW and in free-space, respectively [36]. For propagation constants smaller than the free-space one, a fast wave is excited, which leads to the leakage of electromagnetic energy (i.e., the considered structure actually represents a leaky-wave antenna).

Glide Symmetry to Create Stopbands and Electromagnetic Bandgaps

Some of the recently proposed structures with higher symmetries, and specifically those with glide symmetry, have been studied for their ability to produce stopbands and bandgaps. Periodic structures are often used in antenna designs to eliminate surface waves, reduce the mutual coupling between antennas, and produce microwave filters. On the other hand, a new technology known as the *gap waveguide* was recently proposed for high-frequency microwave circuits and antennas [13]. This technology requires stopbands for parallel-plate modes instead of surface waves (i.e., the periodic structure is embedded in a parallel-plate structure). One of the most popular types of gap waveguides is the groove gap waveguide. This technology is equivalent to a conventional rectangular waveguide in which the solid lateral walls are replaced by an electromagnetic bandgap (EBG) structure. Using this EBG structure, the waveguide is manufactured in two

pieces that are assembled afterward by simply screwing them together. Electrical contact between the two pieces is not strictly required.

Analysis of 2D Holey Glide-Symmetric EBGs

One possible solution to creating stopbands between parallel plates is to use periodic holes, as proposed in [37]. However, the stopband in all directions (i.e., the EBG) that is created by holey structures is typically narrow, as illustrated in Figure 4(a). Even after a thorough optimization of the constituent parameters of the holes, the stopband is quite different from one produced with pin-type structures [38]. In [39], it was demonstrated that holey structures with glide symmetry have a larger EBG bandwidth than conventional periodic holey structures. Indeed, the replacement of the top metal lid for a periodic structure made of holes, as shown in Figure 4(a), modifies all modes propagating in the structure and creates a wide stopband between the second and third mode that can be used, for example, for gap waveguide technology [40]–[42].

A complete parametric study of glide-symmetric holey structures, in terms of stopband properties, was carried out in [38]. The authors demonstrated that the period of the structure plays a key role in glide-symmetric holey structures since it determines the frequency range of operation. This implies that such a periodic structure is electrically larger than one made of pins. Another relevant conclusion is that the depth of the holes affects the behavior of the structure up to a given value, which has interesting consequences for the manufacturing of the structure since the depth

Glide symmetry is a good candidate for producing low-dispersive materials that can be used for lens antennas.

of the holes does not need to be precisely controlled. This property can be explained by the fact that only evanescent modes penetrate the holes [34], [35]. These modes vanish after a given depth, making this structure practically insensitive to the flatness and height of a hole.

Holey Glide-Symmetric Structures for Gap Waveguide Technology

One popular application of EBGs is in a parallel-plate scenario for potential use in gap waveguide technology. A number of periodic structures—typically, pin types, corrugations, and mushroom types—have been proposed for gap waveguide technology [44]. Gap waveguides can also be implemented with glide-symmetric holes acting as an EBG [40]. The two main advantages of this implementation are simplified manufacturing and robustness. The presence of the glide-symmetric holey structure stops the leakage produced by the irregularities on the two surfaces, which, in practice, are not perfectly attached.

With this approach, as illustrated in Figure 4(b), it is possible to design waveguide components. For example, phase shifters were presented in [41] and [45]. Another example of a component made with this version of the technology is a TE_{10}-to-TE_{20} mode converter,

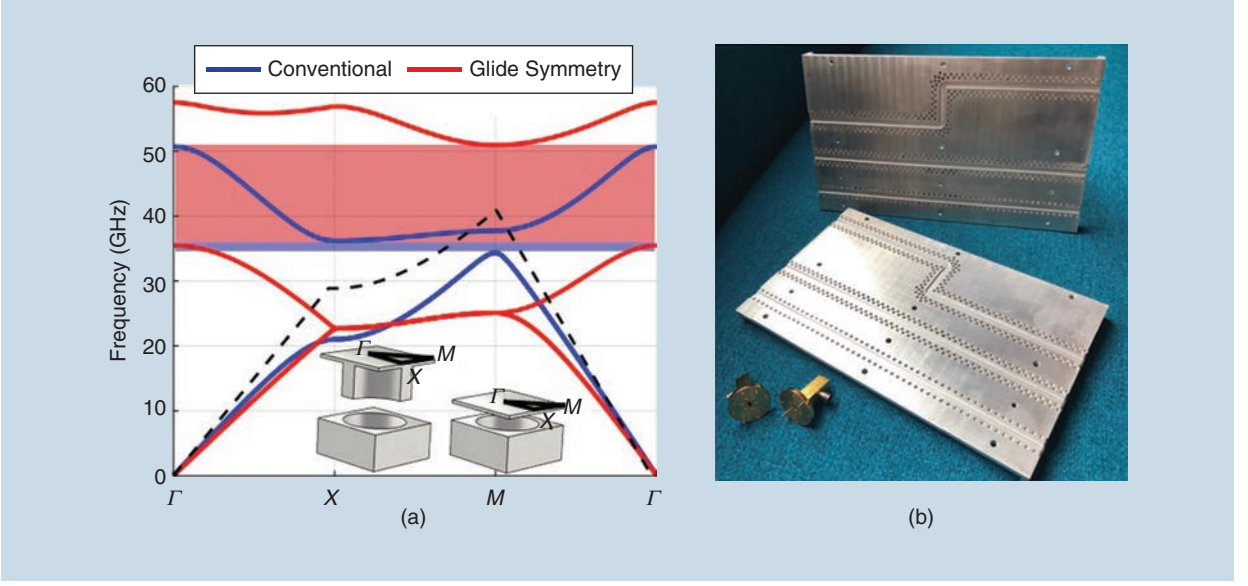

Figure 4. *(a) Dispersion diagrams comparing holey structures with and without glide symmetry. (b) A manufactured groove gap waveguide [40] and a flange [43] with glide-symmetric holes.*

which was used in [46] to produce a transversally compact slot array. Finally, a recent work [42] explored the possibilities of breaking the symmetry of the holes to add filtering capabilities to gap waveguide technology. When glide symmetry is broken, the bandgap is divided in two with a propagating mode in between. Therefore, in the frequency range of this mode, the waveguide has leakage that can be dissipated by introducing a thin, lossy material between the layers. Recent implementations of glide symmetry also make use of multilayer structures to reduce the manufacturing cost at high frequencies [47]. In [47], glide symmetry is imposed between adjacent layers. In other words, each layer is a half-unit cell displaced with respect to its top and bottom layers to increase the bandwidth of rejection.

Glide Symmetry for Flanges

Another interesting use of glide symmetry as an EBG was proposed in [43]. In this case, holey glide-symmetric holes were introduced in a waveguide flange to avoid leakage between connections. This technique can be used to produce fast measurements at very high frequencies since no physical contact between flanges is required. This idea was previously proposed with pins instead of holes in [15]. Here, again, the solution with holes is remarkably more robust and simpler to manufacture than the pin type. The concept was experimentally validated in the U band in [43]. The designed flanges in this article are presented in Figure 4(b).

Controllable Stopbands on Planar Technology

Although glide symmetry has become popular for its immediate application to gap waveguide technology, its opportunities extend beyond this specific domain. For example, glide symmetry has also been applied to transmission lines. In particular, it was proposed in coplanar waveguides to independently control the stopbands of even and odd modes [22]. Similarly, glide symmetry was employed in planar bifilar technology to control the stopbands generated by creating and breaking this symmetry [48]. In [49], elliptical holes between two dielectric layers were proposed to produce stopbands by breaking the glide symmetry. This work demonstrated that the width of these stopbands and their attenuation depend on the level of symmetry that is broken.

In [33], it was demonstrated that, using glide-symmetric mushrooms, the bandwidth of the first stopband in a microstrip technology can be increased without any additional manufacturing cost. This increase in the bandwidth is due to the different coupling that exists between conventional and glide-symmetric periodic unit cells. Therefore, only when the unit cells are electrically closed can glide symmetry be advantageous. Finally, in [50], glide-symmetric holes were used to directly produce fully metallic filters. These filters are proposed as a robust and low-cost alternative to conventional waffle-iron technology for high-frequency applications, such as at the Ka band and beyond.

Glide Symmetries to Reduce Dispersion

Another important feature of higher symmetries (and, in particular, glide symmetry) is that they can be used to reduce the dispersion of the first propagating mode in a periodic structure. This phenomenon has been used to create broadband lenses and low-dispersive transmission lines that find applications in leaky-wave antennas.

1D Glide-Symmetric Structures

The first studies of the dispersion of glide-symmetric structures were conducted for 1D periodic structures [6]. When the coupling between subunit cells is strong, the dispersion of the modes propagating in the new periodic structure is reduced. More recently, these results were corroborated for thin metallic corrugations [18], planar bifilar lines [48], and slotted lines [21], [22]. In all these studies, and for all these different technologies, when glide symmetry was applied, the first and second modes were connected, removing the first stopband [19]. The elimination of the first stopband inherently reduces the dispersion of the first mode, which means that the bandwidth is increased. This feature can be used, for example, to control the radiation of leaky-wave antennas [22], [51]–[54]. In one remarkable antenna proposed in [52], glide symmetry was used to compensate for the phase dispersion of a leaky-wave antenna, producing a low-cost broadband antenna for point-to-point communications at 60 GHz. Although most examples of glide symmetry employ two layers to implement the symmetry, a new type of flat glide symmetry was proposed in [49]. In that work, elliptical holes were introduced between two dielectric layers. These holes modify the propagation characteristics of the parallel-plate modes inside each layer, and glide symmetry reduces the dispersion.

2D Glide-Symmetric Structures

As with 1D periodic structures, 2D glide-symmetric structures are less dispersive than conventional ones. In [25], it was demonstrated that fully metallic glide-symmetric structures reduce the dispersion of the first propagating mode in PPWs. Additionally, the first mode is able to produce higher refractive indexes, and it is more isotropic. Although the first implementations of 2D glide-symmetric structures were based on holey structures [25], similar properties were also found for glide-symmetric pins [55], [56]. This technique was employed in [57] to produce a broadband Luneburg lens antenna in the Ka band for 5G communications. This antenna is shown in Figure 5(a), and its radiation patterns at

28 GHz are illustrated in Figure 5(b). It is broadband and highly efficient, and it has low scan losses.

Both pins and holes can be implemented to produce anisotropic responses. This anisotropy does not necessarily affect the broadband response of periodic structures. Glide-symmetric anisotropic unit cells were used to compress the size of a conventional Luneburg lens with transformation optics [58], which is an asset in practical applications since lens antennas can be reduced in size. In [58], it was demonstrated that glide symmetry was able to produce a higher level of compression than conventional unit cells.

Another example of 2D glide symmetry can be found in [59]. The authors demonstrated that nearby layers of patches that possess glide symmetry are able to produce higher equivalent refractive indexes. Similarly, glide symmetry is a good candidate for producing low-dispersive materials that can be used for lens antennas [60], [61]. Other recent implementations of 2D glide-symmetric structures include multilayer glide-symmetric metasurfaces [62], [63], dielectric lenses [64], reconfigurable planar lenses in the optical regime [65], and broadband slow acoustic waves [66]. Finally, glide symmetry has been introduced to reduce the reflections at the contour of homogeneous lenses [67]. For example, in [67], it was established that glide-symmetric unit cells are able to produce effective magnetic materials to practically eliminate the reflections in a hyperbolic lens. This technique can be used to increase the total efficiency of lens antennas.

Twist-Symmetric Structures

Similar to glide symmetries, twist-symmetric structures have propagation properties that differ from common periodic structures [68]. They can also be described with models that are analogous to glide symmetry. In [6], it was demonstrated that an m-fold twist line leads to the suppression of the first $m-1$ stopband in the line's Brillouin diagram. As in glide-symmmetric structures, this effect can be used to reduce frequency dispersion. Following the generalized Floquet theorem, m-fold twist-symmetric structures can be characterized by a subunit cell of length p/m. Therefore, they can be analyzed with equivalent-circuit models, as in the "Circuit Models" section [24], and with a multimodal approach similar to the one described in the "Multimode Analysis" section [31].

The latter method requires the description of a subunit cell as a 2-N-port network, where N is the number of background modes retained at each Floquet boundary, which defines a subcell transmission matrix $\boldsymbol{T}_{1/m}$, as in (2). Unlike glide symmetry, in twist structures, the modes are classed according to their azimuthal variation on the circular cross section of the waveguide $[\cos(n\varphi)$ and $\sin(n\varphi)]$ for a nth azimuthal order. The modes are then rotated at an angle π/m by means of a rotation

Glide symmetry has also been proposed to produce tunable stopbands and increase the bandwidth of filters.

matrix during every translation of p/m. The eigenvalue problem in (1) can be formulated as [31]

$$\begin{bmatrix} \boldsymbol{Q} & \boldsymbol{0} \\ \boldsymbol{0} & \boldsymbol{Q} \end{bmatrix} \cdot \boldsymbol{T}_{1/m} \cdot \begin{bmatrix} \boldsymbol{V} \\ \boldsymbol{I} \end{bmatrix} = e^{-jk_z \frac{p}{m}} \begin{bmatrix} \boldsymbol{V} \\ \boldsymbol{I} \end{bmatrix}, \tag{8}$$

where the $\boldsymbol{Q}$ matrix rotates the background mode at the subunit cell ports. Here, again, the presence of higher-order modes leads to a different dispersive behavior with respect to a line without a twist operation, where the $\boldsymbol{Q}$ matrix would become an identity matrix in (8).

Twist Symmetries in Circular-Section Coaxial Cables

Twist symmetry has been used in coaxial lines to increase their density across a large bandwidth of operation

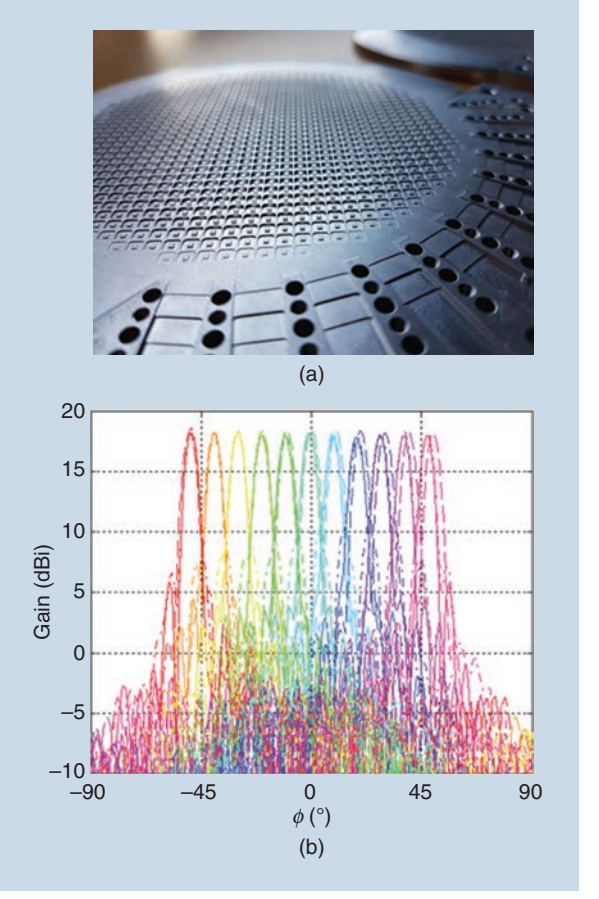

Figure 5. *A glide-symmetric Luneburg lens antenna [57]. (a) The manufactured prototype. (Scource: O. Zetterström; used with permission.) (b) Simulated and measured radiation patterns at 28 GHz. dBi: decibels isotropic.*

[17], [23]. Two alternatives have been studied: holey structures [23] and pins [17], [24]. Examples of the latter are given in Figure 6(a). As illustrated in Figure 6(b), the effective density of the medium depends on the order of the twist symmetry. Holes drilled in the inner conductor of the coaxial cable also lead to a similar effect, as demonstrated numerically and experimentally in [23]. In [23], to increase the effect of the holes in the line, an opening of π radians was chosen. In [24], π-radian rings were added to the outer conductor in a twist configuration, and an extension of the nondispersive frequency range was clearly observed when the twist order increased. As in glide structures, the physical parameters of the scatterers along the line can be changed, thus obtaining a graded-index line, where different frequencies can be rejected at varying positions of the transmission line [23].

In circular coaxial cables, another kind of symmetry analogous to the glide operator was introduced: polar glide symmetry. This symmetry is created by translating the obstacle in one conductor by one half a period and mirroring it into the other conductor [17], [23], [24]. This operation is not strictly a glide symmetry, and it does not close the first stopband at the edge of the Brillouin zone. However, fine-tuning the structure can result in waveguides with circular cross sections, producing effects that are similar to glide symmetry in Cartesian coordinates. A polar glide with π-radian rings was employed in [23] to prove this effect. In [24], a polar glide was implemented with π-radian rings, which is equivalent to a stepped discontinuity in the conductor radius. In its polar glide configuration, this stepped discontinuity alternates between the inner and outer conductor radii.

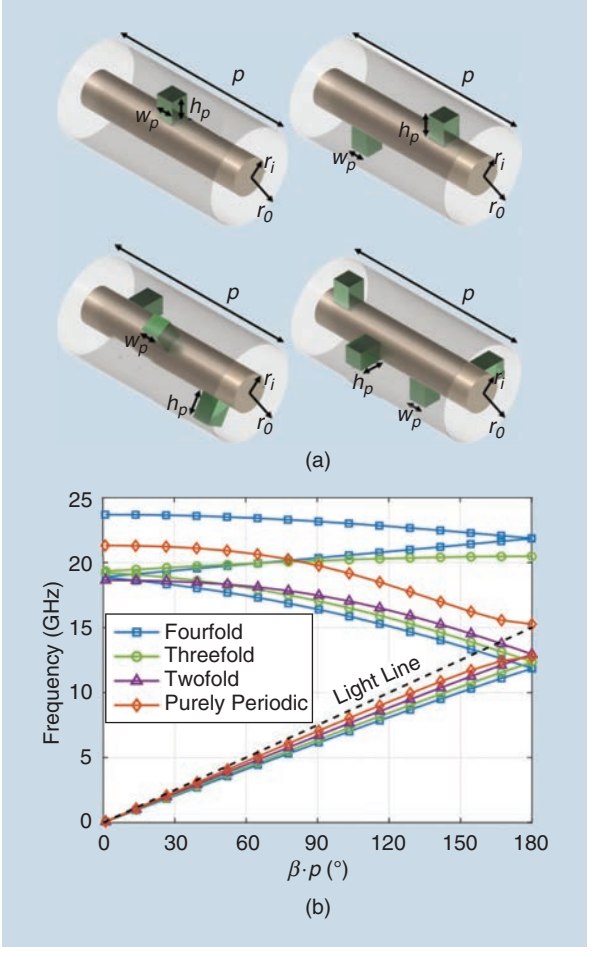

Figure 6. *(a) A coaxial cable loaded with a periodic array of pins with one-, two-, three-, and fourfold twist symmetry. (b) Dispersion diagrams of the coaxial cables [68].*

Another original way to combine twist and glide symmetries was proposed in [69], where a helicoidal radiating line (i.e., a helix antenna) is perturbed with periodic corrugations. A sequence of periodic corrugations naturally defines a twist symmetry due to the helicoidal shape of the line. Furthermore, a glide-symmetric sequence of corrugations can also be combined with the twist symmetry of the line. As a result, several geometric parameters can be used to tune the propagation features along the line, with a broadband response. In turn, in [69], it was proved that a helix antenna can be miniaturized without a significant deterioration of its performance.

Twist-Symmetric Waveguides and Metasurfaces

Twist symmetries have also been implemented in circular waveguides [70], as displayed in Figure 7. In [70], a holey waveguide was periodically loaded with metallic sheets having circular perforated holes that were not centered in the waveguide cross section. These obstacles block the first transverse electric mode of the waveguide and let only the transverse magnetic modes propagate. Furthermore, if these circular holes are rotated in a twist-symmetric feature, the stopbands between the first n modes are suppressed. Acting on geometrical parameters, a broader band of propagation is available as the period decreases, thus leading to a miniaturization of the line. Finally, if the holes have an elliptical shape, only a twist-symmetric rotation will open a passband, as illustrated in Figure 7.

Other applications of twist symmetry can be encountered in metasurface designs. For example, in [71], a multilayered configuration of metasurfaces based on split-ring resonators was proposed. The layered structure is locally twist-symmetric with respect to the stratification direction. The electric density encountered by a plane wave traveling across the metasurfaces depends on the twist order. These properties can be used to tailor a flat lens since different phase delays at each incidence point can be produced. In [71], these delays were designed to obtain a plane wave emerging from the lens. The design maintained

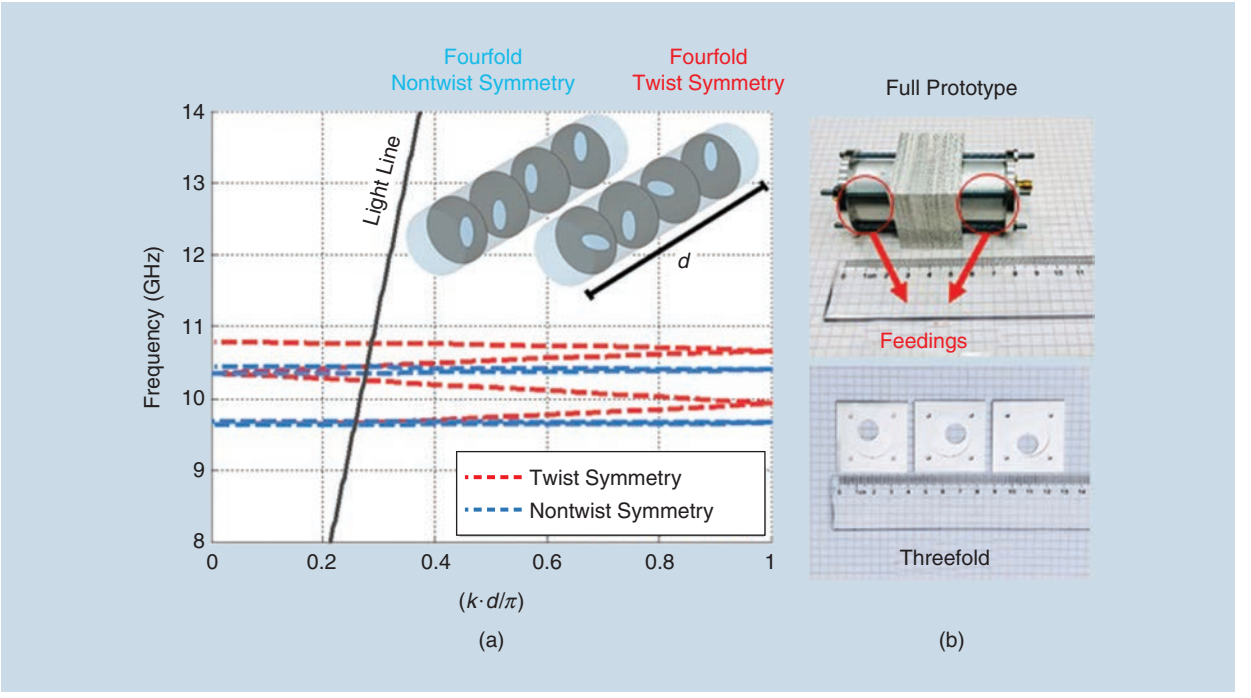

Figure 7. *A circular waveguide with twist-symmetric irises, as in [70]. (a) Dispersion diagrams for a fourfold twist-symmetric configuration with elliptical holes. (b) The prototype for circular holes.*

the orientation of the split rings on the first and last metasurfaces, so no depolarization is encountered. However, similar configurations can be used to convert the polarization [72], [73].

Conclusions

In this article, we described the latest discoveries related to higher symmetries and opportunities to incorporate them into electromagnetic device designs. There are two known types of spatial higher symmetries: glide and twist. Glide symmetry has been the most broadly studied since it can be implemented in planar structures, which are easy to manufacture. For example, glide symmetry has been proposed to reduce the dispersion properties of the first propagating mode in parallel-plate configurations. This creates possibilities for increasing the bandwidth of metasurface lens antennas. More recently, glide symmetry was proposed to reduce the cost of low-dispersive, leaky-wave antennas.

Additionally, glide symmetry has been reported to increase the operation bandwidth of conventional EBGs. This presents opportunities, for example, in cost-effective and robust gap waveguide technology and filters and to avoid undesireable leakage in flanges. Glide symmetry has also been proposed to produce tunable stopbands and increase the bandwidth of filters. In more recent works, glide symmetry has been found suitable for increasing the anisotropy of periodic structures, which can be used to reduce the dimensions of lens antennas. Finally, glide symmetry has been proposed for reducing the reflections at the contour of hyperbolic lenses; this can be used to increase the total efficiency of lens antennas. Twist symmetries have been less studied than glide symmetries due to the complexity of their practical implementation. However, like glide symmetries, they have been proposed to reduce the dispersion of propagating modes and to control stopbands in transmission lines, waveguides, and flat metasurfaces.

Acknowledgments

The authors would like to thank Oskar Zetterström for providing the photo in Figure 5(a). This work was partly funded by the Spanish Government, under grant TEC2016-79700-C2-2-R; the French Government, under National Research Agency (ANR) Modeling and Design of Holey Metasurfaces project grant ANR JCJC 2016, ANR-16-CE24-0030; the Vinnova project High-5 (grant 2018-01522), under the Strategic Program on Smart Electronic Systems; the Stiftelsen Åforsk project Higher-Symmetric Materials for 5G Communications (grant 18-302); and COST Action SyMat CA18223, supported by COST (European Cooperation in Science and Technology), www.cost.eu.

References

[1] A. Okabe, B. Boots, K. Sugihara, and S. N. Chiu, *Spatial Tessellations: Concepts and Applications of Voronoi Diagrams, 2nd edition*. Hoboken, NJ: Wiley, 2000.

[2] G. L. Trigg, "Higher symmetries," *Phys. Rev. Lett.*, vol. 14, no. 13, p. 479, Mar. 1965. doi: 10.1103/PhysRevLett.14.479.
[3] P. J. Crepeau and P. R. McIsaac, "Consequences of symmetry in periodic structures," *Proc. IEEE*, vol. 52, no. 1, pp. 33–43, Jan. 1964. doi: 10.1109/PROC.1964.2740.
[4] R. Mittra and S. Laxpati, "Propagation in a wave guide with glide reflection symmetry," *Can. J. Phys.*, vol. 43, no. 2, pp. 353–372, 1965. doi: 10.1139/p65-032.
[5] R. Kieburtz and J. Impagliazzo, "Multimode propagation on radiating traveling-wave structures with glide-symmetric excitation," *IEEE Trans. Antennas Propag.*, vol. 18, no. 1, pp. 3–7, Jan. 1970. doi: 10.1109/TAP.1970.1139607.
[6] A. Hessel, M. H. Chen, R. C. M. Li, and A. A. Oliner, "Propagation in periodically loaded waveguides with higher symmetries," *Proc. IEEE*, vol. 61, no. 2, pp. 183–195, Feb. 1973. doi: 10.1109/PROC.1973.9003.
[7] A. Sihvola, *Electromagnetic Emergence in Metamaterials*. Dordrecht: Springer-Verlag, 2002, pp. 3–17.
[8] N. Engheta and R.-W. Ziolkowski, *Metamaterials: Physics and Engineering Explorations*. Hoboken, NJ: Wiley, 2006.
[9] S. Maci, G. Minatti, M. Casaletti, and M. Bosiljevac, "Metasurfing: Addressing waves on impenetrable metasurfaces," *IEEE Antennas Wireless Propag. Lett.*, vol. 10, pp. 1499–1502, 2011. doi: 10.1109/LAWP.2012.2183631.
[10] C. Pfeiffer and A. Grbic, "Metamaterial Huygens' surfaces: Tailoring wave fronts with reflectionless sheets," *Phys. Rev. Lett.*, vol. 110, no. 19, p. 197,401, May 2013. doi: 10.1103/PhysRevLett.110.197401.
[11] *The Evolution of Electromagnetic Waveguides: From Hollow Metallic Guides to Microwave Integrated Circuits*. Hoboken, NJ: Wiley, 2006, ch. 16, pp. 543–566.
[12] Y. Wang, J. Li, L. Huang, Y. Jing, A. Georgakopoulos, and P. Demestichas, "5G mobile: Spectrum broadening to higher-frequency bands to support high data rates," *IEEE Veh. Technol. Mag.*, vol. 9, no. 3, pp. 39–46, Sept. 2014. doi: 10.1109/MVT.2014.2333694.
[13] P.-S. Kildal, E. Alfonso, A. Valero-Nogueira, and E. Rajo-Iglesias, "Local metamaterial-based waveguides in gaps between parallel metal plates," *IEEE Antennas Wireless Propag. Lett.*, vol. 8, pp. 84–87, 2009. doi: 10.1109/LAWP.2008.2011147.
[14] O. Quevedo-Teruel, M. Ebrahimpouri, and F. Ghasemifard, "Lens antennas for 5G communications systems," *IEEE Commun. Mag.*, vol. 56, no. 7, pp. 36–41, July 2018. doi: 10.1109/MCOM.2018.1700977.
[15] S. Rahiminejad, E. Pucci, V. Vassilev, P.-S. Kildal, S. Haasl, and P. Enoksson, "Polymer gap adapter for contactless, robust, and fast measurements at 220–325 GHz," *J. Microelectromech. Syst.*, vol. 25, no. 1, pp. 160–169, Feb. 2016. doi: 10.1109/JMEMS.2015.2500277.
[16] S. Amari, R. Vahldieck, and J. Bornemann, "Accurate analysis of periodic structures with an additional symmetry in the unit cell from classical matrix eigenvalues," *IEEE Trans. Microw. Theory Techn.*, vol. 46, no. 10, pp. 1513–1515, Oct. 1998. doi: 10.1109/22.721158.
[17] O. Dahlberg, R. C. Mitchell-Thomas, and O. Quevedo-Teruel, "Reducing the dispersion of periodic structures with twist and polar glide symmetries," *Sci. Rep.*, vol. 7, Aug. 2017, Art no. 10136. doi: 10.1038/s41598-017-10566-w.
[18] R. Quesada, D. Martín-Cano, F. J. García-Vidal, and J. Bravo-Abad, "Deep-subwavelength negative-index waveguiding enabled by coupled conformal surface plasmons," *Opt. Lett.*, vol. 39, no. 10, pp. 2990–2993, May 2014. doi: 10.1364/OL.39.002990.
[19] G. Valerio, Z. Sipus, A. Grbic, and O. Quevedo-Teruel, "Accurate equivalent-circuit descriptions of thin glide-symmetric corrugated metasurfaces," *IEEE Trans. Antennas Propag.*, vol. 65, no. 5, pp. 2695–2700, May 2017. doi: 10.1109/TAP.2017.2677923.
[20] F. Ghasemifard, M. Norgren, and O. Quevedo-Teruel, "Dispersion analysis of 2-D glide-symmetric corrugated metasurfaces using mode-matching technique," *IEEE Microw. Compon. Lett.*, vol. 28, no. 1, pp. 1–3, Jan. 2018. doi: 10.1109/LMWC.2017.2769881.
[21] M. Camacho, R. C. Mitchell-Thomas, A. P. Hibbins, J. R. Sambles, and O. Quevedo-Teruel, "Designer surface plasmon dispersion on a one-dimensional periodic slot metasurface with glide symmetry," *Optics Lett.*, vol. 42, no. 17, pp. 3375–3378, Sept. 2017. doi: 10.1364/OL.42.003375.
[22] M. Camacho, R. C. Mitchell-Thomas, A. P. Hibbins, J. R. Sambles, and O. Quevedo-Teruel, "Mimicking glide symmetry dispersion with coupled slot metasurfaces," *Appl. Phys. Lett.*, vol. 111, no. 12, p. 121,603, 2017. doi: 10.1063/1.5000222.
[23] F. Ghasemifard, M. Norgren, and O. Quevedo-Teruel, "Twist and polar glide symmetries: An additional degree of freedom to control the propagation characteristics of periodic structures," *Sci. Rep.*, vol. 8, no. 1, July 2018. Art no. 11266. doi: 10.1038/s41598-018-29565-6.
[24] Q. Chen, F. Ghasemifard, G. Valerio, and O. Quevedo-Teruel, "Modeling and dispersion analysis of coaxial lines with higher symmetries," *IEEE Trans. Microw. Theory Techn.*, vol. 66, no. 10, pp. 4338–4345, Oct. 2018. doi: 10.1109/TMTT.2018.2865456.
[25] O. Quevedo-Teruel, M. Ebrahimpouri, and M. N. M. Kehn, "Ultrawideband metasurface lenses based on off-shifted opposite layers," *IEEE Antennas Wireless Propag. Lett.*, vol. 15, pp. 484–487, Dec. 2016. doi: 10.1109/LAWP.2015.2492678.
[26] G. Valerio, F. Ghasemifard, Z. Sipus, and O. Quevedo-Teruel, "Glide-symmetric all-metal holey metasurfaces for low-dispersive artificial materials: Modeling and properties," *IEEE Trans. Microw. Theory Techn.*, vol. 66, no. 7, pp. 3210–3223, July 2018. doi: 10.1109/TMTT.2018.2829885.
[27] F. Ghasemifard, M. Norgren, O. Quevedo-Teruel, and G. Valerio, "Analyzing glide-symmetric holey metasurfaces using a generalized Floquet theorem," *IEEE Access*, vol. 6, pp. 71,743–71,750, Nov. 2018. doi: 10.1109/ACCESS.2018.2882056.
[28] S. Sensiper, "Electromagnetic wave propagation on helical structures (a review and survey of recent progress," *Proc. IRE*, vol. 43, no. 2, pp. 149–161, Feb. 1955. doi: 10.1109/JRPROC.1955.278072.
[29] M. Bagheriasl, O. Quevedo-Teruel, and G. Valerio, "Bloch analysis of artificial lines and surfaces exhibiting glide symmetry," *IEEE Trans. Microw. Theory Techn.*, vol. 67, no. 7, pp. 2618–2628, July 2019. doi: 10.1109/TMTT.2019.2916821.
[30] F. Mesa, R. Rodríguez-Berral, and F. Medina, "On the computation of the dispersion diagram of symmetric one-dimensionally periodic structures," *Symmetry*, vol. 10, no. 8, p. 307, 2018. doi: 10.3390/sym10080307.
[31] M. Bagheriasl and G. Valerio, "Bloch analysis of electromagnetic waves in twist-symmetric lines," *Symmetry*, vol. 11, no. 5, p. 620, 2019. doi: 10.3390/sym11050620.
[32] N. Marcuvitz, *Waveguide Handbook*. London, U.K.: P. Peregrinus on behalf of the Institution of Electrical Engineers, 1986.
[33] B. A. Mouris, A. Fernandez-Prieto, R. Thobaben, J. Martel, F. Mesa, and O. Quevedo-Teruel, "On the increment of the bandwidth of mushroom-type EBG structures with glide symmetry," *IEEE Trans. Microw. Theory Technol.*, vol. 68, no. 4, pp. 1365–1375, 2020. doi: 10.1109/TMTT.2020.2966700.
[34] F. J. García de Abajo and J. J. Sáenz, "Electromagnetic surface modes in structured perfect-conductor surfaces," *Phys. Rev. Lett.*, vol. 95, no. 23, p. 233,901, Nov. 2005. doi: 10.1103/PhysRevLett.95.233901.
[35] G. Valerio, Z. Sipus, A. Grbic, and O. Quevedo-Teruel, "Nonresonant modes in plasmonic holey metasurfaces for the design of artificial flat lenses," *Opt. Lett.*, vol. 42, no. 10, pp. 2026–2029, May 2017. doi: 10.1364/OL.42.002026.
[36] Z. Sipus and M. Bosiljevac, "Modelling of glide-symmetric dielectric structures," *Symmetry*, vol. 11, no. 6, p. 805, 2019. doi: 10.3390/sym11060805.
[37] D. Dawn, Y. Ohashi, and T. Shimura, "A novel electromagnetic bandgap metal plate for parallel plate mode suppression in shielded structures," *IEEE Microw. Compon. Lett.*, vol. 12, no. 5, pp. 166–168, May 2002. doi: 10.1109/7260.1000191.
[38] M. Ebrahimpouri, O. Quevedo-Teruel, and E. Rajo-Iglesias, "Design guidelines for gap waveguide technology based on glide-symmetric holey structures," *IEEE Microw. Compon. Lett.*, vol. 27, no. 6, pp. 542–544, June 2017. doi: 10.1109/LMWC.2017.2701308.
[39] M. Ebrahimpouri, E. Rajo-Iglesias, Z. Sipus, and O. Quevedo-Teruel, "Low-cost metasurface using glide symmetry for integrated waveguides," in *Proc. 10th European Conf. Antennas and Propagation (EuCAP)*, Apr. 2016, pp. 1–2. doi: 10.1109/EuCAP.2016.7481261.

[40] M. Ebrahimpouri, E. Rajo-Iglesias, Z. Sipus, and O. Quevedo-Teruel, "Cost-effective gap waveguide technology based on glide-symmetric holey EBG structures," *IEEE Trans. Microw. Theory Techn.*, vol. 66, no. 2, pp. 927–934, Feb 2018.

[41] E. Rajo-Iglesias, M. Ebrahimpouri, and O. Quevedo-Teruel, "Wideband phase shifter in groove gap waveguide technology implemented with glide-symmetric holey EBG," *IEEE Microw. Compon. Lett.*, vol. 28, no. 6, pp. 476–478, June 2018. doi: 10.1109/LMWC.2018.2832013.

[42] P. Padilla et al., "Broken glide-symmetric holey structures for bandgap selection in gap-waveguide technology," *IEEE Microw. Compon. Lett.*, vol. 29, no. 5, pp. 327–329, May 2019. doi: 10.1109/LMWC.2019.2906460.

[43] M. Ebrahimpouri, A. A. Brazalez, L. Manholm, and O. Quevedo-Teruel, "Using glide-symmetric holes to reduce leakage between waveguide flanges," *IEEE Microw. Compon. Lett.*, vol. 28, no. 6, pp. 473–475, June 2018. doi: 10.1109/LMWC.2018.2824563.

[44] E. Rajo-Iglesias and P.-S. Kildal, "Numerical studies of bandwidth of parallel-plate cut-off realised by a bed of nails, corrugations and mushroom-type electromagnetic bandgap for use in gap waveguides," *IET Microw. Antennas Propag.*, vol. 5, no. 3, pp. 282–289, Feb. 2011. doi: 10.1049/iet-map.2010.0073.

[45] A. Palomares-Caballero, A. Alex-Amor, P. Padilla, F. Luna, and J. Valenzuela-Valdes, "Compact and low-loss V-band waveguide phase shifter based on glide-symmetric pin configuration," *IEEE Access*, vol. 7, pp. 31,297–31,304, Mar. 2019. doi: 10.1109/ACCESS.2019.2903438.

[46] Q. Liao, E. Rajo-Iglesias, and O. Quevedo-Teruel, "Ka-band fully metallic TE_{40} slot array antenna with glide-symmetric gap waveguide technology," *IEEE Trans. Antennas Propag.*, vol. 67, no. 10, pp. 6410–6418, Oct. 2019. doi: 10.1109/TAP.2019.2922829.

[47] A. Vosoogh, H. Zirath, and Z. S. He, "Novel air-filled waveguide transmission line based on multilayer thin metal plates," *IEEE Trans. THz Sci. Technol.*, vol. 9, no. 3, pp. 282–290, May 2019. doi: 10.1109/TTHZ.2019.2905775.

[48] P. Padilla, L. F. Herrán, A. Tamayo-Domínguez, J. F. Valenzuela-Valdés, and O. Quevedo-Teruel, "Glide symmetry to prevent the lowest stopband of printed corrugated transmission lines," *IEEE Microw. Compon. Lett.*, vol. 28, no. 9, pp. 750–752, Sept. 2018. doi: 10.1109/LMWC.2018.2858228.

[49] A. Tamayo-Dominguez, J.-M. Fernandez-Gonzalez, and O. Quevedo-Teruel, "One-plane glide-symmetric holey structures for stop-band and refraction index reconfiguration," *Symmetry*, vol. 11, no. 4, p. 495, 2019. doi: 10.3390/sym11040495.

[50] A. Monje-Real, N. J. G. Fonseca, O. Zetterstrom, E. Pucci, and O. Quevedo-Teruel, "Holey glide-symmetric filters for 5G at millimeter-wave frequencies," *IEEE Microw. Compon. Lett.*, vol. 30, no. 1, pp. 31–34, Jan. 2020. doi: 10.1109/LMWC.2019.2953211.

[51] J. J. Wu, C. Wu, D. J. Hou, K. Liu, and T. Yang, "Propagation of low-frequency spoof surface plasmon polaritons in a bilateral cross-metal diaphragm channel waveguide in the absence of bandgap," *IEEE Photon. J.*, vol. 7, no. 1, pp. 1–8, Feb. 2015. doi: 10.1109/JPHOT.2015.2392382.

[52] Q. Chen, O. Zetterstrom, E. Pucci, A. Palomares-Caballero, P. Padilla, and O. Quevedo-Teruel, "Glide-symmetric holey leaky-wave antenna with low dispersion for 60-GHz point-to-point communications," *IEEE Trans. Antennas Propag.*, vol. 68, no. 3, pp. 1925–1936. doi: 10.1109/TAP.2019.2944535.

[53] J. Chen et al., "Wideband leaky-wave antennas loaded with gradient metasurface for fixed-beam radiations with customized tilting angles," *IEEE Trans. Antennas Propag.*, vol. 68, no. 1, pp. 161–170. doi: 10.1109/TAP.2019.2940542.

[54] G. Zhang, Q. Zhang, Y. Chen, and R. D. Murch, "High-scanning-rate and wide-angle leaky-wave antennas based on glide-symmetry Goubau line," *IEEE Trans. Antennas Propag.*, vol. 68, no. 4, pp. 2531–2540. doi: 10.1109/TAP.2019.2951524.

[55] N. Memeletzoglou, C. Sanchez-Cabello, F. Pizarro-Torres, and E. Rajo-Iglesias, "Analysis of periodic structures made of pins inside a parallel plate waveguide," *Symmetry*, vol. 11, no. 4, p. 582, 2019. doi: 10.3390/sym11040582.

[56] D. Sun et al., "Gap waveguide with interdigital-pin bed of nails for high-frequency applications," *IEEE Trans. Microw. Theory Techn.*, vol. 67, no. 7, pp. 2640–2648, July 2019. doi: 10.1109/TMTT.2019.2914907.

[57] O. Quevedo-Teruel, J. Miao, M. Mattsson, A. Algaba-Brazalez, M. Johansson, and L. Manholm, "Glide-symmetric fully metallic Luneburg lens for 5G communications at Ka-band," *IEEE Antennas Wireless Propag. Lett.*, vol. 17, no. 9, pp. 1588–1592, Sept. 2018. doi: 10.1109/LAWP.2018.2856371.

[58] M. Ebrahimpouri and O. Quevedo-Teruel, "Ultrawideband anisotropic glide-symmetric metasurfaces," *IEEE Antennas Wireless Propag. Lett.*, vol. 18, no. 8, pp. 1547–1551, Aug. 2019. doi: 10.1109/LAWP.2019.2922238.

[59] T. Chang et al., "Broadband giant-refractive-index material based on mesoscopic space-filling curves," *Nature Commun.*, vol. 7, Aug. 2016, Art no. 12661. doi: 10.1038/ncomms12661.

[60] D. Cavallo and C. Felita, "Analytical formulas for artificial dielectrics with nonaligned layers," *IEEE Trans. Antennas Propag.*, vol. 65, no. 10, pp. 5303–5311, Oct. 2017. doi: 10.1109/TAP.2017.2738064.

[61] D. Cavallo, "Dissipation losses in artificial dielectric layers," *IEEE Trans. Antennas Propag.*, vol. 66, no. 12, pp. 7460–7465, Dec. 2018. doi: 10.1109/TAP.2018.2869241.

[62] J. D. de Pineda, R. C. Mitchell-Thomas, A. P. Hibbins, and J. R. Sambles, "A broadband metasurface Luneburg lens for microwave surface waves," *Appl. Phys. Lett.*, vol. 111, no. 21, p. 211,603, Nov. 2017. doi: 10.1063/1.5003571.

[63] J. D. de Pineda, A. P. Hibbins, and J. R. Sambles, "Microwave edge modes on a metasurface with glide symmetry," *Phys. Rev. B*, vol. 98, no. 20, p. 205,426, Nov. 2018. doi: 10.1103/PhysRevB.98.205426.

[64] D. Jia, Y. He, N. Ding, J. Zhou, B. Du, and W. Zhang, "Beam-steering flat lens antenna based on multilayer gradient index metamaterials," *IEEE Antennas Wireless Propag. Lett.*, vol. 17, no. 8, pp. 1510–1514, Aug. 2018. doi: 10.1109/LAWP.2018.2851442.

[65] M. M. Shanei, D. Fathi, F. Ghasemifard, and O. Quevedo-Teruel, "All-silicon reconfigurable metasurfaces for multifunction and tunable performance at optical frequencies based on glide symmetry," *Sci. Rep.*, vol. 9, pp. 2045–2322, Sept. 2019. doi: 10.1038/s41598-019-49395-4.

[66] J. G. Beadle, I. R. Hooper, J. R. Sambles, and A. P. Hibbins, "Broadband, slow sound on a glide-symmetric meander-channel surface," *J. Acoust. Soc. Am.*, vol. 145, no. 5, pp. 3190–3194, 2019. doi: 10.1121/1.5109549.

[67] M. Ebrahimpouri, L. F. Herran, and O. Quevedo-Teruel, "Wide-angle impedance matching using glide-symmetric metasurfaces," *IEEE Microw. Compon. Lett.*, vol. 30, no. 1, pp. 8–11, Jan. 2020. doi: 10.1109/LMWC.2019.2955074.

[68] O. Dahlberg, F. Ghasemifard, G. Valerio, and O. Quevedo-Teruel, "Propagation characteristics of periodic structures possessing twist and polar glide symmetries," *EPJ Appl. Metamat.*, vol. 6, pp. 1–6, Mar. 2019. doi: 10.1051/epjam/2019012.

[69] A. Palomares-Caballero, P. Padilla, A. Alex-Amor, J. Valenzuela-Valdés, and O. Quevedo-Teruel, "Twist and glide symmetries for helix antenna design and miniaturization," *Symmetry*, vol. 11, no. 3, 2019. doi: 10.3390/sym11030349.

[70] O. Quevedo-Teruel, O. Dahlberg, and G. Valerio, "Propagation in waveguides with transversal twist-symmetric holey metallic plates," *IEEE Microw. Compon. Lett.*, vol. 28, no. 10, pp. 858–860, Oct. 2018. doi: 10.1109/LMWC.2018.2863718.

[71] O. Dahlberg, G. Valerio, and O. Quevedo-Teruel, "Fully metallic flat lens based on locally twist-symmetric array of complementary split-ring resonators," *Symmetry*, vol. 11, no. 4, p. 581, 2019. doi: 10.3390/sym11040581.

[72] Z. Wei, Y. Cao, Y. Fan, X. Yu, and H. Li, "Broadband polarization transformation via enhanced asymmetric transmission through arrays of twisted complementary split-ring resonators," *Appl. Phys. Lett.*, vol. 99, no. 22, p. 221,907, 2011. doi: 10.1063/1.3664774.

[73] A. N. Askarpour, Y. Zhao, and A. Alù, "Wave propagation in twisted metamaterials," *Phys. Rev. B*, vol. 90, no. 5, p. 054305, Aug. 2014. doi: 10.1103/PhysRevB.90.054305.

Wenjie Feng, Wenquan Che, Yongrong Shi, Quan Xue, Xiu Yin Zhang, and Xin Yu Zhou

Balanced to Unbalanced

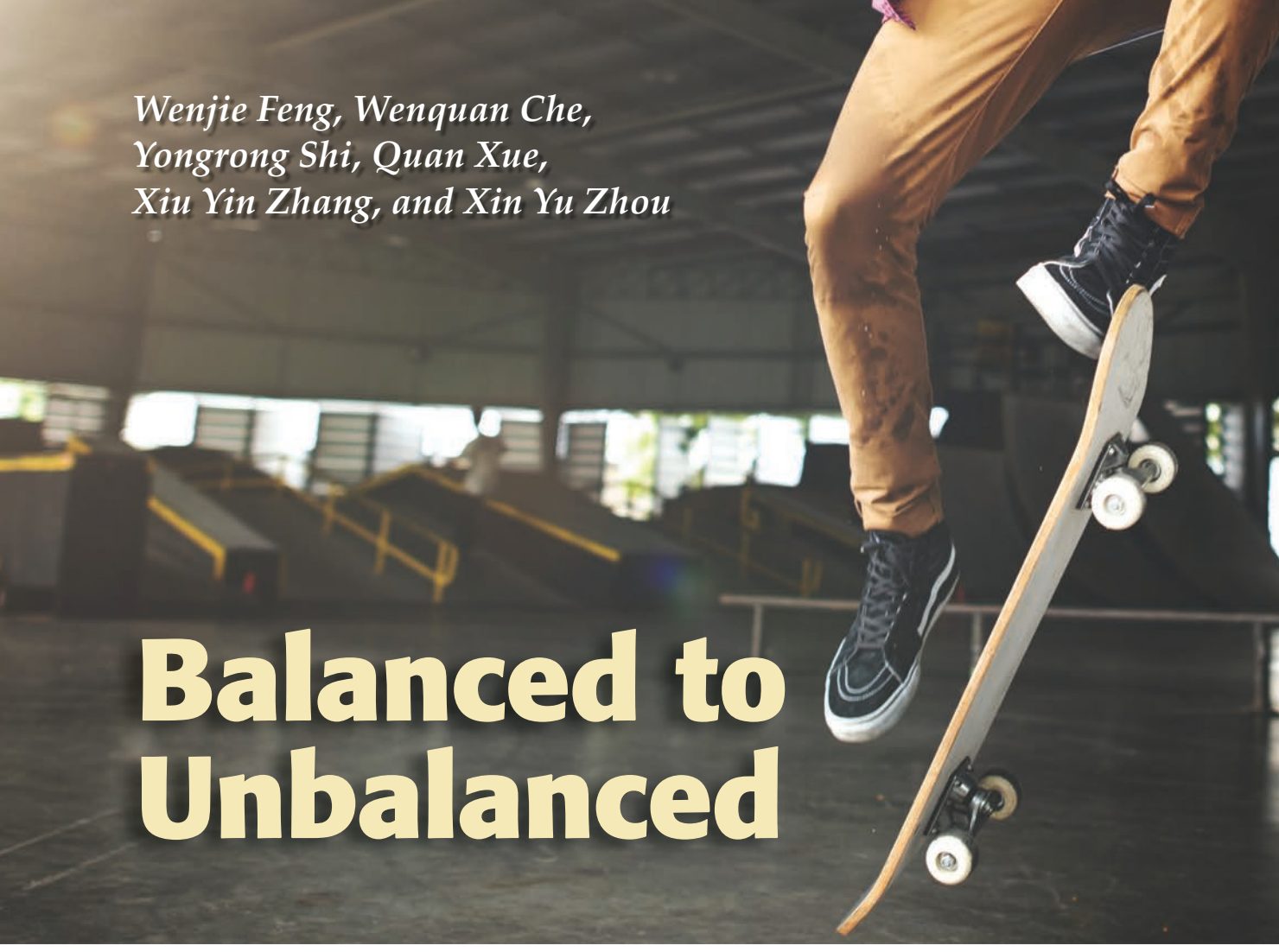

Fifth-generation (5G) communication techniques are growing in popularity, and 5G will become the commercial operation standard for mainland China in 2020 [1]. As the next-generation mobile communication network, 5G will not only greatly improve communication efficiency; it will also change the way people live and work. The 5G communication system contains the millimeter-wave and sub-6-GHz bands. For the sub-6-GHz band, circuits are becoming ever more compact and multifunction; thus, electromagnetic interference and multicoupling problems will greatly affect the entire system's performance [2]–[4]. In response, balanced circuits with higher immunity to environmental noises [5]–[8], lower electromagnetic interference [9]–[11], and better dynamic range [12]–[15] have attracted increasing attention in the past few years, and a large number of balanced circuits are being conceived [16], [17]. Currently, all feature differential-mode input and output terminals, so they cannot be connected directly to single-ended circuits. Balanced filters, antennas, and power dividers that can be cointegrated with balanced

Wenjie Feng (fengwenjie1985@163.com) and Wenquan Che (yeeren_che@163.com) are with the School of Electronic and Information Engineering, South China University of Technology, Guangzhou, China, and the Department of Communication Engineering, Nanjing University of Science and Technology, China. Yongrong Shi (yongrongshi@hotmail.com) is with the Department of Microwave Module Circuit, Nanjing Electronic Devices Institute, China. Quan Xue (eeqxue@scut.edu.cn) and Xiu Yin Zhang (zhangxiuyin@scut.edu.cn) are with the School of Electronic and Information Engineering, South China University of Technology, Guangzhou, China. Xin Yu Zhou (zhouxinyu24@hotmail.com) is with the Department of Electronic Engineering, City University of Hong Kong, China.

Digital Object Identifier 10.1109/MMM.2020.3014989

Date of current version: 6 October 2020

active circuits are required for the development of fully balanced transmitter and receiver RF chains, such as the balanced power dividers that can be connected to a Doherty power amplifier in a balanced system. In this case, balancing is only necessary at the input and output stages. It is expected that the transistor stage is still a single-ended structure, where only two amplifier devices are needed [18].

Power-distribution circuits, such as power dividers and directional couplers, are essential components [16]–[18] employed in antenna arrays, power amplifiers, phase shifters, and modems [18], all of which share several characteristic parameters, such as power-division bandwidth, power-division isolation, and compact size. In this article, we provide an overview of multifunctional wideband balanced-to-unbalanced four-/five-port filtering power dividers. Proposed planar multifunctional balanced-to-unbalanced filtering power dividers have attractive features such as wideband power-division bandwidth, wideband common-mode suppression, high power-division isolation, and multifunction integration.

Multifunctional Balanced-to-Unbalanced Four-Port Filtering Power Dividers

Balanced-to-Unbalanced Four-Port Filtering Power Dividers Using Coupled Lines

For microwave-balanced circuits, the differential-mode signal is used to transmit power [5]–[9], and the common- and cross-mode signals are suppressed [10]–[18]. Unlike conventional four-port balanced-to-balanced circuits [5]–[16], as shown in Figure 1(a), the proposed wideband balanced-to-unbalanced filtering power divider is a four-port reciprocal network with a pair of balanced ports, i.e., 1^+, 1^- (ports 1 and 3), and two single-ended ports, i.e., ports 2 and 4 [19]; S_{mm} refers to the mixed-mode scattering matrix, which can be obtained as in [19], [20]:

$$S_{mm} = \begin{bmatrix} S_{dd11} & S_{dc11} & S_{ds12} & S_{ds14} \\ S_{cd11} & S_{cc11} & S_{cs12} & S_{cs14} \\ S_{sd21} & S_{sc21} & S_{ss22} & S_{ss24} \\ S_{sd41} & S_{sc41} & S_{ss42} & S_{ss44} \end{bmatrix}, \tag{1}$$

and

$$\begin{cases} S_{dd11} = (S_{1+1+} - S_{1+1-} - S_{1-1+} + S_{1-1-})/2 \\ S_{cc11} = (S_{1+1+} + S_{1+1-} + S_{1-1+} + S_{1-1-})/2 \\ S_{cd11} = (S_{1+1+} - S_{1+1-} + S_{1-1+} - S_{1-1-})/2 \\ S_{dc11} = (S_{1+1+} + S_{1+1-} - S_{1-1+} - S_{1-1-})/2 \end{cases}'$$

$$\begin{cases} S_{sdn1} = (S_{n1+} - S_{n1-})/\sqrt{2} \\ S_{ds1n} = (S_{1+n} - S_{1-n})/\sqrt{2} \\ S_{scn1} = (S_{n1+} + S_{n1-})/\sqrt{2} \\ S_{cs1n} = (S_{1+n} + S_{1-n})/\sqrt{2} \end{cases}'$$

$$S_{ssnp} = S_{np}, \tag{2}$$

where $n, p = 2, 4$ and subscripts d, c, and s represent the differential mode, the common code, and the single-ended port, respectively. The filtering power divider should meet the requirements for port-impedance matching, differential-mode signal equal power division, wideband common-mode signal suppression, and power-division isolation.

In most balanced-to-unbalanced power dividers [20], [21], the differential-mode power-division bandwidths are less than 40%, and the common-mode suppression cannot meet the wideband frequency. To overcome these disadvantages, three new wideband balanced-to-unbalanced filtering power dividers are proposed in [19]; when the odd/even modes are excited from ports 1^+ and 1^-, a virtual short/open appears along the symmetric line, as shown in Figure 1(b) and (c). Figure 2(d)–(f) displays the measured and simulated frequency responses of the filtering power divider with coupled lines, and the prototype of the filtering power divider is shown in Figure 2(g).

For the differential mode, the measured 4-dB fractional bandwidth is 80.5% (1.17 to 2.78 GHz), the $|S_{dd11}|$ is greater than 13 dB, and the minimum in-band $|S_{sd21}|$ is 3.4 dB. For the common mode, the measured $|S_{sc21}|$ is better than 10 dB (the greatest 45-dB rejection at 2.03 GHz). The $|S_{dc11}|$ is greater than 30 dB. In addition, the measured power-division isolation $|S_{42}|$ is more than 15 dB (1.76 to 2.23 GHz), and the $|S_{22}|/|S_{44}|$ is greater than 15 dB from 1.72 to 2.29 GHz. In total, the proposed wideband balanced-to-unbalanced power divider with filtering function has been fully realized, while the passband selectivity for the differential-mode passband is not ideal. To overcome this shortcoming, two other novel high-selectivity wideband balanced-to-unbalanced filtering power dividers with adjustable transmission zeros are also realized in [19].

Balanced-to-Unbalanced Four-Port Filtering Power Dividers With Extended Upper Stopband

The balanced-to-unbalanced filtering power dividers in [19]–[21] achieve wideband power division and multifunctional performance. However, the broader-frequency common-mode suppression levels, differential-mode upper stopband, and differential-mode-to-common-mode conversion suppression can be improved. Several wideband balanced-to-unbalanced filtering power dividers with extended upper stopbands are proposed in [22]; one of these is shown in Figure 2(a). In this case, the stepped-impedance, coupled-line sections are used to replace the conventional coupled lines [23], and a one-wavelength-long closed-loop resonator with even- and odd-mode characteristic impedances Z_{ee1} and Z_{oo1} and an electrical length of

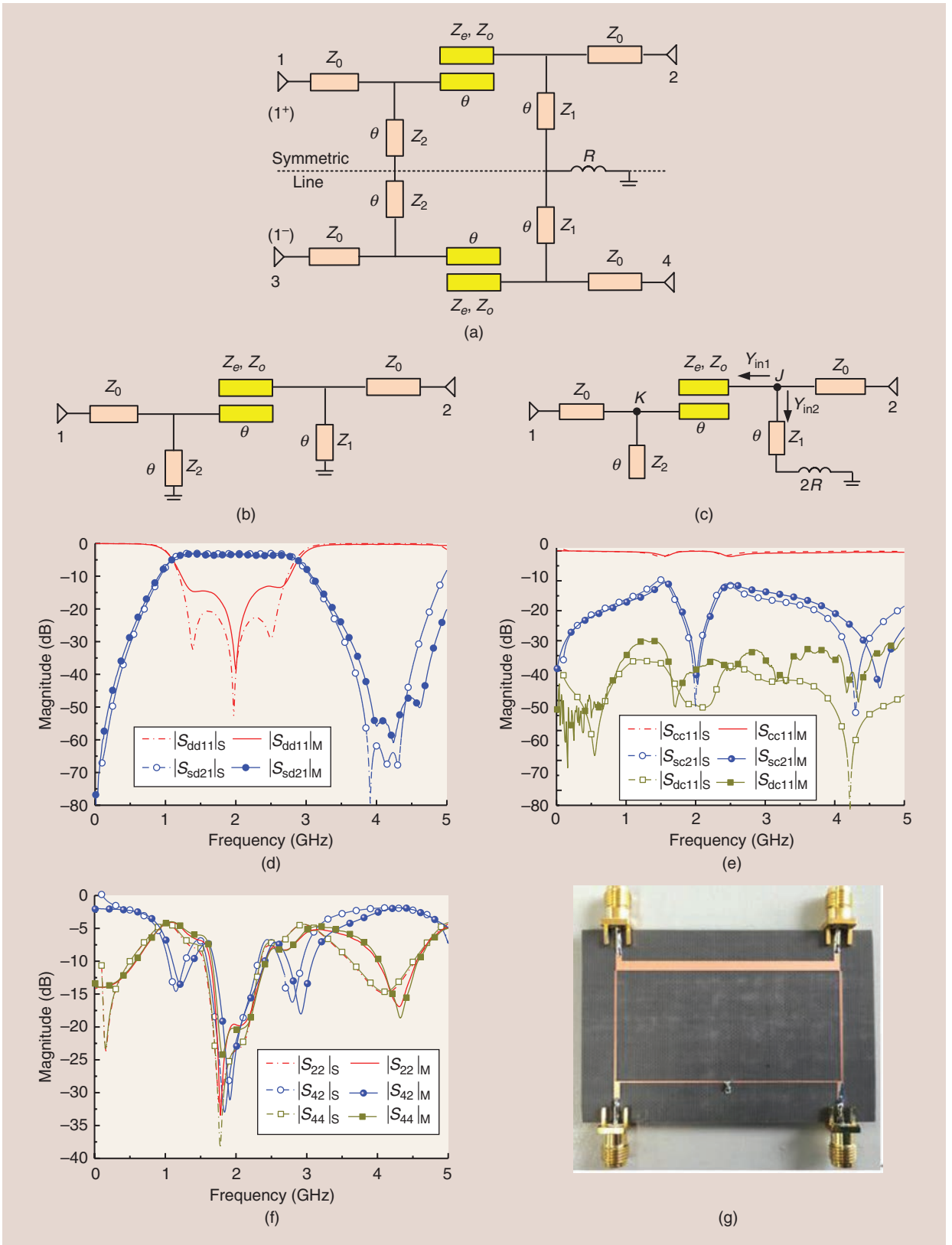

Figure 1. *A balanced-to-unbalanced filtering power divider with coupled lines [19]. (a) The schematic diagram, (b) a differential-mode circuit, (c) a common-mode circuit, (d) differential-mode frequency responses, (e) common-mode frequency responses, (f) the single-ended ports' responses, and (g) the prototype.*

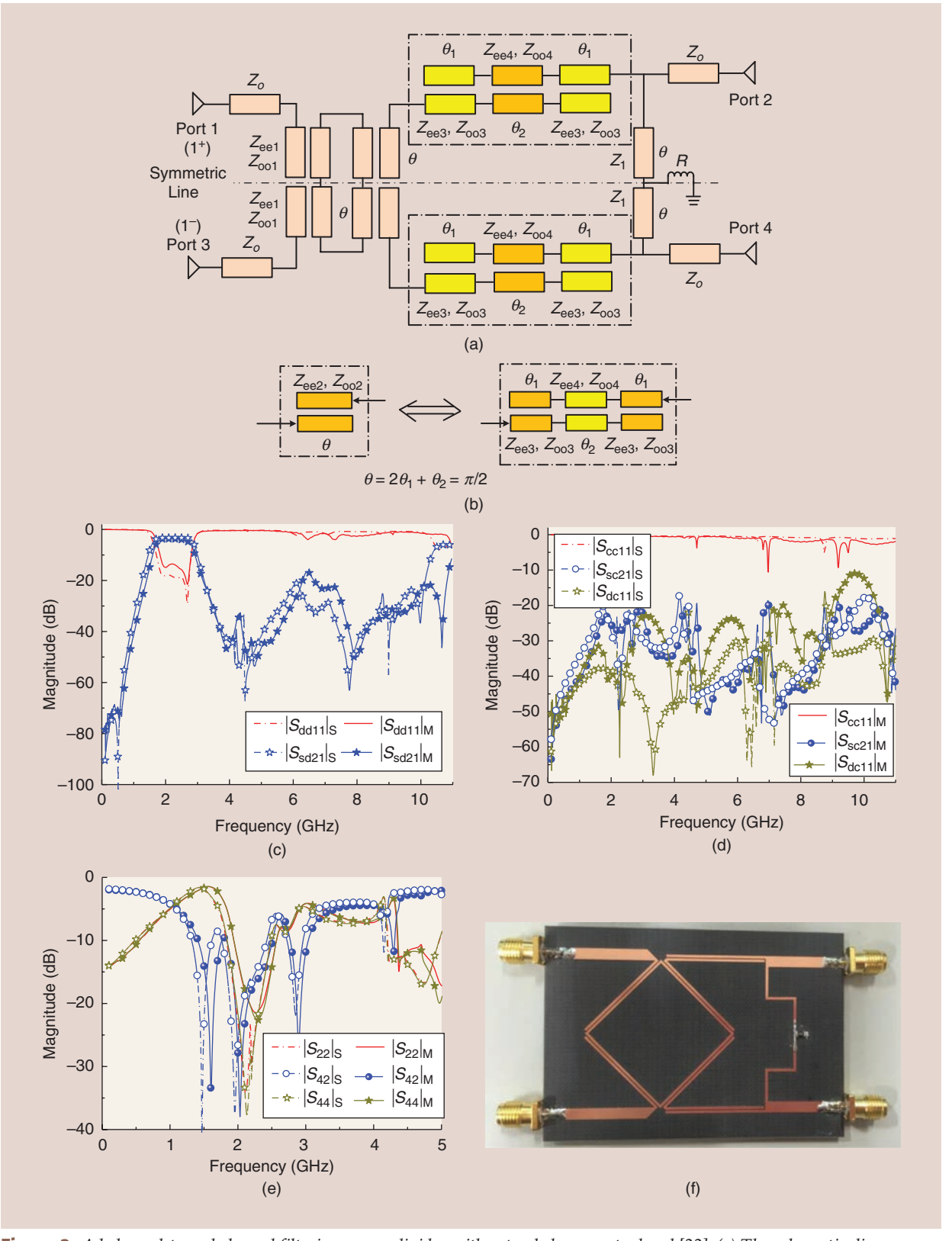

Figure 2. *A balanced-to-unbalanced filtering power divider with extended upper stopband [22]. (a) The schematic diagram, (b) conventional and stepped-impedance coupled-lines sections, (c) differential-mode frequency responses, (d) common-mode frequency responses, (e) the single-ended ports' responses, and (f) the prototype.*

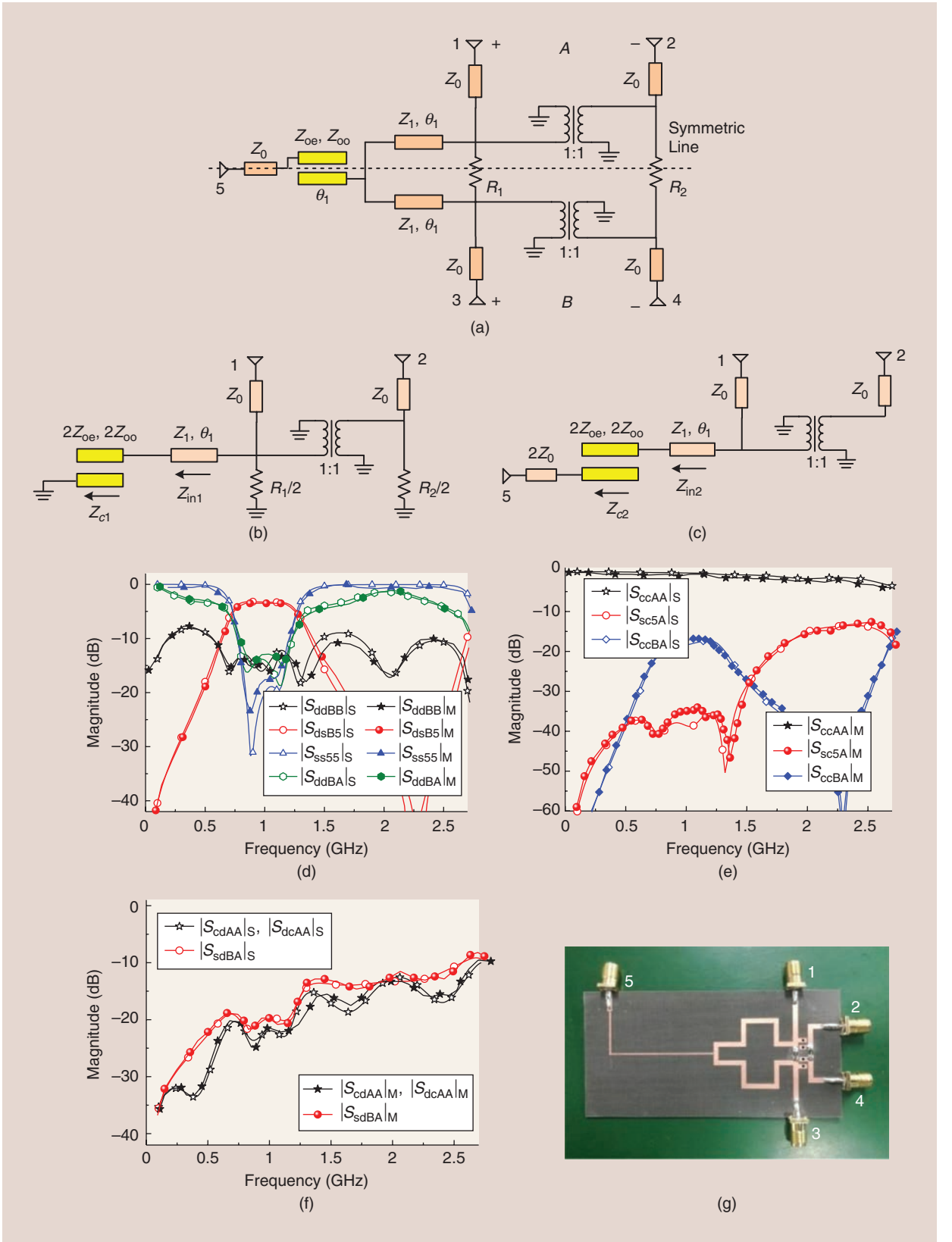

Figure 3. *A balanced-to-unbalanced filtering power divider using a 180° phase inverter [28]. (a) The schematic diagram, (b) a differential-mode circuit, (c) a common-mode circuit, (d) differential-mode frequency responses, (e) common-mode frequency responses, (f) the single-ended ports' responses, and (g) the prototype.*

θ is coupled to the input-port section of the circuit [a pair of balanced ports 1^+, 1^- (ports 1 and 3)] and two single-ended ports [2], [4], [24]. As displayed in Figure 2(b), for $\theta_1 = \theta_2 = \pi/6$, four transmission zeros are generated at the following spectral positions (they are expressed in terms of electrical lengths at these frequencies):

$$\begin{aligned}&\theta(f_{tz1}) = 0,\ \theta(f_{tz2})\\&= 3\cdot\arccos\sqrt{\frac{Z_{ee3}^2 Z_{oo4} - Z_{ee4} Z_{oo3}^2}{\frac{Z_{ee3}^2}{Z_{oo4}}(Z_{oo3}+Z_{oo4})^2 - \frac{Z_{oo3}^2}{Z_{ee4}}(Z_{ee3}+Z_{ee4})^2}},\\&\theta(f_{tz3}) = 3\pi - \theta(f_{tz2}), \theta(f_{tz4}) = 3\pi.\end{aligned} \tag{3}$$

The proposed wideband balanced-to-unbalanced filtering power dividers can be analyzed by the differential- and common-mode analysis procedure (as illustrated in [19]). Figure 3(c)–(f) presents the measured-frequency responses and a prototype of the wideband balanced-to-unbalanced filtering power divider with extended upper stopband. For the differential mode, the measured 3-dB power-division bandwidth ($|S_{sd21}|$<3.75 dB) extends from 1.72 to 2.8 GHz (i.e., 49.1% in relative terms). The differential-mode input-power-reflection ($|S_{dd11}|$) parameter is below –14 dB throughout the frequency range 1.8–2.9 GHz, whereas its 30-dB attenuation-referred stopband ($|S_{sd21}|$) extends from 3.1 to 10.6 GHz (i.e., up to 4.82 f_0). The common-mode suppression ($|S_{sc21}|$) and common-to-differential-mode dc reach 9.2 GHz (i.e., up to 4.7 f_0), while the minimum power-isolation ($|S_{42}|$) level between the single-ended output ports is above 30 dB [a center frequency (f_0) of 2.28 GHz].

Multifunctional Balanced-to-Unbalanced Five-Port Filtering Power Dividers

Microstrip Balanced-to-Unbalanced Five-Port Filtering Power Divider Using a 180° Phase Inverter

In addition to balanced-to-unbalanced four-port power dividers, single-ended-to-balanced five-port power dividers are also very important for connecting to balanced-driven antennas and balanced amplifiers. Some single-ended-to-balanced power dividers are proposed in [25]–[27]. However, they face some problems, such as narrow-band common-mode suppression, poor passband selectivity, and harmonic suppression; their multifunctional performance is hampered by the fact that they are not capable of bandpass filtering. A series of wideband five-port single-ended-to-balanced power dividers with wideband common-mode suppression is presented in [28]. As depicted in Figure 3(a), the proposed single-ended-to-balanced filtering power divider is a five-port component, which consists of a single-ended input (port 5) and two balanced outputs (ports A or 1 and 2 and B or 3 and 4). As with mixed-mode four-port balanced-to-unbalanced power dividers, the mixed-mode scattering matrix of the five-port power divider can also be obtained from the equation in [27] and [28]. For an example, see (4) at the bottom of the page.

The performance of the five-port power divider can be summarized as follows: when the differential-mode signals are excited in balanced port A (B) [27], [28], no differential-mode signals should be reflected (i.e., $S_{ddAA} = S_{ddBB} = 0$), no differential-mode signals can be transmitted to the other port B (A) (i.e., $S_{ddBA} = S_{ddAB}$

$$\begin{aligned}[S^{mm}] &= \begin{bmatrix} S_{ddAA} & S_{ddAB} & S_{dcAA} & S_{dcAB} & S_{dsA5}\\ S_{ddBA} & S_{ddBB} & S_{dcBA} & S_{dcBB} & S_{dsB5}\\ S_{cdAA} & S_{cdAB} & S_{ccAA} & S_{ccAB} & S_{csB5}\\ S_{cdBA} & S_{cdBB} & S_{ccBA} & S_{ccBB} & S_{csB5}\\ S_{sd5A} & S_{sd5B} & S_{sc5A} & S_{sc5B} & S_{ss55}\end{bmatrix}\\ &= \begin{bmatrix} \frac{S_{11}-S_{21}-S_{12}+S_{22}}{2} & \frac{S_{13}-S_{23}-S_{14}+S_{24}}{2} & \frac{S_{11}-S_{21}+S_{12}-S_{22}}{2} & \frac{S_{13}-S_{23}+S_{14}-S_{24}}{2} & \frac{S_{15}-S_{25}}{\sqrt{2}}\\ \frac{S_{31}-S_{41}-S_{32}+S_{42}}{2} & \frac{S_{33}-S_{43}-S_{34}+S_{44}}{2} & \frac{S_{31}-S_{41}+S_{32}-S_{42}}{2} & \frac{S_{33}-S_{43}+S_{34}-S_{44}}{2} & \frac{S_{35}-S_{45}}{\sqrt{2}}\\ \frac{S_{11}+S_{21}-S_{12}-S_{22}}{2} & \frac{S_{13}+S_{23}-S_{14}-S_{24}}{2} & \frac{S_{11}+S_{21}+S_{12}+S_{22}}{2} & \frac{S_{13}+S_{23}+S_{14}+S_{24}}{2} & \frac{S_{15}+S_{25}}{\sqrt{2}}\\ \frac{S_{31}+S_{41}-S_{32}-S_{42}}{2} & \frac{S_{33}+S_{43}-S_{34}-S_{44}}{2} & \frac{S_{31}+S_{41}+S_{32}+S_{42}}{2} & \frac{S_{33}+S_{43}+S_{34}+S_{44}}{2} & \frac{S_{35}+S_{45}}{\sqrt{2}}\\ \frac{S_{51}-S_{52}}{\sqrt{2}} & \frac{S_{53}-S_{54}}{\sqrt{2}} & \frac{S_{51}+S_{52}}{\sqrt{2}} & \frac{S_{53}+S_{54}}{\sqrt{2}} & S_{55}\end{bmatrix}.\end{aligned} \tag{4}$$

TABLE 1. Comparisons of several balanced filtering power dividers based on different techniques.

References	Port Number	0.6-dB Bandwidth (%, f_0)	Common-Mode Suppression	Wideband Common-Mode Suppression	Common-Mode and Differential-Mode Conversion	Filtering Property	Core Circuit Size ($\lambda_g \times \lambda_g$)
[21, Sec. 2]	4	5% 1.88 GHz	0.95–1.05 f_0 < –15 dB	No	< –15 dB 0.9–1.1 f_0	Yes	1.1 × 0.3
[25]	5	≈40% 10 GHz	0.9–1.1 f_0 < –15 dB	No	< –16 dB 0.9–1.1 f_0	No	0.5 × 0.25
[26]	5	≈30% 1 GHz	0.6–1.4 f_0 < –15 dB	No	< –15 dB 0.8–1.2 f_0	No	0.75 × 0.1
[27, Sec. 2]	4	36% 2 GHz	0.8–1.2 f_0 < –15 dB	No	< –15 dB 0.8–1.15 f_0	No	0.75 × 0.1
[19, Sec. 2]	4	60% 2 GHz	0.9–1.2 f_0 < –15 dB	Yes	< –15 dB 0.9–1.2 f_0	Yes	0.57 × 0.26
[22, Sec. 2]	4	49.1% 2.2 GHz	0–4.2 f_0 < –20 dB	Yes	< –20 dB 0–4 f_0	Yes	0.50 × 0.41
[28, Sec. 3]	5	42% 1.03 GHz	0–2.7 f_0 < –17 dB	Yes	< –15 dB 0–1.3 f_0	Yes	0.4 × 0.16
[28, Sec. 4]	5	45% 1.01 GHz	0–2.7 f_0 < –20 dB	Yes	< –15 dB 0–2 f_0	Yes	0.45 × 0.2

= 0), and the common-mode signals converted from the differential-mode signal are also not excited (i.e., $S_{cdAA} = S_{cdBB} = 0$) [27], [28]. After further calculation, the mixed-mode scattering matrix can be shown as [27], [28]

$$[S^{mm}] = \begin{bmatrix} 0 & 0 & 0 & 0 & \sqrt{2}S_{15} \\ 0 & 0 & 0 & 0 & \sqrt{2}S_{15} \\ 0 & 0 & -1 & 0 & 0 \\ 0 & 0 & 0 & -1 & 0 \\ \sqrt{2}S_{15} & \sqrt{2}S_{15} & 0 & 0 & 0 \end{bmatrix}. \quad (5)$$

Figure 3(d)–(f) depicts the measured and simulated frequency responses of the filtering power divider using an 180° phase inverter, and the prototype of the filtering power divider is shown in Figure 3(g). The measured 0.6-dB power-division bandwidth is roughly 42% (0.78–1.2 GHz), the upper stopband harmonic suppression is greater than 20 dB from 1.62 to 2.58 GHz (i.e., up to 2.58 f_0), the $|S_{ddAB}|$ is less than –13 dB for 0.8–1.2 GHz, the common-mode suppression parameter $|S_{ccBA}|$ is at least –17 dB from dc to 2.7 GHz, and the mode-conversion parameter for the common and differential modes is below –15 dB from dc to 1.3 GHz. Moreover, the use of a half-wavelength open-ended stub permits the synthesis of a high-selectivity filtering power divider with two transmission zeros located at 0.5 and 1.5 GHz, respectively [28].

Conclusions and Future Development

This article introduced wideband balanced-to-unbalanced four- and five-port filtering power dividers. Some comparisons with other approaches to balanced power dividers are listed in Table 1. In contrast to balanced power dividers developed using different techniques, the proposed balanced-to-unbalanced filtering power dividers all have multifunctional performance [19], [22], wideband common-mode suppression, and high passband selectivity for the differential mode [28]. The largest common-mode suppression can be extended up to over four octaves [22], and the integrated filtering function can further reduce the power divider's circuit size and transmission loss [28].

It should be pointed out that all of these multifunctional filtering power dividers are single-layer structures [21]–[28]; they can easily extend to applications of on-chip circuits and systems such as CMOS technology and gallium-arsenide technology [29]–[34], and it can be anticipated that increasing numbers of balanced integrated circuits will appear for 5G systems in the near future.

Acknowledgments

This work was supported by the National Key R&D Program of China (2018YFB1802000), the National Natural Science Foundation of China (61822110 and 61971387), the Guangdong Important Fields Research Program (2018B010115001), the Guangdong Innovative and Entrepreneurial Research Team Program (2017ZT07X032), the "Qing Lan Project" of the Jiangsu Province (2017–2020), and the Open Funding of State Key Laboratory of Millimeter Waves (K201804).

References

[1] B. Yang, Z. Yu, J. Lan, R. Zhang, J. Zhou, and W. Hong, "Digital beamforming-based massive MIMO transceiver for 5G millimeter-wave communications," *IEEE Trans. Microw. Theory Techn.*, vol. 66, no. 7, pp. 3403–3418, July 2018. doi: 10.1109/TMTT.2018.2829702.

[2] S. Rajendran, B. Bergh, and T. Vermeulen, "IEEE 5G spectrum sharing challenge: A practical evaluation of learning and feedback," *IEEE Commun. Mag.*, vol. 54, no. 11, pp. 210–216, Nov. 2016. doi: 10.1109/MCOM.2016.1600209RP.

[3] H. Tullberg et al., "The METIS 5G system concept: Meeting the 5G requirements," *IEEE Commun. Mag.*, vol. 54, no. 12, pp. 132–139, Dec. 2016. doi: 10.1109/MCOM.2016.1500799CM.

[4] T. S. Rappaport, Y. Xing, G. R. MacCartney, A. F. Molisch, E. Mellios, and J. Zhang, "Overview of millimeter wave communications for fifth-generation (5G) wireless networks: With a focus on propagation models," *IEEE Trans. Antennas Propag.*, vol. 65, no. 12, pp. 6213–6230, Dec. 2017. doi: 10.1109/TAP.2017.2734243.

[5] X. Gao, W. J. Feng, and W. Q. Che, "High selectivity wideband balanced filters using coupled lines with open/shorted stubs," *IEEE Microw. Wireless Compon. Lett.*, vol. 27, no. 3, pp. 260–262, Mar. 2017. doi: 10.1109/LMWC.2017.2661998.

[6] Y.-H. Pang, E. D. Lin, and Y.-Y. Chen, "A planar balanced crossover," *IEEE Trans. Microw. Theory Techn.*, vol. 64, no. 6, pp. 1812–1821, June 2016. doi: 10.1109/TMTT.2016.2551703.

[7] L.-S. Wu, Y.-X. Guo, and J.-F. Mao, "Balanced-to-balanced Gysel power divider with bandpass filtering response," *IEEE Trans. Microw. Theory Techn.*, vol. 61, no. 12, pp. 4052–4062, Dec. 2013. doi: 10.1109/TMTT.2013.2287684.

[8] W. J. Feng, W. Q. Che, and Q. Xue, "Balanced filters with wideband common mode suppression using dual-mode ring resonators," *IEEE Trans. Circuits Syst. I, Reg. Papers*, vol. 62, no. 6, pp. 1499–1507, June 2015. doi: 10.1109/TCSI.2015.2423752.

[9] Q. Xue, J. Shi, and J.-X. Chen, "Unbalanced-to-balanced and balanced to-unbalanced diplexer with high selectivity and common-mode suppression," *IEEE Trans. Microw. Theory Techn.*, vol. 59, no. 11, pp. 2848–2855, Nov. 2011. doi: 10.1109/TMTT.2011.2165960.

[10] W. Zhang, Y. L. Wu, Y. A. Liu, F. M. Ghannouchi, and A. Hasan, "A wideband balanced-to-unbalanced coupled-line power divider," *IEEE Microw. Wireless Compon. Lett.*, vol. 26, no. 6, pp. 410–412, June 2016. doi: 10.1109/LMWC.2016.2561400.

[11] Y. C. Chiou, J. T. Kuo, and H. R. Lee, "Design of compact symmetric four-port crossover junction," *IEEE Microw. Wireless Compon. Lett.*, vol. 19, no. 9, pp. 545–547, 2009. doi: 10.1109/LMWC.2009.2027054.

[12] R. Gómez-García, R. Loeches-Sánchez, D. Psychogiou, and D. Peroulis, "Multi-stub-loaded differential-mode multi-band bandpass planar filters," *IEEE Trans. Circuits Syst., II, Exp. Briefs*, vol. 65, no. 3, pp. 271–275, Mar. 2018. doi: 10.1109/TCSII.2017.2688336.

[13] W. J. Feng, X. Gao, W. Q. Che, W. C. Yang, and Q. Xue, "High selectivity wideband balanced filters with multiple transmission zeros," *IEEE Trans. Circuits Syst., II, Exp. Briefs*, vol. 64, no. 10, pp. 1182–1186, Oct. 2017. doi: 10.1109/TCSII.2015.2482398.

[14] W. J. Feng, C. Y. Zhao, W. Q. Che, and Q. Xue, "Wideband balanced network with high isolation using double-sided parallel-strip line," *IEEE Trans. Microw. Theory Techn.*, vol. 63, no. 12, pp. 4013–4018, Dec. 2015. doi: 10.1109/TMTT.2015.2495357.

[15] B. Zhang, Y. L. Wu, and Y. A. Liu, "Wideband single-ended and differential bandpass filters based on terminated coupled line structures," *IEEE Trans. Microw. Theory Techn.*, vol. 65, no. 3, pp. 761–774, Mar. 2017. doi: 10.1109/TMTT.2016.2628741.

[16] W. J. Feng, W. Q. Che, and Q. Xue, "The proper balance: Overview of microstrip wideband balanced circuits with wideband common mode suppression," *IEEE Microw. Mag.*, vol. 16, no. 5, pp. 55–68, June 2015. doi: 10.1109/MMM.2015.2408275.

[17] L. Jiao, Y. Wu, and W. Zhang, "Design methodology for six-port equal/unequal quadrature and rat-race couplers with balanced and unbalanced ports terminated by arbitrary resistances," *IEEE Trans. Microw. Theory Techn.*, vol. 66, no. 3, pp. 1249–1262, Mar. 2018. doi: 10.1109/TMTT.2017.2778108.

[18] W. R. Eisenstant, B. Stengel, and B. M. Thompson, *Microwave Differential Circuit Design using Mixed-Mode S-Parameters*, Boston: Artech House, 2006.

[19] X. Gao, W. J. Feng, W. Q. Che, and Q. Xue, "Wideband balanced-to-unbalanced filtering power dividers based on coupled lines," *IEEE Trans. Microw. Theory Techn.*, vol. 65, no. 1, pp. 86–95, Jan. 2017. doi: 10.1109/TMTT.2016.2614668.

[20] F. Huang, J. Wang, J. Hong, and W. Wu, "A new balanced-to-unbalanced filtering power divider with dual controllable passbands and enhanced in-band common-mode suppression," *IEEE Trans. Microw. Theory Techn.*, vol. 67, no. 2, pp. 695–703, Feb. 2019. doi: 10.1109/TMTT.2018.2883100.

[21] K. Xu, J. Shi, L. L. Lin, and J.-X. Chen, "A balanced-to-unbalanced microstrip power divider with filtering function," *IEEE Trans. Microw. Theory Techn.*, vol. 63, no. 8, pp. 2561–2569, Aug. 2015. doi: 10.1109/TMTT.2015.2445051.

[22] W. J. Feng, X. K. Ma, R. Gómez-García, Y. R. Shi, W. Q. Che, and Q. Xue, "Multi-functional balanced-to-unbalanced filtering power dividers with extended upper stopband," *IEEE Trans. Circuits Syst., II, Exp. Briefs*, vol. 66, no. 7, pp. 1154–1158, July 2019. doi: 10.1109/TCSII.2018.2877984.

[23] C. W. Tang, C. T. Tseng, S. H. Chiu, and P. H. Wu, "Design of wide passband/stopband microstrip bandpass filters with the stepped coupled line," *IEEE Trans. Microw. Theory Techn.*, vol. 61, no. 3, pp. 1095–1103, Mar. 2013. doi: 10.1109/TMTT.2013.2244227.

[24] W. J. Feng, W. Q. Che, Y. L. Ma, and Q. Xue, "Compact wideband differential bandpass filter using half-wavelength ring resonator," *IEEE Microw. Wireless Compon. Lett.*, vol. 23, no. 2, pp. 81–83, Feb. 2013. doi: 10.1109/LMWC.2013.2239632.

[25] Y. Yu and L. Sun, "A design of single-ended to differential-ended power divider for X band application," *Microw. Opt. Technol. Lett.*, vol. 57, no. 11, pp. 2669–2673, Nov. 2015. doi: 10.1002/mop.29404.

[26] W. W. Zhang et al., "Novel planar compact coupled-line single-ended-to-balanced power divider," *IEEE Trans. Microw. Theory Techn.*, vol. 65, no. 8, pp. 2953–2963, Aug. 2017. doi: 10.1109/TMTT.2017.2685389.

[27] Y. Wu, Z. Zhuang, L. Jiao, and Y. Liu, "A novel balanced-to-unbalanced complex impedance-transforming in-phase power divider," *IEEE Access*, vol. 5, pp. 16,205–16,213, Aug. 2017. doi: 10.1109/ACCESS.2017.2738013.

[28] W. J. Feng, Y. Zhao, W. Q. Che, R. Gómez-García, and Q. Xue, "Single-ended-to-balanced filtering power dividers with wideband common-mode suppression," *IEEE Trans. Microw. Theory Techn.*, vol. 66, no. 12, pp. 5531–5542, Dec. 2018. doi: 10.1109/TMTT.2018.2867195.

[29] E. Elsaidy, A. Barakat, A. B. Abdel-rahman, A. Allam, and R. K. Pokharel, "Ultracompact CMOS 60-GHz tapped-line combline BPF with two transmission zeros using defected ground structures," *IEEE Trans. Compon., Packag. Manuf. Technol.*, vol. 8, no. 9, pp. 1642–1649, 2018. doi: 10.1109/TCPMT.2018.2861411.

[30] K. X. Ma, N. N. Yan, K. S. Yeo, and W. M. Lim, "Miniaturized 40–60 GHz on-chip balun with capacitive loading compensation," *IEEE Electron Device Lett.*, vol. 35, no. 4, pp. 434–436, Apr. 2014. doi: 10.1109/LED.2014.2304612.

[31] Y. Zhong, Y. Yang, X. Zhu, E. Dutkiewicz, K. M. Shum, and Q. Xue, "An on-chip bandpass filter using a broadside-coupled meander line resonator with a defected-ground structure," *IEEE Electron Device Lett.*, vol. 38, no. 5, pp. 626–629, May 2017. doi: 10.1109/LED.2017.2690283.

[32] Z. J. Hou, S. Member, Y. Yang, S. Member, X. Zhu, and Y. C. Li, "A compact and low-loss bandpass filter using self-coupled folded-line resonator with capacitive feeding technique," *IEEE Electron Device Lett.*, vol. 39, no. 10, pp. 1584–1587, 2018. doi: 10.1109/LED.2018.2864597.

[33] Y. Yang, L. Hang, J. H. Zhang, X. Zhu, E. Dutkiewicz, and Q. Xue, "Compact on-chip bandpass filter with improved in-band flatness and stopband attenuation in 0.13- μm (Bi)-CMOS Technology," *IEEE Electron Device Lett.*, vol. 38, no. 10, pp. 1359–1362, Oct. 2017. doi: 10.1109/LED.2017.2739186.

[34] T. B. Kumar, K. X. Ma, and K. S. Yeo, "A 60-GHz coplanar waveguide-based bidirectional LNA in SiGe BiCMOS," *IEEE Microw. Wireless Compon. Lett.*, vol. 27, no. 8, pp. 742–744, Aug. 2017. doi: 10.1109/LMWC.2017.2723951.

Awards

IEEE Fellow Alexander I. Nosich Elected a Fellow of the Optical Society

During its September 2019 meeting in Washington, D.C., the board of directors of the Optical Society (OSA) elevated Prof. Alexander I. Nosich to OSA fellow (Figure 1), effective in 2020. His citation reads, "For the development of a method of analytical regularization to solve radiation, scattering, and eigenvalue problems in micro- and nano-optics." Prof. Nosich was elevated to IEEE Fellow in 2004.

Prof. Nosich is principal scientist with and head of the Laboratory of Micro and Nano-Optics, a major Ukrainian R&D center for millimeter and submillimeter waves that he founded in 2010 at the Institute of Radio Physics and Electronics, National Academy of Sciences of Ukraine. Prof. Nosich is a top-level theoretician in the field of computational electromagnetics and photonics. He is internationally recognized for having promoted a powerful and generic mathematical approach known as the *method of analytical regularization*, which converts the electromagnetic field problem to a Fredholm second-kind matrix equation that guarantees convergence.

©SHUTTERSTOCK.COM/VALDIS TORMS

In optics, his derivation of the radiation condition for open waveguides was a pioneering achievement, generalizing the Sommerfeld condition. He also introduced the lasing eigenvalue problem, a modified formulation of the source-free Maxwell problem adapted to study the on-threshold natural modes of lasers as open resonators with active regions. More recently, he studied ultrahigh-Q lattice modes, linking them to the origin of the well-known phased array blindness effect.

Prof. Nosich initiated the International Conference on Mathematical Methods in Electromagnetic Theory (which has been held since 1990), organized the IEEE East Ukraine Joint Chapter (1995), represented Ukraine in the European Microwave Association (2001–2003), and received the Doctor Honoris Causa of the University of Rennes-1, France (2015). It should be mentioned that Prof. Nosich works under conditions that are very unfavorable compared to more developed countries. Recognizing these circumstances, the International Commission for Optics awarded him the Galileo Galilei Medal in 2017.

Figure 1. *Prof. Alexander I. Nosich was elected an OSA fellow.*

Digital Object Identifier 10.1109/MMM.2020.3014992
Date of current version: 6 October 2020

IC-MAM 2021

IEEE MTT-S International Conference on **Microwave Acoustics & Mechanics**

July 19–21, 2021, Munich, Germany

Conference General Chair
Amelie Hagelauer
Universität Bayreuth
Bayreuth, Germany
chairs.icmam@mtt.org

Conference General Co-Chair
Andreas Tag
Qorvo
Apopka, FL, USA

Technical Program Chair
Holger Maune
Technische Universität Darmstadt
Darmstadt, Germany
tpc.icmam@mtt.org

Technical Program Co-Chair
Andreas Link
Qorvo
Munich, Germany

Songbin Gong
University of Illinois
Urbana, IL, USA

Conference Finance Chair
Stefan J. Rupitsch
Friedrich-Alexander-Universität
Erlangen-Nürnberg, Germany
finance.icmam@mtt.org

Venue
Rohde & Schwarz
Training Centre Munich

Sponsor
ROHDE&SCHWARZ
Make ideas real

Call for Papers

The International Conference on Microwave Acoustics & Mechanics (IC-MAM) represents a unique and unprecedented opportunity to bring together researchers and practitioners of different background (materials scientists, physicists, microwave engineers and process technologists), to share the most recent advances in new materials and manufacturing processes as well as components and devices, which represent the key for the development of future RF, microwave, mm-wave and THz devices, circuits and systems based on RF-MEMS and Acoustics. IC-MAM is organized by the IEEE Microwave Theory and Techniques Society (MTT-S) and features an exciting technical program and invited talks by worldwide recognized experts of RF-MEMS and BAW/SAW technologies.

Conference Topics

Perspective authors are cordially invited to submit papers in all areas of Microwave Acoustics and RF MEMS including but not limited to:

- Acoustic/MEMS Device Applications
- Acoustic/MEMS Device Design
- Acoustic/MEMS Device Modeling
- Materials & Propagation
- Advances in Filter and Multiplexer Technology
- SAW and BAW Sensor Devices and Applications
- Multi-Band RF Modules for Multi-Standard/-Mode Systems
- Fusion of Major Transmit and Receive Functionality in Single Modules
- Tunable & Reconfigurable Devices, like Bulk and Thin-film Components and Devices, e.g., based on Ferroelectrics, Phase-Change Materials

Submitted papers should be three to four pages in length. Authors must adhere to the format of the IEEE conference paper template.

Submission deadline:	April 12, 2021
Notification of acceptance:	May 11, 2021
Final paper submission:	May 31, 2021
Conference date:	July 19–21, 2021

Technical Sponsor
IEEE MTT-S

Technical Co-Sponsors
EuMA VDE

http://www.icmam-ieee.org

Digital Object Identifier 10.1109/MMM.2020.3020485

Educator's Corner

A Radio Engineer's Voyage to Double-Century-Old Plane Geometry

■ Takashi Ohira

Sail to the mysterious triangles and arcs of supreme elegance.

Academia may approach radio engineering through two possible educational ways. One is based on the analysis of formulas stemming from electromagnetics and circuit theory. Students are required to have mastered calculus and linear algebra beforehand. Although this way is mathematically rigorous, students sometimes become exhausted by the nabla-manifold vector and matrix equations. The other possible approach is based on plane geometry. The instructor draws an impedance locus on a blackboard to illustrate the behavior of circuit components, such as *LCR* and transmission lines. According to our academic experience, this friendly way is effective to stimulate first-year students to intuitively start from the introduction. The special geometry that can be exploited in radio engineering originated in the early 19th century, i.e., long before the Smith chart was invented. One may then ask, what in the world took place two centuries ago? To answer this question, we have in this article a time-traveling vessel. The final boarding gong is now beating, and we will soon hoist the sails for a mysterious adventure.

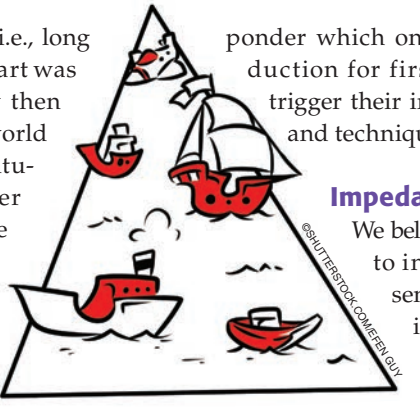

Maiden Voyage

Imagine that we make our maiden voyage across the ocean. Every mate on duty must be able to use an indispensable item: the navigation chart. This idea also applies to voyages in radio engineering. Through analogy to Mercator, Mollweide, and Lambert's conic projections in cartography, there are several different schemes we can use to draw a chart of electric impedance on a complex plane. Each scheme has pros and cons in accordance with the purpose of the chart, as comprehensively overviewed by Harold Wheeler in [1]. University lecturers may then ponder which one is the best introduction for first-year students to trigger their interest in RF theory and techniques.

Impedance Plane

We believe that the best way to introduce the representation of impedance is to use a Cartesian coordinate system, as presented in Figure 1. Complex impedance is decomposed into its real and imaginary parts as $Z = R + jX$. This is simply called the *impedance plane* or,

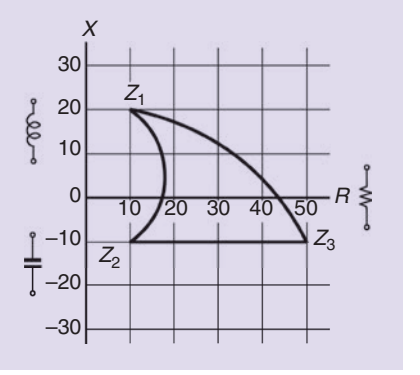

Figure 1. *The impedance half-plane with a mysterious triangle.*

Takashi Ohira (ohira@tut.jp) is with Toyohashi University of Technology, Aichi, Japan. He is a Life Fellow of IEEE.

Digital Object Identifier 10.1109/MMM.2020.3015136
Date of current version: 6 October 2020

to be more specific, the impedance *half-plane*, when the load is assumed to be passive, i.e., $R > 0$. The concept of such a half-plane was originally proposed by Henri Poincaré as a visible model of hyperbolic geometry [2], [3].

This concept is exploited for radio engineering by assuming that the vertical axis represents a reactance X, which physically implies inductors for positive X and capacitors for negative X. This R-X system utilizes a linear and orthogonal grid, which provides straight-line routes to represent the behavior of *LCR* elements connected in series to the load. Therefore, this simple approach is highly recommended for first-semester young sailors or possibly prospective captains, rather than trying to demonstrate other sophisticated circular charts abruptly. That is to say, simple is beautiful.

Figure 2. *A variety of VSWR indicators in our vessel's radio shack.*

Curious Enigma

One stimulating supplement to this plane is a mysterious triangle drawn on the R-X grid, as shown in Figure 1. This is, apparently, distorted in comparison to the usual triangle. However, in a sense, the three routes shown all represent the shortest links between two vertices. This may sound like a tricky riddle. In spite of this, it is mathematically true when a special metric or scale intended for the impedance half-plane is employed. To address this curious enigma in an analytical way, let us set out on our voyage by first examining the meanings of "distance" and "length" on a chart. These concepts will be clarified in the following sections.

Geometric Distance

Let us consider two points, Z_1 and Z_2, located anywhere on the half-plane. For example, look again at the triangle's west side in Figure 1. The question here is, how should we define the distance, hereafter denoted as D, between Z_1 and Z_2? In any geometry, the distance must be a single, scalar, and real function of the relative position of two points. More strictly, it must exhibit four properties: identity, nonnegativity, commutativity, and triangle inequality [2], [3].

Even taking all these requirements into account, the definition of *distance* is not unique; rather, it has alternative formulations. A quick idea could be $D = |Z_1 - Z_2|$, where the twin vertical bars mean complex modulus. Although this definition is mathematically simple, it does not work properly in radio engineering, as the impedance has a dimension of ohms. Another idea for the definition could be $D = |Z_1 - Z_2|/Z_o$, where the denominator, Z_o, denotes some reference impedance, such as 50 Ω. In this definition, the physical dimension is nullified by the normalization. However, universe-strong versatility is expected from the general definition of *distance*. What we are looking for is a dimension-free, purely relative quantity that is invariant to any reference impedance.

Among the possible candidates for a valid definition of *distance*, we single out the natural logarithm of voltage standing-wave ratio (VSWR) ρ, which is simply formulated as

$$D = \ln \rho. \tag{1}$$

This is because the logarithmic VSWR strikes a deep chord with radio engineers, as richly suggested by Madhu Gupta in [3]. The aforementioned D is called the *Poincaré distance* in hyperbolic geometry, and (1) indicates our selection as the starting postulate of this exciting voyage.

> *We employ log VSWR as our starting postulate.*

Reflectance Magnitude

To estimate the distance D between Z_1 and Z_2 using (1), we need to recall how ρ is derived from the two impedances. This can be formulated by the wave-reflectance approach as follows.

Radio engineers, from amateur to professional, often use ρ to tune a load, such as antennas or a wireless coupler for RF power transfer. Various measurement instruments are illustrated in Figure 2. They all indicate ρ to notify the radio operator of how much power is being reflected from the load. A basic and well-known relation is given by

$$\rho = \frac{1+\gamma}{1-\gamma}, \tag{2}$$

where γ denotes the reflectance magnitude. This equation tells us that the VSWR starts from unity at zero reflection, becomes three at half reflection, and goes to infinity at full reflection. Typical numerical examples of this behavior are given in Table 1.

Radio engineers, from amateur to professional, often use ρ to tune a load such as antennas or a wireless coupler for RF power transfer.

In addition to the numeric table, a more instructive route to the γ-to-ρ conversion is shown in Figure 3. Let us place a perpendicular pole at point (1, 0) up to height γ. We draw a straight line (elastic cord) from the pivot point (–1, 1) that passes through the pole's top. This cord is extended down to intercept the horizon at coordinate ρ, which gives us the exact VSWR. An inverse conversion is also available. Slide ρ from left to right along the horizon while keeping the pivot point fixed. The height γ at which the pole is truncated by the cord gives the reflectance magnitude.

This mechanical model enables us to estimate the VSWR even without any formula or electronic calculator. In fact, such a graphical approach cultivates engineering intuition in students' minds much more fully than just starting with the user's manual for fully automated simulation software.

Our next question is that of how γ comes from the two impedances. Stating the conclusion first, the aforementioned reflectance can be formulated as

$$\gamma = \left| \frac{Z_2 - Z_1}{Z_2 + Z_1^*} \right|, \tag{3}$$

where the superscript asterisk * denotes the complex conjugate.

Some undergraduates may be puzzled as to why the asterisk stays solely in the denominator of (3) and not in the numerator. The answer is easy: this formula can be derived by just imposing the basic Ohm's law on the RF voltages and currents in a simple lumped-constant system. This can be done even without assuming transmission lines or wave propagation. A full description of this elegant theory is provided in [4].

We now have a powerful tool to measure the Poincaré distance, that is, the three-step sequence (3)–(2)–(1) displayed in Figure 4. This sequence is highly versatile because (1), (2), and (3) are valid not only for a Cartesian chart; they are also valid for any kind of chart, regardless of its shape, scale, or coordinate gradation. This wide validity can be directly derived from the formulas themselves. Moreover, reference impedance Z_o does not affect γ, ρ, or D at all. Obviously, these quantities are functions only of Z_1 and Z_2.

Triangle Mystery

Charles Berlitz warned travelers never to sail into the Bermuda Triangle, but we now gather momentum toward the triangle shown in Figure 1 with full curiosity in mind. Upon reaching vertex Z_1, our first assignment is to measure the distance between Z_1 and Z_1 itself. A zero distance may sound trivial, but it actually makes sense, as it resembles the 0-Ω calibration of circuit testers or impedance analyzers. By substituting $Z_1 = Z_2$ into (1), (2), and (3) in Figure 4, we can sequentially confirm that $\gamma = 0$, and thus $\rho = 1$, resulting in $D = 0$ as expected. The verification is successful. Our instruments are go!

Next we steer our boat to vertex Z_2, where our second assignment is to measure the distance between Z_1 and Z_2. Reading out their positions as $Z_1 = 10 + j20$ and $Z_2 = 10 - j10$ from the grid and inserting these complexes into (3), we obtain

$$\gamma_{12} = \left| \frac{(10 + j20) - (10 - j10)}{(10 + j20) + (10 + j10)} \right| = \frac{3}{\sqrt{13}}, \tag{4}$$

where the combined subscript $_{12}$ denotes the corresponding points Z_1 and Z_2. Substituting this result into (2) and (1), we obtain

$$D_{12} = \ln \frac{\sqrt{13} + 3}{\sqrt{13} - 3} \approx 2.4. \tag{5}$$

This is the distance between Z_1 and Z_2 observed in the Poincaré metric.

In (5), there is no unit appended to the figure. This is quite natural for dimension-free quantities. However, if units are required, the answer is neper (Np) for the quantity stemming from the natural logarithm. Another

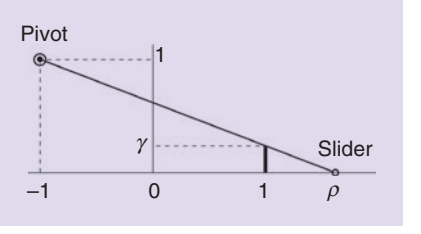

Figure 3. *An elastic-cord model to explain the γ-to-ρ conversion.*

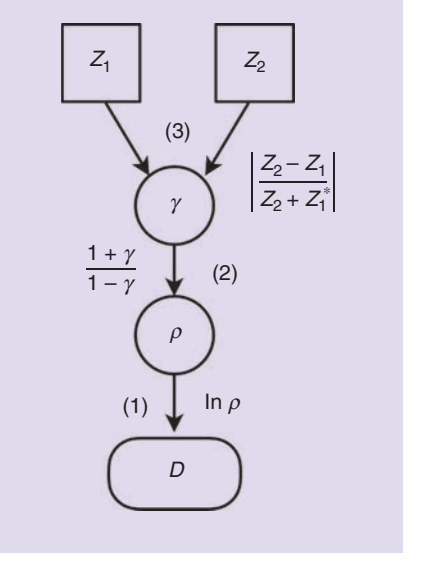

Figure 4. *A flowchart to measure the Poincaré distance between Z_1 and Z_2.*

TABLE 1. The reflectance-to-VSWR conversion lookup table.

γ	0	0.2	0.5	0.6	0.75	0.8	0.9	1
ρ	1	1.5	3	4	7	9	19	∞

option we have is to convert Np into decibel (dB), which is defined as 20 times the common logarithm and is thus familiar to radio engineers. It is quite impressive that 20 $\log_{10}$ VSWR lives in perfect harmony with M.C. Escher's art work, as pointed out by Gupta in [3]. For quick conversion, 1 Np ≈ 8.686 dB.

We finally sail to vertex Z_3 of the triangle, carrying a twofold mission: to measure both D_{23} and D_{31} at once. Repeating the same calculation process as in (4) and (5), we obtain

$$\gamma_{23} = \left| \frac{(50 - j10) - (10 - j10)}{(50 - j10) + (10 + j10)} \right| = \frac{2}{3}, \quad (6)$$

$$D_{23} = \ln \frac{3+2}{3-2} \approx 1.6, \quad (7)$$

$$\gamma_{31} = \left| \frac{(50 - j10) - (10 + j20)}{(50 - j10) + (10 - j20)} \right| = \frac{\sqrt{5}}{3}, \quad (8)$$

$$D_{31} = \ln \frac{3+\sqrt{5}}{3-\sqrt{5}} \approx 1.9. \quad (9)$$

Comparing the three distances, we can conclude that $D_{23} < D_{31} < D_{12}$. This inequality apparently disagrees with how the triangle looks in Figure 1 under the lamp of traditional geometry. That is why this plane seems so mysterious.

Which route is shorter, the curve or the straight line?

Piecewise Segmentation

When we make a long-haul voyage, the shortest or geodesic route is not always available. Sometimes, a tidal current or a jet stream dominates our course. This is also true in radio engineering. Imagine that we design an impedance transformer from Z_1 to Z_2. A wide variety of lumped and distributed-constant elements can be used. However, these elements seldom follow the shortest path to reach the target impedance on the plane [5]–[7]. This is why the length of curved routes must be considered apart from the direct distance described in the previous section.

According to differential geometry, a smooth curve can be measured by a line integral of infinitesimal segments along the curve. We begin with a small segment truncated at Z_1 and Z_2, as shown in Figure 5. The two points are denoted as

$$Z_1 = R + jX, \quad (10)$$

$$Z_2 = R + jX + \delta Z, \quad (11)$$

where δZ implies a slight difference between the two points on the R-X plane.

Again, we follow the three-step sequence (3)–(2)–(1) depicted in Figure 4. Substituting (10) and (11) into (3), we obtain

$$\gamma = \left| \frac{Z_2 - Z_1}{Z_2 + Z_1^*} \right| = \frac{|\delta Z|}{|2R + \delta Z|}. \quad (12)$$

Then, substituting (12) into (2) and expanding the result into its first-order Maclaurin series with respect to $|\delta Z|$, we obtain

$$\rho = \frac{1+\gamma}{1-\gamma} = \frac{|2R + \delta Z| + |\delta Z|}{|2R + \delta Z| - |\delta Z|} = 1 + \frac{|\delta Z|}{R}, \quad (13)$$

in which the higher-order terms can be omitted because they are negligible. Finally, substituting (13) into (1) and applying the same expansion mentioned previously, we obtain

$$D = \ln \rho = \ln\left(1 + \frac{|\delta Z|}{R}\right) = \frac{|\delta Z|}{R} \quad (14)$$

for the distance between Z_1 and Z_2. See Figure 6 for graphical assistance to grasp what (14) means.

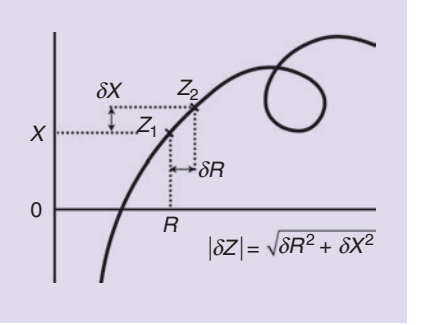

Figure 5. *A smooth curve and its segment on the impedance half-plane.*

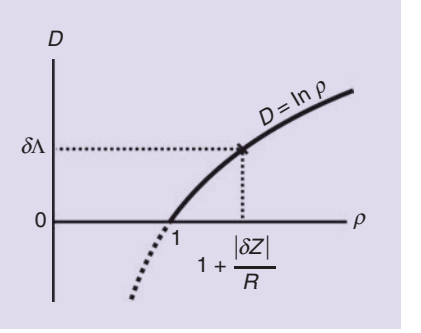

Figure 6. *A small segment length stems from the natural logarithm of VSWR. We find that $\delta\Lambda = |\delta Z|/R$ because the curve has a 45° slope in the vicinity of unity.*

The segment length is a small increment of VSWR from unity.

Assuming that the curve is smooth and the segment sufficiently small, the aforementioned distance can be equivalently regarded as the segment length. The impedance difference is decomposed into its real and imaginary parts as

$$\delta Z = \delta R + j\delta X. \quad (15)$$

Looking at Figures 5 and 6 together, we can rewrite (14) as

$$\delta\Lambda = \frac{|\delta Z|}{R} = \frac{1}{R}\sqrt{\delta R^2 + \delta X^2}. \quad (16)$$

This is the Poincaré distance between two adjacent impedances. From this result, we conclude that the small segment length is given by the absolute difference in impedance normalized to its original resistance. Note that the original reactance X does not contribute to the length at all. Finally, above $\delta\Lambda$ is accumulated as

$$\Lambda = \int_C d\Lambda \quad (17)$$

to measure the entire curve length Λ, where the prefix δ is replaced by the infinitesimal operator d. Sequence (15)–(16)–(17) is summarized as a flowchart in Figure 7.

Curve Length

Now let us look back at the mysterious triangle presented in Figure 1. We sail

from vertex Z_1 to Z_2 once again. This time, however, the route is segmented into small pieces that are integrated in length. For simplicity, we assume that this route is a circular arc lying along the circle that passes through Z_1 and Z_2 and is centered on the x-axis. Reading out its location from the grid, the circle is formulated as

$$R^2 + (X-5)^2 = 325. \tag{18}$$

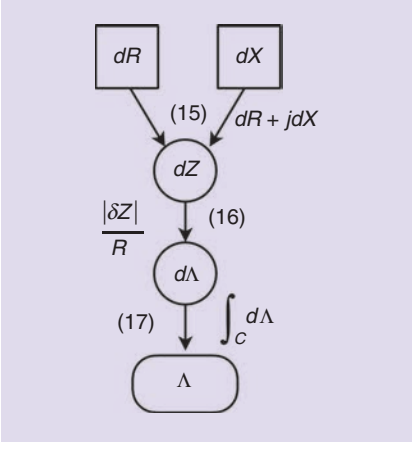

Figure 7. *A flowchart to measure the Poincaré length of a smooth curve.*

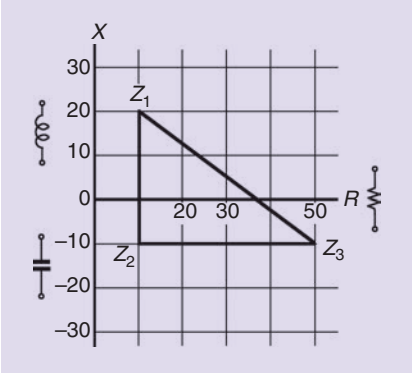

Figure 8. *A pseudotriangle on the impedance half-plane.*

TABLE 2. The triangle dimensions in the Poincaré metric.

	Z_1–Z_2	Z_2–Z_3	Z_3–Z_1
Distance D	2.4	1.6	1.9
Length Λ in Figure 1	2.4	1.6	1.9
Length Λ in Figure 8	3	1.6	2

By differentiation, the curve's slope is calculated as

$$\frac{dR}{dX} = -\frac{X-5}{R}. \tag{19}$$

This slope enables us to eliminate δR from (16), resulting in

$$\begin{aligned} d\Lambda &= \frac{1}{R}\sqrt{dR^2 + dX^2} = \frac{5\sqrt{13}}{R^2}dX \\ &= \frac{1}{2}\left| \frac{1}{X-5+5\sqrt{13}} \right. \\ &\quad \left. - \frac{1}{X-5-5\sqrt{13}} \right| dX, \end{aligned} \tag{20}$$

where δ reduces to the infinitesimal operator d. Integrating this $d\Lambda$ from Z_2 to Z_1, the arc is measured as

$$\begin{aligned} \Lambda_{12} &= \int_{Z_2}^{Z_1} d\Lambda \\ &= \left[\frac{1}{2} \ln \left| \frac{X-5+5\sqrt{13}}{X-5-5\sqrt{13}} \right| \right]_{-10}^{20} \\ &= \ln \frac{\sqrt{13}+3}{\sqrt{13}-3} \approx 2.4. \end{aligned} \tag{21}$$

Although the calculation has been a little bit tough this time, the resultant length is identical to the distance observed in (5). This identity means that the assumed arc is the shortest route that links the two vertices. This is because, in general, the length can never be less than the distance. In a similar way, we can also confirm that $D_{23} = \Lambda_{23}$ and $D_{31} = \Lambda_{31}$. Thus, we conclude that this shape should be called a *triangle* even though it looks distorted.

Pseudotriangle

We now move on to another mysterious triangle, as seen in Figure 8. We find that it resembles the triangle in Figure 1; the only difference is that its three sides are all straight lines rather than curves. Looking at Figures 1 and 8 in parallel, let us pose the following question: Which side is longer, the curve or the straight line?

The straight line from Z_1 to Z_2 is read out as $R = 10$ and $-10 < X < 20$. Therefore, $dR = 0$, and, thus, (16) simply reduces to

$$d\Lambda = \frac{1}{10}|dX|. \tag{22}$$

Integrating from Z_2 to Z_1, the line measures

$$\begin{aligned} \Lambda_{12} &= \int_{Z_2}^{Z_1} d\Lambda \\ &= \frac{1}{10}\int_{-10}^{20} dX = \frac{1}{10}[X]_{-10}^{20} = 3. \end{aligned} \tag{23}$$

This result finds a roughly 25% increment from (5) or (21). We can therefore answer the quiz: the straight line is longer than the curve. This answer is diametrically opposed to common sense, considering usual geometry.

Let us see the next line shown in Figure 8. The straight line from Z_2 to Z_3 is read out as $10 < R < 50$ and $X = -10$. Therefore, $dX = 0$, and, thus, (16) reduces to

$$d\Lambda = \frac{1}{R}|dR|. \tag{24}$$

Integrating from Z_2 to Z_3, the line measures

$$\begin{aligned} \Lambda_{23} &= \int_{Z_2}^{Z_3} d\Lambda \\ &= \int_{10}^{50} \frac{1}{R} dR = [\ln R]_{10}^{50} = \ln 5 \approx 1.6. \end{aligned} \tag{25}$$

This is identical to the result from (7), which is completely natural because this route is a straight baseline common to both triangles.

The final line shown in Figure 8 runs from Z_1 to Z_3 at a slant, which is formulated as

$$X = -\frac{3}{4}R + \frac{55}{2} \tag{26}$$

for $10 < R < 50$. Therefore, $dX = -3/4\, dR$, and, thus, (16) reduces to

$$d\Lambda = \frac{5}{4R}|dR|. \tag{27}$$

Integrating from Z_1 to Z_3, the line measures

$$\begin{aligned} \Lambda_{13} &= \int_{Z_1}^{Z_3} d\Lambda \\ &= \int_{10}^{50} \frac{5}{4R} dR = \frac{5}{4}[\ln R]_{10}^{50} \\ &= \frac{5}{4}\ln 5 \approx 2.0. \end{aligned} \tag{28}$$

By comparing this result with (9), we can say again that the straight line is longer than the curve. See Table 2 for an overview of the two triangles in dimension.

In summary, the shape in Figure 8 looks like a triangle, but its sides do not always link the corresponding vertices with the minimum length. In this sense, even having three angles, it should be called a *pseudotriangle*.

The route looks straight but is curved in a sense.

Zero and Infinity

Although the adventure on the impedance half-plane is not yet exhausted, we leave its further exploration to brave future challengers. Let us now steer our vessel from the triangular zone toward a circular island with full rudder.

The question here is, on what kind of plane can we meet both zero (short) and infinity (open) (as they cannot simultaneously live in a Cartesian town)? This is because infinity is too far on the aforementioned impedance plane, whereas zero is too far on the admittance plane. To overcome this antipodal conflict, instead of the Cartesian scale, a nonlinear scale for the coordinates is required.

One solution to this puzzle is to employ the reflectance magnitude γ as a radial scale. It is already known that γ ranges from zero to unity, never diverging even for an open, short, or any positive real impedance. The plane, in general, must be a 2D world. Therefore, in addition to the magnitude, the phase θ of the reflection must be taken into account. Thus, we involve γ and θ in the polar-coordinate complex reflectance

$$\Gamma = \gamma e^{j\theta} = \frac{\rho - 1}{\rho + 1} e^{j\theta}, \tag{29}$$

where ρ denotes the VSWR once seen in (2). Explicitly, $\gamma = |\Gamma|$, and $\theta = \angle\Gamma$. The final right-hand side in (29) is called the *VSWR expression of complex reflectance*, which will be exploited in the final section.

It is also known that the reflectance can be calculated from

$$\Gamma = \frac{R + jX - 50}{R + jX + 50} \tag{30}$$

in a 50-Ω system. For example, $\Gamma = -1$ when $R = X = 0$. To see how Γ behaves in response to impedance, we sweep R and X from zero to infinity and plot Γ on a complex plane. The result is presented in Figure 9. We find that zero and infinity can successfully live together in one world. This elegant projection is called a *Poincaré disk* in hyperbolic geometry [2], [3], [8] and is also known as a *Smith chart* in radio engineering [9], [10].

The shape in Figure 8 looks like a triangle, but its sides do not always link the corresponding vertices with the minimum length.

How can zero and infinity live in one world?

Power Ratio

The disk shown in Figure 9 was indeed an elegant discovery and is even now working for us on the visual display of electromagnetic field simulators and vector network analyzers and on the blackboard in microwave engineering classrooms. However, at least in geometry, this disk is not the only solution for zero and infinity to coexist. Looking further forward, let us continue our voyage to seek another circular island.

If we accept the concept of the power standing-wave ratio (PSWR), denoted as ρ^2, a favorable wind will

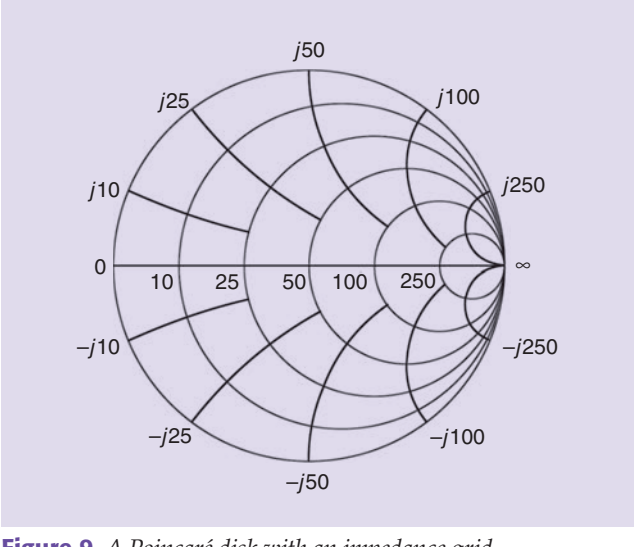

Figure 9. *A Poincaré disk with an impedance grid.*

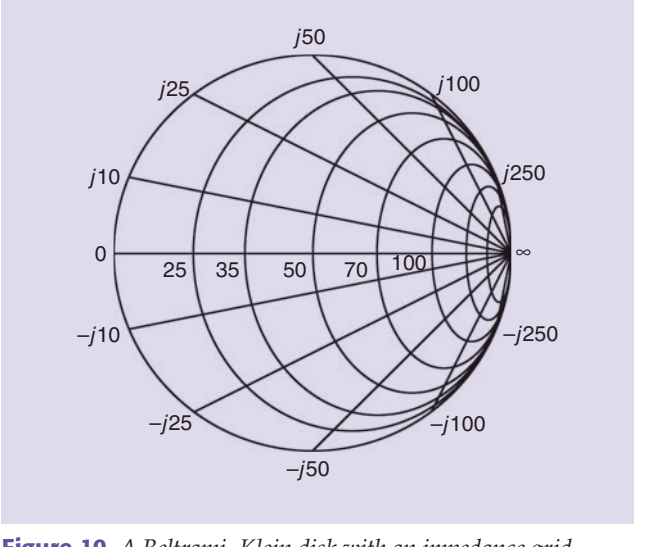

Figure 10. *A Beltrami–Klein disk with an impedance grid.*

blow to hoist our sails. This notation, ρ^2, is based on the common circuit theorem: voltage ratio squared equals power ratio. Now, even though it may sound somewhat abrupt, it is quite convenient to thrust this PSWR into the complex reflectance. By just replacing ρ with ρ^2 on the final right-hand side of (29), we define a new complex:

$$\Omega = \frac{\rho^2 - 1}{\rho^2 + 1} e^{j\theta}. \tag{31}$$

This simple replacement makes a difference only in magnitude; the phase is kept unchanged from the original Γ. Because the right-hand side in (31) ranges from zero to unity in magnitude at any phase, we notice that Ω draws a circular disk on the complex plane as well as Γ does. In other words, this disk meets the prime requirement of zero and infinity as well as the Smith chart does.

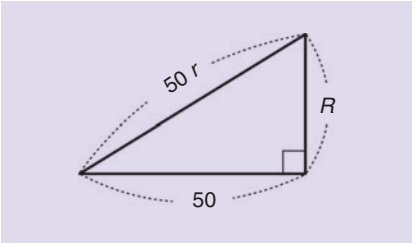

Figure 11. *A right triangle can be used to remember the axial ratio's elegant law.*

To thoroughly comprehend how Ω behaves on the plane, it is helpful to formulate Ω in terms of Γ. By substituting (2) and (29) into (31), we can eliminate ρ and θ at the same time, resulting in

$$\Omega = \frac{2\Gamma}{1 + \Gamma\Gamma^*}. \tag{32}$$

Upon encountering this formula, might students feel something come to their attention? Yes, this is congruent with the double-angle rule of hyperbolic tangent, except for the conjugation on the denominator's final term. In any case, using this formula, we can sail directly from the familiar Γ island to the new Ω island.

With the help of (32), we can convert (30) into

$$\Omega = \frac{R^2 + (X + j50)^2}{R^2 + X^2 + 50^2}, \tag{33}$$

which projects the *R*-*X* grid within the disk, as seen in Figure 10. This chart is called the *Beltrami–Klein disk* in hyperbolic geometry [2], [11], [12]. On this disk, we notice ellipses in the north–south symmetry with respect to the Equator, commonly contacting the East Pole (or West Pole in Australia-orientated maps). These ellipses are called *horocycles* in hyperbolic geometry. They physically mean constant-*R* contours, along which *X* ranges from negative to positive infinity. Focusing on the ellipse's axial ratio *r*, we find

$$50^2 + R^2 = 50^2 r^2, \tag{34}$$

where *R* is the resistance read out at the ellipse's west-side interception across the Equator. This formula is so elegant that students can quickly grasp it. Those who are better at geometry than at algebra can memorize this law via the equivalent right triangle depicted in Figure 11 using the Pythagorean proposition.

We also notice straight lines all converging on the East Pole. These lines are called *geodesics* in hyperbolic geometry. They physically mean constant-*X* contours, along which *R* ranges from zero to infinity. It is a remarkable feature of this disk that all the constant-*X* contours lie in straight chords, in contrast with the circular arcs on the Smith chart shown in Figure 9.

Voltage ratio squared equals power ratio.

Back to the Future

Now it is almost time to bid goodbye to 19th-century geometry and fuel our vessel to sail back to the future. We have three triangles and two circular disks to keep in our treasure box. On finalizing this fruitful adventure, we sincerely express our full respect to Eugenio Beltrami and Henri Poincaré by displaying their portraits in Figure 12. Imagine if we could invite these two great mathematicians to our International Microwave Symposium and give them the chance to know our technical term SWR: they might have presented in a special memorial session how to formulate their circular disks, as in their speech balloons.

Figure 12. *Henri Poincaré (left) (1854–1912) and Eugenio Beltrami (1835–1900).*

Make geometry great again.

Acknowledgments

The author appreciates the constructive comments given by Prof. Siegfried Martius from the Universität Erlangen Nürnberg and Prof. Kiyomichi Araki from the Tokyo Institute of Technology. Thanks also to Marimo Matsumoto from the Toyohashi University of Technology for her help with the portrait illustrations. This work is granted by the Council for Science, Technology, and Innovation; the Cross-Ministerial Strategic Innovation Promotion Program; and the Knowledge Hub Priority Research Project from the Aichi Prefectural Government.

References

[1] H. A. Wheeler, "Reflection charts relating to impedance matching," *IEEE Trans. Microw. Theory Techn.*, vol. 32, no. 9, pp. 1008–1021, Sept. 1984. doi: 10.1109/TMTT.1984.1132814.

[2] A. Ramsay and R. D. Richtmyer, *Introduction to Hyperbolic Geometry*. New York: Springer-Verlag, 1995, pp. 202–217.

[3] M. S. Gupta, "Escher's art, Smith chart, and hyperbolic geometry," *IEEE Microw. Mag.*, vol. 7, no. 5, pp. 66–76, Oct. 2006. doi: 10.1109/MWM.2006.247916.

[4] T. Ohira, "Standing wave ratio," *IEEE Microw. Mag.*, vol. 21, no. 2, pp. 108–109, Feb. 2020. doi: 10.1109/MMM.2019.2952041.

[5] P. Sjöblom and H. Sjöland, "Constant mismatch loss boundary circles and their application to optimum state distribution in adaptive matching networks," *IEEE Trans. Circuits Syst. II*, vol. 61, no. 12, pp. 922–926, Dec. 2014.

[6] K. Yamada et al., "Graphical representation of the power transfer efficiency of lumped-element circuits based on hyperbolic geometry," *IEEE Trans. Circuits Syst. II*, vol. 64, no. 5, pp. 485–489, May 2017. doi: 10.1109/TCSII.2016.2580626.

[7] C. Li et al., "A graphical analysis on compensation designs of large-gap CPT systems," *CES Trans. Elect. Mach. Syst.*, vol. 2, no. 2, pp. 232–242, June 2018. doi: 10.30941/CESTEMS.2018.00029.

[8] T. Ohira, "Poincaré length," *IEEE Microw. Mag.*, vol. 21, no. 3, pp. 120–121, Mar. 2020. doi: 10.1109/MMM.2019.2958799.

[9] P. H. Smith, "Transmission line calculator," *Electronics*, vol. 12, no. 1, pp. 29–31, Jan. 1939.

[10] T. Mizuhashi, "Theory of four-terminal impedance transformation circuit and matching circuit," *J. Inst. Elect. Commun. Eng. Jpn*, vol. 21, no. 12, pp. 1053–1058, Dec. 1937.

[11] T. Ohira, "Beltrami–Klein disk model as viewed for use in impedance trajectory projection," *IEICE Commun. Expr.*, vol. 9, no. 7, pp. 256–261, July 2020. doi: 10.1587/comex.2020XBL0016.

[12] T. Ohira and S. Abe, "Power standing wave ratio as a local grid magnifier for close observation of impedance trajectories (invited)," in *Proc. IEEE Int. Symp. Radio-Frequency Integration Technology*, Hiroshima, Japan, Sept. 2020.

MTT-S Society News

Spotlight on MTT-S Administrative Committees

■ **Goutam Chattopadhyay and Robert H. Caverly**

The following interview is the second in a series of Spotlight articles that take an in-depth look at some of the committees that make up the IEEE Microwave Theory and Techniques Society (MTT-S) Administrative Committee (AdCom). I spoke with the chair of the Meetings and Symposium (M&S) Committee, Dr. Goutam Chattopadhyay (GC).

©SHUTTERSTOCK.COM/NATBASIL

Thank you, Dr. Chattopadhyay, for agreeing to be interviewed for our new Spotlight series and to discuss some background of the M&S Committee. What exactly is the main purpose of the M&S Committee?

GC: Conferences are the first place where we present to our peers fresh-out-of-the-oven research results and new products. They bring together students, young professionals (YPs), researchers, industry leaders, and experts under the same roof and provide an opportunity to interact, exchange ideas, discuss lessons learned, present preliminary results, and fine-tune product concepts based on user feedback. Moreover, conferences provide the perfect platform to network, especially for students and researchers in their early careers. Here, they can rub shoulders with company CEOs/CTOs [chief executive officers/chief technology officers] to pitch their product ideas and discuss research ideas, breakthroughs, failures, and future paths forward with other researchers, professors, and experts in the field.

The MTT-S sponsors and cosponsors, both financially and technically, more than 40 conferences per year, which are held all over the globe on a variety of topics covering megahertz to terahertz frequencies. The depth and breadth of the MTT-S conferences are astounding and contribute tremendously to the success of our Society. The role of the M&S Committee is to perform due diligence in approving conference applications and to provide financial and technical guidance and assistance in helping the organizers carry out successful conferences. The M&S Committee also makes sure that the conferences organized under the MTT-S banner are of the highest quality and are managed with the highest ethical standards. Organizing conferences—large or small—is not a simple task, and the

Goutam Chattopadhyay (goutam@ieee.org), senior research scientist with the NASA Jet Propulsion Laboratory, California Institute of Technology, Pasadena, is chair of the MTT-S Meetings and Symposium Committee. Robert H. Caverly (rcaverly@villanova.edu), editor-in-chief of IEEE Microwave Magazine, *is with Villanova University, Villanova, Pennsylvania.*

Digital Object Identifier 10.1109/MMM.2020.3014993
Date of current version: 6 October 2020

M&S Committee, with its vast experience and expertise, helps organizers navigate the different stages of conference organization. Also, the M&S Committee, with the support of the MTT-S AdCom, acts as a bridge between conference organizers and the IEEE Meetings, Conferences, and Events (MCE) Committee, which is the umbrella organization for all IEEE meetings and conferences.

Where does an MTT-S member see the impact of M&S's work?

GC: MTT-S members see the impact of the M&S Committee's work at the conferences. The conferences, along with our journals and periodicals, are the prime reason people become MTT-S members. The conferences that MTT-S sponsors, both financially and technically, are always of the highest quality in technical content, organization, and attendee experience. The M&S Committee follows a rigorous process for conference approval. Conference organizers are asked to provide detailed plans, which include the makeup of the organizing committee (the general chair, TPC [Technical Program Committee] chair, and treasurer), the technical content, paper acceptance rate, prior years' technical and financial performance, and other relevant information. The M&S Committee evaluates and then approves or denies the conference application. For financially sponsored conferences, the M&S Committee approval is followed by MTT-S Budget Committee and AdCom approval. The most important criteria we follow when approving conference applications are the technical quality and the quality of the attendee experience.

The other impact of the M&S Committee that the MTT-S members see is at conference registration. The M&S Committee, with the approval of the Budget Committee and the AdCom, has implemented a conference registration discount process for MTT-S members attending MTT-S financially sponsored conferences. This not only encourages participants to become MTT-S members; it also gives current members some additional benefits.

What are some of the accomplishments of the M&S in the last two years that the general MTT-S member would have seen?

GC: In our continued effort to serve the needs of our members and the microwave community around the world at large, the M&S Committee has been looking into improving the topical and geographic coverage of our conferences. The committee has been actively looking into the areas and topics of our Society's fields of interest that are not being adequately represented in the existing slate of conferences. Based on feedback from Society members and microwave practitioners, we have started two new financially sponsored conferences: the International Microwave Filter Workshop and the International Conference on Microwave Acoustics and Mechanics.

The African continent is one of the geographic areas where there is a lot of interest in microwave-related activities but where we do not sponsor many conferences. Over the past few years, we worked closely with our colleagues in Africa in starting the International Symposium on Microwaves and Antennas, a 100% MTT-S financially sponsored conference. This conference will move around to different parts of Africa. The first edition was supposed to be in Cairo, Egypt, in early 2021, but, due to the COVID-19 situation, it will now be held in early 2022.

Additionally, over the last two years, the M&S Committee has improved the process of conference organization. The M&S Committee has streamlined the guidelines and provides training and other logistical support, helps TPC chairs with subject matter experts by connecting them to the appropriate technical committee chairs and their members, and puts them in contact with the Marketing Committee to help them with conference advertisement and sponsorship.

How did the procedures change in the M&S Committee when dealing with the pandemic and its impact on conferences?

GC: COVID-19 has had an unprecedented disruptive effect on all aspects of our lives, and the M&S Committee and our conferences have been no exception. Since March 2020, there has been a rush to postpone, cancel, or go virtual for most MTT-S conferences scheduled for the rest of the year. Traditionally, any change to an approved conference requires M&S Committee approval and, for financially sponsored conferences, subsequent Budget Committee and AdCom approval.

Since the COVID-19 disruptions happened on such a massive scale and the conference organizers needed to make decisions on an expedited basis (cancellations of venues, hotel rooms, and other commitments, which usually have a big financial impact), we quickly realized that it was not possible for us to work on a case-by-case basis and solicit approval from multiple committees. We had to be nimble and act fast, and a new strategy was necessary. The AdCom authorized the M&S Committee chair to approve any changes in the conference schedule (for 2020 conferences) by consulting with the conference chairs, conference Executive Committee chair, MTT-S president, Budget Committee chair, and treasurer. This, along with help and support from the IEEE MCE, was pivotal in dealing with the rapidly evolving situation. After innumerable WebEx and Zoom meetings with the different stakeholders, we were able to stabilize the situation.

Many conferences have been rescheduled to the latter part of the year, some have been postponed by one year, a few are going virtual, and some are going to a hybrid mode—a mix of virtual and in person. With help from the conference organizers, M&S Committee members, the AdCom, and others, we dealt with the situation as best as we could. All our decisions were primarily based on keeping in

mind the health and well-being of our members and conference attendees. We are making sure that the M&S Committee provides all the support that conference organizers need.

As a follow up, about how long before the conference went virtual or was postponed were the decisions made?

GC: That varied from conference to conference. Conferences scheduled in the first quarter of 2020 had to act fast in March when the pandemic hit hard. Some conference organizers wanted to wait and watch before making decisions, as those conferences were scheduled toward the end of the calendar year. A few decided to get ahead of the curve and postpone by a year given the uncertainty of the pandemic recovery. A couple of conferences were postponed to a later date and then the organizers came back and decided to do a virtual conference at the changed dates. At this point, we are providing maximum flexibility to organizers and not imposing any artificial deadlines for them to reschedule. If it is at all possible to decide early, we are encouraging that option, but the decisions are made based on the situation on the ground. Our approach has been to provide conference organizers with help and guidance so that they can make the best possible decision for the attendees and MTT-S volunteers.

The conferences, along with our journals and periodicals, are the prime reason people become MTT-S members.

What are some of the plans that the M&S Committee is working on that the general MTT-S member should be looking forward to?

GC: We are joining hands with the MTT-S YPs to bring in more students and young engineers and researchers to our conferences. Students and YPs are our future, and we are trying to develop the next generation of leaders by encouraging YPs to take up more active roles in conference organization. We are also exploring the possibility of live-broadcasting the keynote and plenary lectures of conferences through the mtt.org website. We believe that will not only act as an advertisement for conferences and future events but also will allow other members to attend those lectures virtually. We are also planning to broadcast some conference-related materials prior to the keynote/plenary lectures. To bring in more YPs and women in microwaves (WiM) at our conferences, we are encouraging the conference organizers to select a YP/WiM as one of the keynote/plenary speakers for their conferences.

As an MTT-S member, how can I make a contribution to help with the work related to M&S Committee?

GC: The MTT-S is run by volunteers, and one of the high-impact acts of volunteerism is through conference organization. We highly encourage MTT-S members to get involved in conference organization and to be a part of the local organizing committee. It's a great learning experience and highly rewarding. If members do not know how to become part of the conference organizing team, please reach out to one of the M&S Committee members, and we will put you in contact with the organizing team. The best way to contribute to the M&S Committee's work is to attend conferences and send us suggestions and ideas as to how we can improve the quality and attendee experience of our conferences.

What made you want to become the chair of M&S Committee?

GC: Prior to getting elected as an MTT-S AdCom member, I was a Distinguished Microwave Lecturer. In that role, I traveled to different parts of the globe; interacted with students, YPs, researchers, industry experts, and others; and observed firsthand the enthusiasm they all have about microwaves, millimeter-waves, and terahertz. I also noticed the gaps that exist in different regions: in many parts of the world, there are not many microwave conferences to attend. Moreover, often people from those regions do not have the means to travel to the IEEE MTT-S International Microwave Symposium or to our other flagship conferences. I felt that we needed to address those needs. Therefore, when I got elected to the AdCom, I joined the M&S Committee as the vice-chair under the leadership of the then M&S Committee chair, Dr. Maurizio Bozzi.

At the M&S Committee, we started our work to establish a new conference in Africa. Earlier this year, I was entrusted with the responsibility of being the chair of the M&S Committee. Additionally, it was quite clear to me that we urgently needed to address the gender, racial, and age-group diversity of our Society as well as at our conferences. I felt that, as the chair of the M&S Committee, I would be able to work closely with WiM Chair Prof. Wenquan (Cherry) Che and incredible YPs such as Dr. Tushar Sharma and others to bring in the necessary changes and address those shortcomings.

At our conferences, we are now trying to have dedicated sessions when there are no other parallel sessions, similar to a keynote and plenary session, entirely devoted to Women in Engineering (WiE), WiM, and YPs. At the 2019 International Microwave and RF Conference in Mumbai, India, where I was the co-general chair, we had a wonderful special session on WiE/WiM/YPs. There were dedicated technical sessions by WiMs and YPs as well as panel discussions related to gender equality and diversity. I believe it is imperative for all of us to go out of our way to recruit women, people of color, and YPs in conference organization and leadership roles. These leaders are out there, and our role as the leaders of our Society is to encourage and help them in any possible way to make that happen.

IEEE TRANSACTIONS ON
MICROWAVE THEORY AND TECHNIQUES
A PUBLICATION OF THE IEEE MICROWAVE THEORY AND TECHNIQUES SOCIETY

IEEE Transactions on Microwave Theory and Techniques

Special Issue on

Microwave and Millimeter-Wave Communication and Sensor Systems

New Submission Date: 26 February 2021, Publication Date: October 2021

Motivation

The aim of this Special Issue is to publish technical papers in microwave and millimeter-wave communication and sensor systems. In recent years, we have seen a strong resurgence in such systems due to 5G and satellite communications (SATCOM), automotive radars, precise location services, UAV tracking, imaging radars, STAR (simultaneous transmit and receive systems also known as self-duplex), power amplifiers with digital pre-distortion, antenna tuning with closed loop functions, etc. Also, silicon chips are becoming more complex with multiple transmit and receive beamforming channels, up and down-conversion mixers, synthesizers, ADCs and DACs and even digital signal processing decision circuitry all on the same die. The silicon (and III-V front-end) solutions can be considered as stand-alone and are connected to antennas (or antenna arrays) for operation. For such complex systems, it is not required to know the detailed operation of every circuit or component, and it is more important to look at the solution from a systems perspective, such as co-design of the RF blocks with the antennas and with the DSP back-end, and the decision algorithms for the respective application areas. Also, calibration and test of such complex systems is critical, and novel techniques are needed to reduce the calibration cost which can lead to a reduction in system cost. The increased impact of microwave and millimeter-wave systems is noticeable throughout society, especially in 5G communications, automotive radars, safety/security applications, and in bio-medical sensors.

Topics of interest to be covered by the Special Issue include, but are not limited to

- *Systems and system-level demonstrations for communications and radar sensing*, including but not limited to: active and passive phased arrays using different beamforming technologies, MIMO arrays, repeaters, self-duplex and active nulling arrays, polarization diversity, closed-loop antenna tuning solutions, dual- or multi-band arrays, reconfigurable arrays, calibration and test techniques, etc. Applications for 5G, point-to-point links, SATCOM, automotive radars, position sensing, and other standards are especially welcome.
- *System-level integrated circuits and/or sub-systems using multiple chips*, including but not limited to: communication and radar chips with multi-channel transceivers, power amplifiers with wideband digital pre-distortion and envellope tracking, signal cancelling chips for self-duplex systems at the RF, IF and DSP level, and other complex systems on a chip. Circuits using solid-state (BiCMOS, SiGe, CMOS, SOI CMOS, GaAs, GaN and any combination) and non-solid-state technologies (RF MEMS, BST, liquid crystal, phase-change, etc.) are solicited.
- *Packaging and module technologies*, including but not limited to: complex packaging design for multifunction wideband systems, high power/thermal considerations, module technologies for receivers and transmitters, antennas-in-package and wafer-scale systems.
- *Review papers*, including but not limited to: papers summarizing the state of the art in automotive radars, SATCOM, 5G, point-to-point links, sensing systems, power amplifier digial predistortion, etc. are also encouraged. Potential authors should contact the editors to discuss their submission and to get approval for this special category.

Authors must consult the link https://www.mtt.org/author-information-transactions/ for submission instructions.

Guest Editors

Prof. Gabriel M. Rebeiz
University of California, San Diego, USA
rebeiz@ece.ucsd.edu

Prof. James F. Buckwalter
University of California, Santa Barbara, USA
buckwalter@ece.ucsb.edu

Digital Object Identifier 10.1109/MMM.2020.3020486

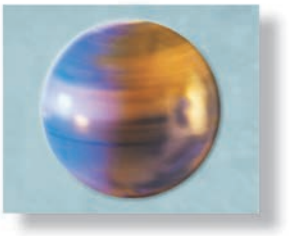

Around the Globe

Maxwell, Einstein, Newton, and Faraday

■ **David O. Forfar**

When Einstein made his first visit to the United Kingdom, the press asked him if he had stood on the shoulders of Newton. Einstein replied, "That statement is not quite right. I stood on Maxwell's shoulders."

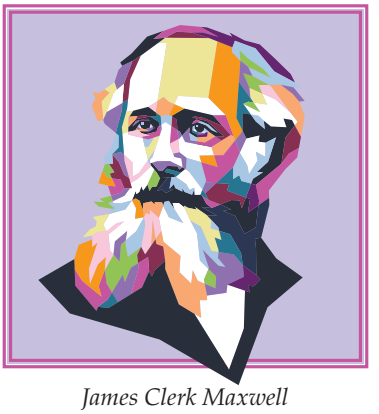

James Clerk Maxwell

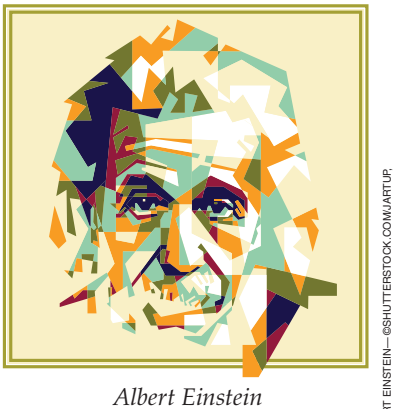

Albert Einstein

Issac Newton

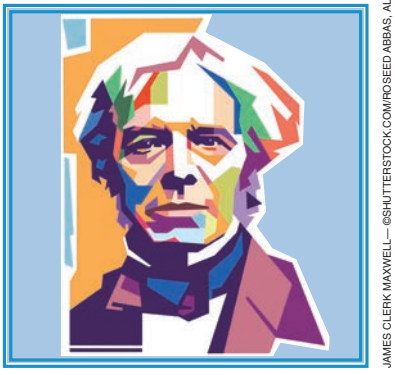

Michael Faraday

JAMES CLERK MAXWELL— ©SHUTTERSTOCK.COM/ROSEED ABBAS. ALBERT EINSTEIN— ©SHUTTERSTOCK.COM/JARTUP. ISSAC NEWTON— ©SHUTTERSTOCK.COM/WPAP. MICHAEL FARADAY— ©SHUTTERSTOCK.COM/SAHROE

James Clerk Maxwell Foundation

This article is reprinted from the 2012 *Maxwell Newsletter*, with the permission of the James Clerk Maxwell Foundation (JCMF), which is dedicated to the life and history of Clerk Maxwell. A wealth of information is available at http://www.clerkmaxwellfoundation.org/. In addition, the JCMF owns and maintains an extensive collection of Maxwell material at his birthplace, 14 India Street, Edinburgh, Scotland. When travel conditions return to normal, visitors are most welcome. This article was arranged by David Forfar and James Rautio, both trustees of the JCMF.

David O. Forfar (doforfar@outlook.com) is a trustee and former chairman of the James Clerk Maxwell Foundation.

Digital Object Identifier 10.1109/MMM.2020.3014994
Date of current version: 6 October 2020

The late Cambridge professor, Stephen Hawking, Fellow of the Royal Society, stated in a television program some years ago that there was a story that Einstein had a picture of Clerk Maxwell, in addition to that of Faraday and Newton, on the wall of his Princeton study. The photograph of Einstein in his Princeton study (Figure 1) provides the proof

for Maxwell, and we can also assume it was true for Newton and Faraday. Einstein's picture of Maxwell can be identified; it is a photograph of the portrait of Maxwell (Figure 2) by Lowes Dickinson that hangs in the hall of Trinity College, Cambridge.

In 1931, in an essay about Maxwell, Einstein wrote, "before Maxwell, physical reality was thought of as consisting of material particles. … Since Maxwell's time, physical reality has been thought of as represented by continuous fields. … This change in the conception of reality is the most profound and most fruitful that physics has experienced since the time of Newton."

Faraday and Maxwell saw electromagnetic fields, and their attendant taut "lines of force," as a means by which energy could be transmitted with a finite speed. The energy carried by certain fields, which warm any object in their path, is an example of the power of fields to transmit a physical effect (in this case, heat) across space.

Maxwell stated that it was Faraday (1791–1867) who, in 1846, first proposed that light was an electromagnetic wave. Faraday had recognized the ability of magnetism to alter light (its plane of polarization).

It was known that waves would travel through an elastic material at a speed equal to the square root of the ratio of its elastic modulus to its density. In his 1861 paper "On Physical Lines of Force," Maxwell assumed that electromagnetic waves traveled through such an "elastic material," called the *aether*. Maxwell estimated the aether's elastic modulus and density using known experimental results for the value of certain electrical and magnetic constants based on experiments that were nothing to do with light itself. The value of these electrical and magnetic constants had only been known since 1856, so Faraday himself was not able to estimate, in 1846, the speed of electromagnetic waves. However, in 1861, Maxwell was able to do so. This speed of these "electromagnetic" waves proved to be equal (within experimental error) to the known speed of light, derived by the French physicist Fizeau (1819–1896) from optical experiments on light itself. This so confirmed Faraday's prediction of 1846 that Maxwell was able to conclude in 1861, "... we can scarcely avoid the inference that light consists in the transverse undulations of the same medium, which is the cause of electric and magnetic phenomena."

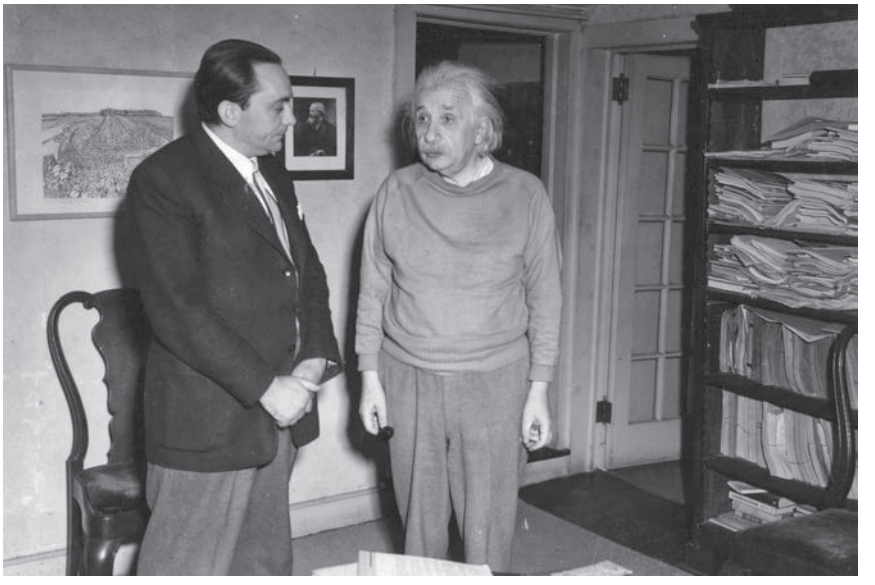

Figure 1. *Albert Einstein (right) in his Princeton study. His copy of Maxwell's portrait is visible above his right shoulder. (Source: Drew University and the Shelby White and Leon Levy Archives Center, Institute for Advanced Study, Princeton, New Jersey; used with permission.)*

In 1865, in his paper "A Dynamical Theory of the Electromagnetic Field," Maxwell gave the equations governing all electric and magnetic phenomena. Certain of the equations were mathematical expressions of previous laws of electricity and magnetism, which had already been discovered by Coulomb, Ampère, Oersted, and Faraday.

Maxwell stated that it was Faraday who, in 1846, first proposed that light was an electromagnetic wave.

In addition to these laws, Maxwell considered that a changing electric field would give rise to a special form of current. He used the analogy of positive and negative charges inside molecules (although these were then hardly known) being "displaced," i.e., being "pulled" in one direction and then "pushed" in the opposite direction (without the charges leaving the molecule), thereby creating a special type of current which needed to be included in the Oersted/Ampère law. This was new and innovative, and Maxwell used the name "displacement current," which we now know exists even in a vacuum. The equations governing the electromagnetic field are now known as *Maxwell's equations* and are among the most fundamental equations of physics, as they unify the electric and magnetic forces.

In 1864, Maxwell was then able to confirm, even more elegantly than he was able to do in his 1861 paper, that these equations lead to undulating, but mutually supportive, electric and magnetic fields. Maxwell showed again that the speed of these waves was, to within experimental error, equal to the known speed of light itself. Maxwell reiterated, "... it seems

we have strong reason to conclude that light itself (including radiant heat and other radiations, if any) is an electromagnetic disturbance in the form of waves propagated … according the electromagnetic laws." This conclusion was the most stunning conclusion of 19th century theoretical physics, as many eminent physicists of the time did not believe in such electromagnetic waves traveling with finite speed (the speed of light), thinking instead that electric and magnetic effects were transmitted instantly across the universe ("action at a distance").

Some 22 years later, in 1887, when Maxwell, had he lived, would have been only 56, Hertz demonstrated, in the laboratory, such electromagnetic waves being transmitted and received and having all the properties—reflection, refraction, interference—of waves traveling at a finite speed. This was the most stunning conclusion of 19th century experimental physics.

Maxwell's own words, "including radiant heat and other radiations, if any," have proved prescient and have been amply vindicated by the progressive discovery of a whole spectrum of electromagnetic radiation of different wavelengths—radio waves, microwaves, infrared light, visible light, ultraviolet light, X-rays, and gamma rays. A telescope in Hawaii, named appropriately after James Clerk Maxwell, operates in the microwave part of the electromagnetic spectrum. Electromagnetic waves now provide the means for modern devices to communicate without wires, for example, today's mobile phones.

Einstein

Galileo and Newton had said that, in order to change (transform) between the viewpoints of two different observers (viewing the same event but with one observer traveling with a constant speed and direction relative to the stationary observer), the speed of the moving observer would need to be added to the speed of the stationary observer. Thus, according to Galileo and Newton, "faster than light" speeds were perfectly possible. Maxwell's equations, on the other hand, gave an identical value for the speed of electromagnetic waves, no matter what the speed of the observer. These opposing theories could not both be right!

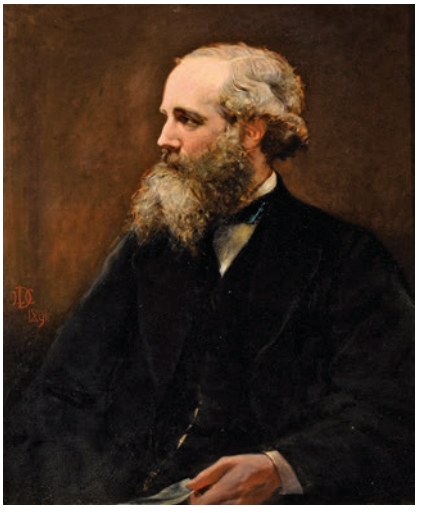

Figure 2. *Lowes Dickinson's portrait of Maxwell. (Source: The Master and Fellows, Trinity College, Cambridge; used with permission.)*

Maxwell's equations, without any alteration, were compatible with Einstein's special theory of relativity.

In his 1905 paper "On the Electrodynamics of Moving Bodies," Einstein derived the mathematical transformation (to change from one observer to another) that would result from the supposition that each observer, in his own frame of reference, measured an identical value for the speed of light. It turned out to be the same transformation which the physicist H. Lorentz (1853–1938) had formulated earlier.

In the same paper, Einstein showed his debt to Maxwell by demonstrating that Maxwell's equations, without any alteration, transformed correctly between two observers, provided the Lorentz transformation was used to change the viewpoint between the observers. It was such considerations that enabled Einstein to state confidently that nature behaved according to the Lorentz transformation and not according to the simpler Galileo/Newton transformation.

Maxwell's equations, without any alteration, were compatible with Einstein's special theory of relativity, whereas Newton's equations had to be changed. For example, the mass of a body now became dependent on its speed (as seen from Einstein's formula $m(v) = m/\sqrt{1 - v^2/c^2}$), whereas the mass of a body, under Newton, had always been a constant number, m, independent of the body's speed.

Furthermore, there could be no aether because, if there was such a thing, there would be a privileged observer in nature for whom the aether was at rest. Einstein told us that there are no privileged observers in inertial frames of reference.

Einstein further showed that, as a consequence of his 1905 paper, "if a body gives off energy L in the form of radiation, its mass diminishes by L/c^2." Einstein derived this formula by considering a body emitting an electromagnetic wave. The formula Einstein used for the energy of the resulting electromagnetic wave was the same one that Maxwell had derived. Einstein viewed the same event from the standpoint of both the stationary and the moving observer, using the Lorentz transform to change to the viewpoint from one observer to the other. By comparing the same *event*, as viewed from the two different viewpoints, he found the basis for his famous equation, $L = mc^2$ or, as we now say, $E = mc^2$.

New Products

■ **Ken Mays, Editor**

Products listed in *IEEE Microwave Magazine* are restricted to hardware, software, test equipment, services, applications, and publications for use in the science and practice of RF/microwave and wireless engineering. Product information is provided as a reader service and does not constitute endorsement by IEEE or the IEEE Microwave Theory and Techniques Society. Absolute accuracy of listings cannot be guaranteed. Contact information is provided for each product so that interested readers may make inquiries directly.

Please submit "New Products" column information to microwave.newproducts@ieee.org.

Welcome to a further installment of the "New Products" column in *IEEE Microwave Magazine*. In this issue, we present six items that may be of interest to the RF/microwave and wireless communities.

Wideband High-Power Amplifier Delivers 40 dBm From 32 to 38 GHz

ERZIA Technologies, an RF/microwave amplifier and integrated assembly company that provides commercial off-the-shelf solutions for high-performance/high-frequency applications, has announced a new compact wideband high-power amplifier (HPA) that operates from 32 to 38 GHz (Ka band). The ERZ-HPA-3200-3800-40 is designed to offer microwave system design engineers working on Ka-band applications reliable and consistent output power across the entire band of operation. In addition to 40 decibel milliwatts (dBm) of power, this microwave amplifier provides 49 dB of gain. It is qualified under U.S. Military standard MIL-STD-810F against temperature, shock, vibration, and acceleration.

The small size and modularity of the amplifier support the rapid development of microwave systems for electronic warfare (EW), avionic and ground radar, satellite communication, 5G, and test equipment operating around Ka-band frequencies. ERZIA wideband designs are among the first of their kind capable of withstanding harsh environments while maintaining output power. ERZIA developed these products in direct response to EW designers who routinely indicated their frustration with power variances throughout their critical wider-band applications and who requested a single HPA to serve a variety of multiband uses.

The ERZ-HPA-3200-3800-40 data sheet can be downloaded at www.erzia.com/microwave/hpa/562. The full lineup of ERZIA wideband HPAs includes models with the following bandwidth/output power combinations: 1–23 GHz/27 dBm, 2–18 GHz/30 dBm, 15–27 GHz/29 dBm, 17–43 GHz/22 dBm, 24–40 GHz/22 dBm, 26–40 GHz/33 dBm, 33–47 GHz/29 dBm, and 75–83 GHz/27 dBm. The models can be reviewed at https://www.erzia.com/microwave/hpa.

Digital Object Identifier 10.1109/MMM.2020.3015135
Date of current version: 6 October 2020

Sarcon Sample Kit

Fujipoly has introduced an engineering kit that includes free samples of 20 Sarcon thermal interface materials, giving engineers the flexibility to test the performance properties of multiple products. The materials in the kit offer thermal conductivities ranging from 0.9 to 13 W/mK. The kit may be requested at https://www.fujipoly.com/usa/resources/Sarcon-TIM-Sample-Kit.html.

Radiocrafts Releases Module for Massive Low-Power, Wide-Area Networks

Radiocrafts, a provider of RF modules and wireless connectivity equipment, has announced a family of RF modules for massive Internet of Things (IoT) deployments using the new Mioty radio protocol. The modules are intended for smart metering, smart city, and industrial sensor applications. The RC1882CEF-MIOTY1, measuring 12.7 × 25.4 mm, is the first shielded RF module with a complete Mioty stack designed for industrial use and volume production. The radio module is completely shielded to avoid electromagnetic interference and enable a modular certification.

The Mioty radio protocol implements the European Telecommunications Standards Institute's telegram splitting ultranarrowband (TS-UNB) Technical Specification 103 357 to achieve greater range and interference resistance. This radio technology represents a unique solution for massive IoT deployments. TS ensures a high resistance to interference, thereby reducing packet losses in noisy environments and crowded shared spectrum.

TS ensures a high resistance to interference, thereby reducing packet losses in noisy environments and crowded shared spectrum.

The module is supported by a development kit consisting of two development boards and accessories that, out of the box, can be connected to a PC and be ready to send application data to a Mioty gateway, including all third-party models. The initial release is a one-way solution for data transmission, and it will be upgraded to bidirectionality as soon as the infrastructure is in place. Also, a U.S. Federal Communications Commission-compliant variant is planned. The European version, at 868 MHz, is available as an evaluation sample and development kit.

Key features of the new Mioty module and technology include the following:

- low-power, wide-area network (LPWAN): UNB radio with TS technology
- high resistance to interference
- the only LPWAN for massive IoT deployments
- more than 1 million messages per day in one network (single gateway)
- typical 15-km line of sight (5 km in urban environments)
- license-free 868 MHz for Europe; 915 MHz for the United States (to be released)
- very low power consumption, short radio transmissions, and battery friendly
- shielded compact module (12.7 × 25.4 mm) delivered on tape and reel.

For further information, contact Radiocrafts by telephone at +47 4000 5195 and email at sales@radiocrafts.com.

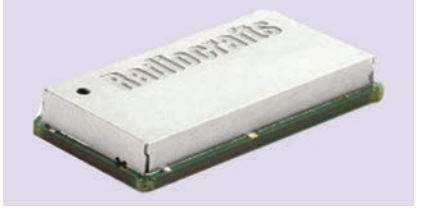

Copper Mountain Releases Compact Vector Network Analyzers With Improved Performance

Copper Mountain Technologies has released compact vector network analyzers (VNAs) S5045 and M5045 with a frequency range from 9 kHz to 4.5 GHz. Featuring a typical dynamic range of 130 dB and a measurement speed of 70 μs, these VNAs replace the recently discontinued S5048 while delivering improved performance. The S5045 comes with advanced software features. The M5045 joins the M series of VNAs and includes standard software features in an economical package. For additional information, visit https://coppermountaintech.com/vna/.

Modelithics Acquires ProbePoints and Launches Fixture and Accessory Products

Modelithics' acquisition of Jmicro Technology's ProbePoints substrate fixture assets encompasses test fixtures and probing accessories for RF/microwave and electrical testing of advanced semiconductor devices and

packaging products. These include alumina substrate fixtures that enable devices without ground–signal–ground probe pads to be evaluated with RF wafer probes. Modelithics will offer standard and custom microwave and millimeter-wave test fixtures and calibration standards in addition to the ProbePoint products.

Designers can now obtain test fixtures and accessories from a company known for precision measurements and trusted models. Modelithics has established an excellent reputation in the RF/microwave industry through its characterization and measurement services as well as measurement-based active and passive simulation models, such as Modelithics COMPLETE Library, which is available for multiple electronic design automation simulation tools. For more information and to request a quote, visit the Modelithics website at www.modelithics.com/home/fixtures or contact the company via email at sales@modelithics.com.

Primarily for use in the high-speed digital test market, this connector is designed for stripline applications.

Samtec Releases 2.4-mm Compression Mount Connector

Samtec has released a 2.40-mm compression-mount connector designed

to perform at up to 50 GHz. Primarily for use in the high-speed digital test market, this connector is designed for stripline applications. The connector is vertically mounted to the printed circuit board and attached by two 0–80 Unified Thread Standard screws, eliminating the need for soldering to the test points. A microstrip design is in development. For more information, visit http://www.samtec.com.

Enigmas, etc.

Impedance Plane

■ **Takashi Ohira**

Two points, $Z_1 = 50 - j25$ and $Z_2 = 50 + j75$, are plotted on the complex impedance plane, as shown in Figure 1. To link these two points, we consider four different routes. Judging from the Poincaré metric, which one is the shortest? Find the correct answer from among the following four choices:

a) straight line
b) obtuse bent
c) right bent
d) acute bent.

In the sense of hyperbolic geometry, the four routes are all curving, although they look like straight or bent lines. Therefore, path length Λ cannot be estimated by merely measuring the distance between two points but should be strictly measured by the line integral

$$\Lambda = \int_c d\Lambda \tag{1}$$

along the route. To perform this integration, infinitesimal segment length $d\Lambda$ is defined as

$$d\Lambda = \frac{1}{R}\sqrt{dR^2 + dX^2}, \tag{2}$$

which is identical to that defined for the curves projected on the Smith chart [1].

The complex plane with Cartesian coordinates was named *Gaussian plane* after the German mathematician and physicist Carl Friedrich Gauss (see Figure 2).

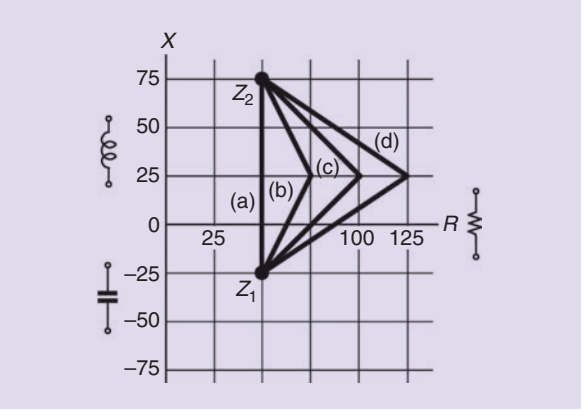

Figure 1. *The four different routes for linking Z_1 and Z_2 on the impedance half-plane. The straight-looking option is not always the best.*

Figure 2. *A portrait of German mathematician and physicist Carl Friedrich Gauss (1777–1855). (Image courtesy of Marimo Matsumoto, Toyohashi University of Technology; used with permission.)*

Takashi Ohira (ohira@tut.jp) is with Toyohashi University of Technology, Aichi, Japan. He is a Senior Life Fellow of IEEE.

Digital Object Identifier 10.1109/MMM.2020.3015137
Date of current version: 6 October 2020

More specifically, the plane shown in Figure 1 should be called *impedance half-plane* because we assume only passive load impedance, i.e., $R > 0$, whereas X runs from positive (inductive) to negative (capacitive) reactance. The mathematical concept of half-plane was first exploited by Henri Poincaré to create a simple model of hyperbolic geometry.

The purpose of this challenge is to get vistas on that plane's behavior from the viewpoint of RF engineers. The correct answer will appear in next month's "Enigmas, etc."

Solution to the October 2020 Puzzle

We start from the voltage standing-wave ratio-based reflectance formula

$$\Gamma = \frac{\rho - 1}{\rho + 1} e^{j\theta}. \tag{1}$$

Putting it into the Beltrami–Klein disk definition, we get

$$\begin{aligned}\Omega &= \frac{\rho^2 - 1}{\rho^2 + 1} e^{j\theta} = \frac{(\rho + 1)^2}{\rho^2 + 1}\Gamma \\ &= \frac{2(\rho + 1)^2\Gamma}{(\rho + 1)^2 + (\rho - 1)^2} = \frac{2\Gamma}{1 + \Gamma\Gamma^*},\end{aligned} \tag{2}$$

where superscript * designates the complex conjugate. As commonly known in 50-Ω systems, the reflectance is translated into the impedance domain as

$$\Gamma = \frac{Z - 50}{Z + 50} = \frac{R - 50 + jX}{R + 50 + jX}. \tag{3}$$

Putting it again into (2), we obtain $\Omega = u + jv$ with

$$u = \frac{R^2 + X^2 - 50^2}{R^2 + X^2 + 50^2}, \tag{4}$$

$$v = \frac{100X}{R^2 + X^2 + 50^2}. \tag{5}$$

To observe the constant-X contour in question, we eliminate R from (4) and (5). Although this algebra may look complicated, it results, after all, in a simple linear equation:

$$50v = X(1 - u). \tag{6}$$

Because it draws a straight line on the $u - v$ plane or disk Ω, the correct answer to last month's puzzle is a). To get the line's geometrical view, see Figure 3, which shows 11 constant-X contours on the disk, together with seven constant-R ellipses.

Thanks to the duality theorem, we can also deduce a sister equation,

$$v = -50B(1 + u), \tag{7}$$

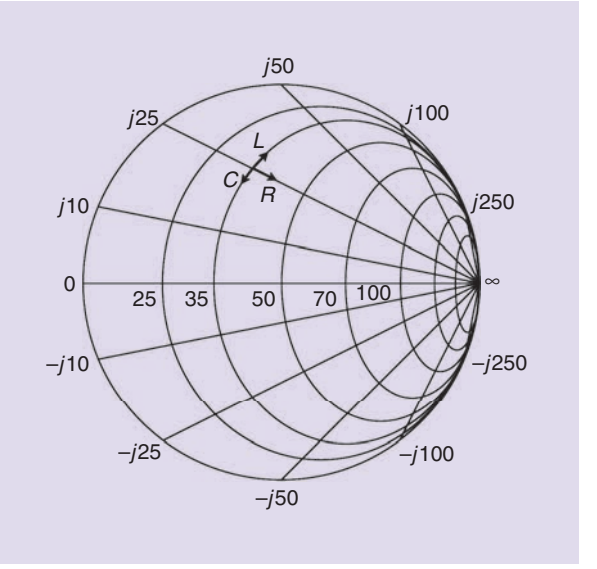

Figure 3. *A Beltrami–Klein disk with constant-X lines and constant-R ellipses.*

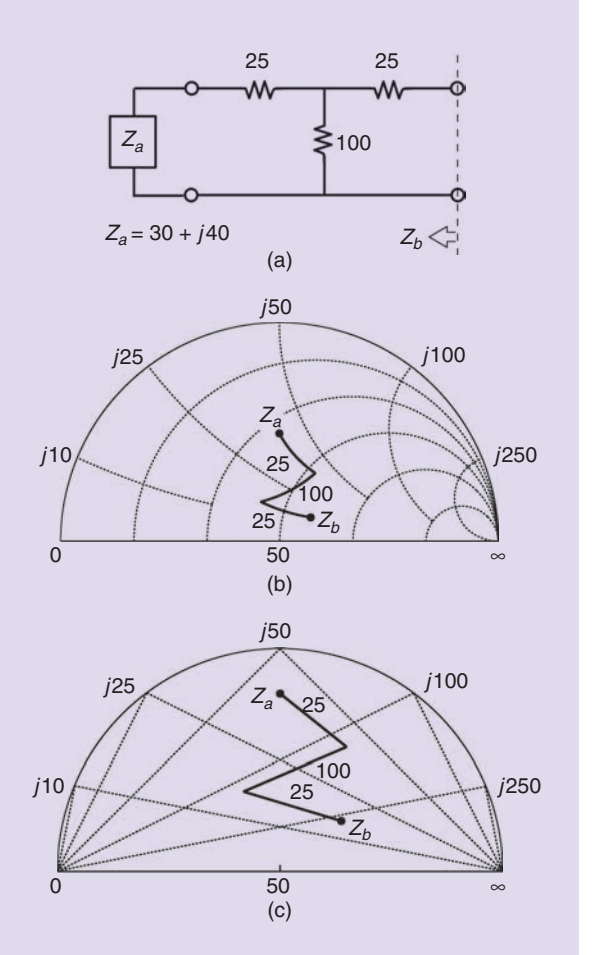

Figure 4. *A resistive network-impedance trajectory projected on the Smith chart and Beltrami–Klein disk.*

to draw a constant-B contour of admittance $Y = G + jB$. Note that $B < 0$ on the upper half of disk Ω. Constant-B contours can be also obtained geometrically by flipping over the constant-X contours from left to right, as seen in the following example.

To experience (6) and (7) in practice, one typical example is presented in Figure 4. A three-element resistive network is connected to impedance $Z_a = 30 + j40$. The trajectory starts from Z_a and zigzags down in three steps toward the horizon. It is so wonderful that every step exhibits a linear segment for both series and shunt resistors! As we know, however, they would look concave if the disk were a regular Smith chart. This astonishing linearity is a distinct feature of the Beltrami–Klein disk from the viewpoint of RF engineering [2]–[4].

References

[1] T. Ohira, "Poincaré length," *IEEE Microw. Mag.*, vol. 21, no. 3, pp. 120–121, Mar. 2020. doi: 10.1109/MMM.2019.2958799.

[2] T. Ohira, "Beltrami-Klein disk model as viewed for use in impedance trajectory projection," *IEICE Communications Express*, vol. 9, no. 7, pp. 256–261, July 2020.

[3] T. Ohira, "A radio engineer's voyage to double-century-old plane geometry," *IEEE Microw. Mag.*, vol. 21, no. 11, pp. 60–67, Nov. 2020.

[4] T. Ohira and S. Abe, "Power standing wave ratio as a local grid magnifier for close observation of impedance trajectories (invited)," in *Proc. IEEE Int. Symp. Radio-Frequency Integration Technology*, WE4B-1, Hiroshima, Nov. 2020.

Conference Calendar

Editor's Note: Please check the website of each conference for any changes to paper or workshop deadlines or conference dates and modality (in person, virtual, or hybrid).

OCTOBER 2020

2020 IEEE Global Humanitarian Technology Conference (GHTC)
29 October–1 November 2020
Location: Seattle, Washington, United States (Virtual Conference)

NOVEMBER 2020

2020 IEEE BiCMOS and Compound Semiconductor Integrated Circuits and Technology Symposium (BCICTS)
8–11 November 2020
Location: Monterey, California, United States (Virtual Conference)

2020 45th International Conference on Infrared, Millimeter, and Terahertz Waves (IRMMW-THz)
8–13 November 2020
Location: Buffalo, New York, United States (Virtual Conference)

2020 IEEE Asia-Pacific Microwave Conference (APMC 2020)
10–13 November 2020
Location: Hong Kong (Virtual Conference)

Digital Object Identifier 10.1109/MMM.2020.3017975
Date of current version: 6 October 2020

2020 IEEE PELS Workshop on Emerging Technologies: Wireless Power Transfer (WoW) and 2020 IEEE Wireless Power Transfer Conference (WPTC)
15–19 November 2020
Location: Seoul, South Korea (WPTC: Hybrid Conference; WoW: Virtual Conference)

2020 International Topical Meeting on Microwave Photonics (MWP)
23–26 November 2020
Location: Matsue, Japan (Virtual Conference)

DECEMBER 2020

2020 IEEE 21st Annual Wireless and Microwave Technology Conference (WAMICON)
1–3 December 2020
Location: Sand Key, Florida, United States

2020 IEEE MTT-S International Conference on Numerical Electromagnetic and Multiphysics Modeling and Optimization (NEMO)
7–9 December 2020
Location: Hangzhou, China

2020 IEEE MTT-S International Microwave and RF Conference (IMARC)
10–12 December 2020
(postponed to 2021)
Location: Kanpur, India

2020 IEEE MTT-S Latin America Microwave Conference (LAMC)
14–16 December 2020
(postponed to May 2021)
Location: Cali, Colombia

2020 IEEE MTT-S International Microwave Biomedical Conference (IMBioC)
14–17 December 2020
Location: Toulouse, France

JANUARY 2021

2020 50th European Microwave Conference (EuMC), 2020 15th European Microwave Integrated Circuits Conference (EuMIC), and 2020 17th European Radar Conference (EuRAD)
10–15 January 2021
Location: Utrecht, The Netherlands

2021 IEEE Radio and Wireless Week (RWW2021, colocated with ARFTG)
17–20 January 2021
Location: San Diego, California, United States (Virtual Conference)

JUNE 2021

2021 IEEE/MTT-S International Microwave Symposium (IMS2021 colocated with ARFTG and RFIC)
6–11 June 2021
Location: Atlanta, Georgia, United States

IMS

Connecting Minds. Exchanging Ideas.

IEEE MTT-S INTERNATIONAL MICROWAVE SYMPOSIUM

IMS2021

EXHIBITION & SPONSORSHIP PREVIEW

6-11 June 2021

ATLANTA•GEORGIA

www.ims-ieee.org/ims2021

IEEE

MTT-S™ IEEE MICROWAVE THEORY & TECHNIQUES SOCIETY

Digital Object Identifier 10.1109/MMM.2020.3020489

Join us in Atlanta, as we come together once again for the world's premier RF and microwave industry conference and tradeshow: IMS2021. Now in its 64th year, IMS is the place to be each year for professionals buying and developing materials, devices, components, systems, design & simulation software, and test & measurement equipment for products operating from RF to THz.

9000 participants from over 50 countries include senior management, engineering management, engineers, and R&D personnel from academia, commercial industry, and government/military. Participating exhibitors can establish new US and international connections, present products directly to industry leaders, and see the state of the art in a showcase of the best developments for applications that enable us to connect for a smarter, safer world.

Georgia World Congress Center

In the heart of Atlanta, the Georgia World Congress Center is at the forefront of the meeting industry, on the vanguard of event health and safety, and offers these features and benefits:

- Largest combined convention, sports, and entertainment campus in North America
- 220 acres anchored by Georgia World Congress Center, Centennial Olympic Park, and Mercedes-Benz Stadium
- 12,000 hotel rooms within walking distance
- 1.5 million square feet of prime exhibit space
- World's largest LEED certified convention center
- Ample meeting space for exhibitor meetings
- Branding opportunities within the facility
- Wi-Fi throughout the facility
- Inexpensive Public Transportation via Metropolitan Atlanta Rapid Transit Authority (MARTA) from Atlanta area and Hartsfield-Jackson Atlanta International Airport to GWCC/CNN Station (W-1)

Reserve your IMS exhibition booth today!

Attendee Snapshot

IMS Four Year Attendance Numbers

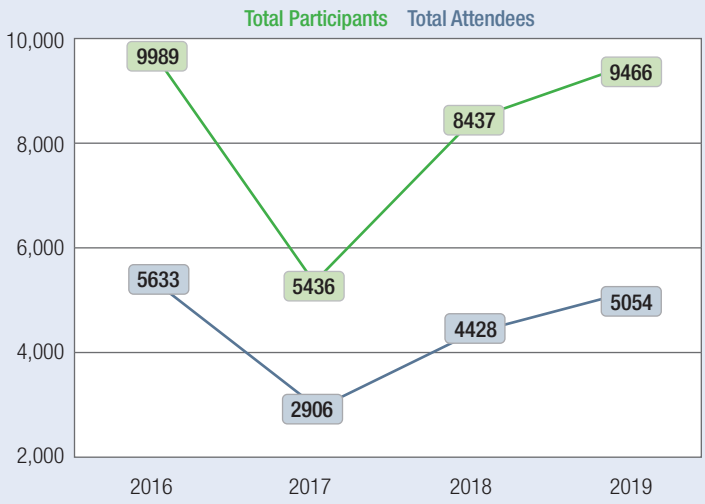

Why Become a Sponsor at IMS 2021?

Beyond the Booth:
Market to attendees throughout the convention center, inviting them to your booth on the show floor. Whether you are looking to promote a product, build your brand, or connect with customers, a sponsorship helps raise your profile. Our expert sales team can help you construct the sponsorship plan that best meets your marketing goals.

Contact your sales representative or exhibits@horizonhouse.com to discuss exhibit and sponsorship opportunities at IMS2021.

Expo Floor – Exhibit Options

IMS
Connecting Minds. Exchanging Ideas.

Exhibitor Benefits

Exhibitors will enjoy the following benefits before, during and after the conference:

Pre-Show:

- An IMS exhibitor console. Dedicated area to showcase your profile.
- Access to 2021 promotional opportunities
- Choice of hotel accommodations including hospitality suites and meeting space

On-Site:

- A listing in the official Conference Program/Exhibition Catalog
- Priority space selection for the IMS2022
- Access to discounted conference registrations
- General exhibit hall security service
- Daily aisle cleaning service

Post-Show:

- Post-event report with conference audit and attendee demographics

STANDARD EXHIBIT BOOTH

IMS2021 Exhibit Space is $3,800 per 10x10 booth.

- Illuminated exhibit space with 8' high backwall drape if needed and 3' high side rails (in-line booths only).
- A 7" x 44" identification sign with the exhibitor's name and booth number (in-line booths only).
- Furnished booth packages and booth decor available in the Exhibitor Manual through the event decorator.

5G Pavilion

The 5G pavilion offers a special turnkey position on the show floor to introduce and showcase your 5G products. All participants receive the following for $3,400:

- 6ft draped table, 2 chairs and electrical
- Identified as a 5G Pavilion participant on all 5G signage
- Promotional listing on the 5G web page, pages in the printed Conference Program/Exhibition Catalog
- Highlighted in IMS attendee promotions and featured on IMS website
- Option to lead a talk in the theater on 5G

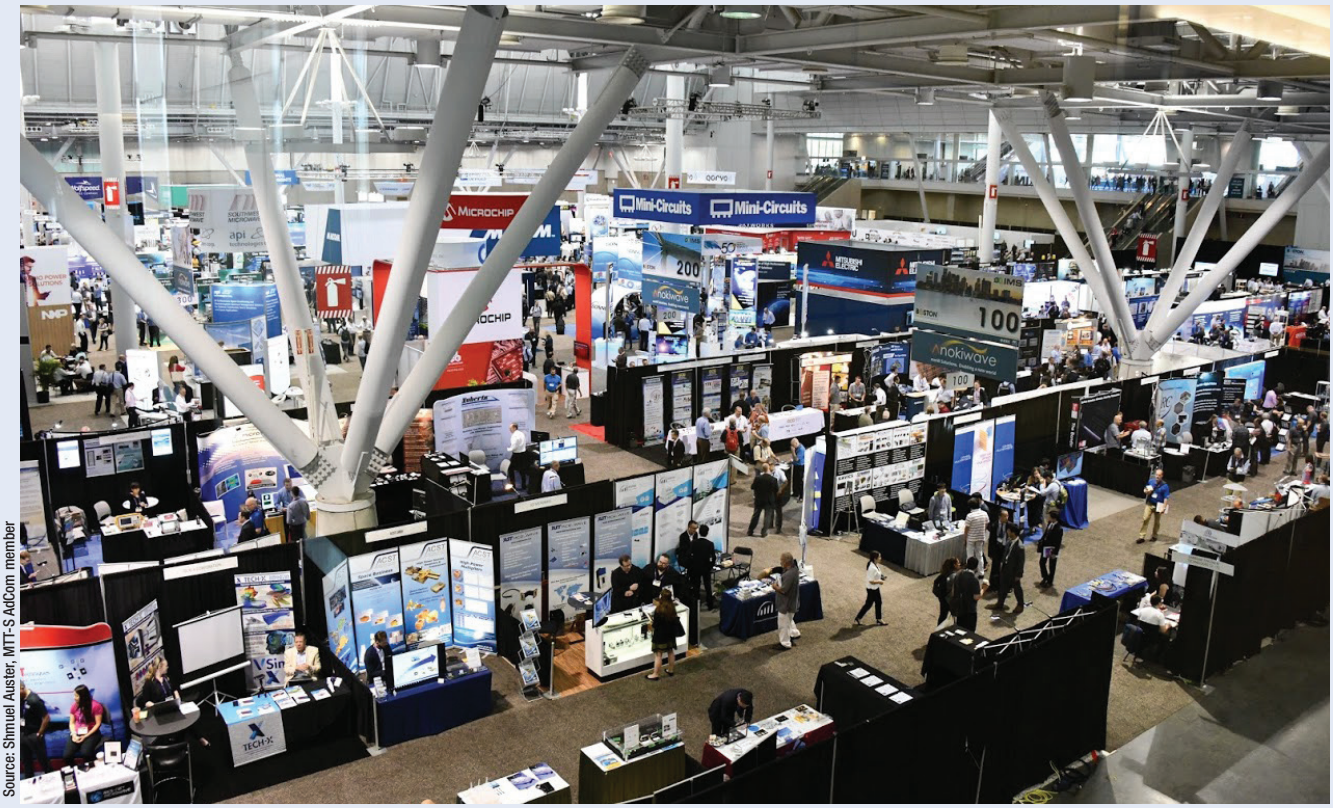

Source: Shmuel Auster, MTT-S AdCom member

IMS

Connecting Minds. Exchanging Ideas.

For details, visit: https://ims-ieee.org/ims2021

SALES REPRESENTATIVES

For General Inquiries
Call (781) 619-1994
or email
exhibits@horizonhouse.com

Eastern and Central Time Zones
Michael Hallman
Sales Manager
4 Valley View Court
Middletown, MD 21769
Tel: (301) 371-8830
FAX: (301) 371-8832
mhallman@horizonhouse.com

Pacific and Mountain Time Zones
Brian Landy
Western Reg. Sales Mgr.
(CA, AZ, OR, WA, ID, NV, UT, NM, CO, WY, MT, ND, SD, NE & Western Canada)
144 Segre Place
Santa Cruz, CA 95060
Tel: (831) 426-4143
FAX: (831) 515-5444
blandy@horizonhouse.com

International Sales
Richard Vaughan
International Sales Manager
16 Sussex Street
London SW1V 4RW, England
Tel: +44 207 596 8742
FAX: +44 207 596 8749
rvaughan@horizonhouse.co.uk

Germany, Austria, and Switzerland
(German-speaking)
WMS.Werbe- und Media Service
Brigitte Beranek
Gerhart-Hauptmann-Street 33,
D-72574 Bad Urach
Germany
Tel: +49 7125 407 31 18
FAX: +49 7125 407 31 08
bberanek@horizonhouse.com

France
Gaston Traboulsi
Tel: 44 207 596 8742
gtraboulsi@horizonhouse.com

Israel
Dan Aronovic
Tel: 972 50 799 1121
aronovic@actcom.co.il

Korea
Young-Seoh Chinn
JES MEDIA, INC.
F801, MisahausD EL Tower
35 Jojeongdae-Ro
Hanam City, Gyeonggi-Do 12918 Korea
Tel: +82 2 481-3411
FAX: +82 2 481-3414
yschinn@horizonhouse.com

China
Shenzhen
Michael Tsui
ACT International
Tel: 86-755-25988571
FAX: 86-755-25988567
michaelt@actintl.com.hk

Shanghai
Linda Li
ACT International
Tel: 86-021-62511200
lindal@actintl.com.hk

Beijing
Cecily Bian
ACT International
Tel: +86 135 5262 1310
cecilyb@actintl.com.hk

Hong Kong, Taiwan, Singapore
Mark Mak
ACT International
Tel: 852-28386298
markm@actintl.com.hk

Japan
Katsuhiro Ishii
Ace Media Service Inc.
12-6, 4-Chome,
Nishiiko, Adachi-Ku
Tokyo 121-0824, Japan
Tel: +81 3 5691 3335
FAX: +81 3 5691 3336
amskatsu@dream.com

CONNECTING FOR A SMARTER, SAFER WORLD

Smartphones, smart homes, smart...healthcare?

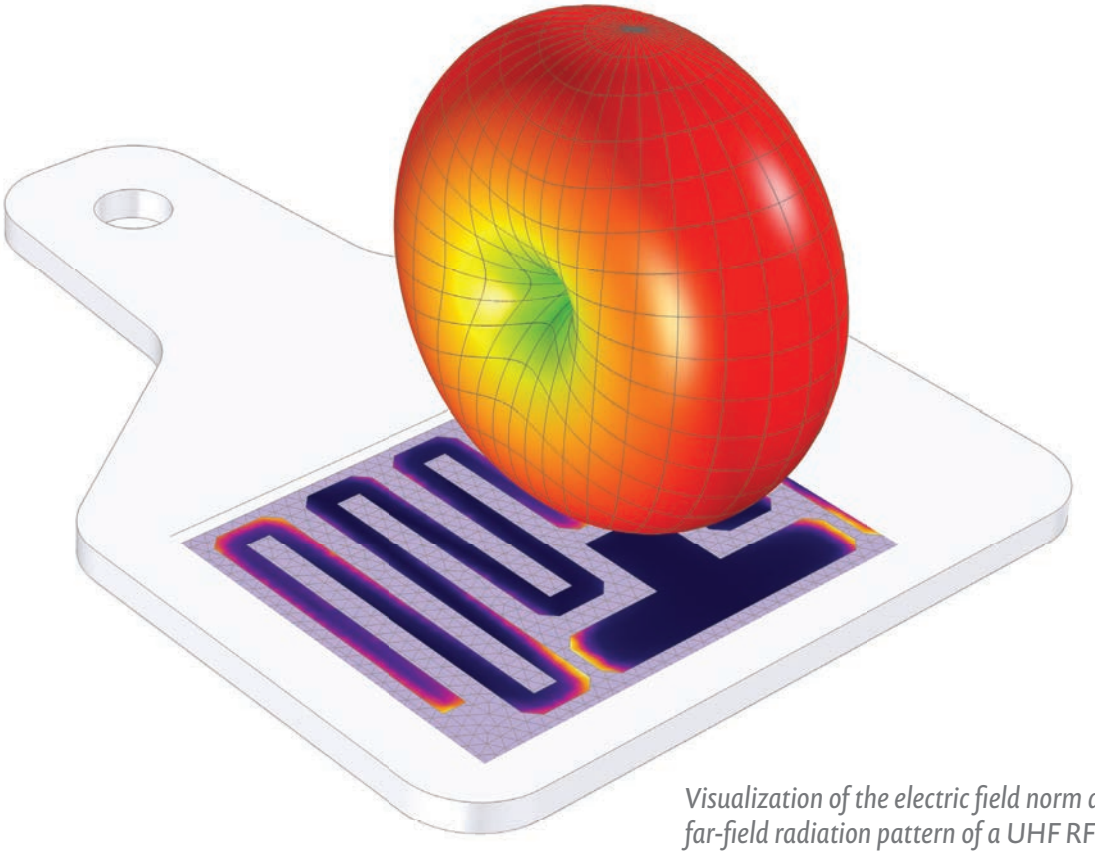

Visualization of the electric field norm and far-field radiation pattern of a UHF RFID tag.

RFID tags are used across many industries, but when it comes to healthcare, there is a major design challenge: size. If wearable RFID tags are too big and bulky, they could cause patient discomfort. Or, if the tag is for a biomedical implant, it has to be smaller than a grain of rice! Design engineers can optimize the size of an RFID tag for its intended purpose using RF simulation.

The COMSOL Multiphysics® software is used for simulating designs, devices, and processes in all fields of engineering, manufacturing, and scientific research. See how you can apply it to designing RFID tags.

comsol.blog/biomed-RFID-tags

COMSOL